

THESIS

IONOSPHERIC SCINTILLATION EFFECTS ON GPS MEASUREMENTS AND
ALGORITHMS TO IMPROVE POSITIONING SOLUTION ACCURACY

Submitted by

Gregory Thomas Myer

Department of Electrical and Computer Engineering

In partial fulfillment of the requirements

For the Degree of Master of Science

Colorado State University

Fort Collins, Colorado

Summer 2017

Master's Committee:

Advisor: Y.T. Jade Morton

Jesse Wilson

Clayton Shonkwiler

Copyright by Gregory T. Myer 2017

All Rights Reserved

ABSTRACT

IONOSPHERIC SCINTILLATION EFFECTS ON GPS MEASUREMENTS AND ALGORITHMS TO IMPROVE POSITIONING SOLUTION ACCURACY

The ionosphere is an important cause of disturbances on GNSS signals, especially in high latitudes and equatorial areas. Previous studies indicate that while ionospheric scintillation may cause abrupt, random fluctuations in carrier phase measurements, its impact on pseudorange is less serious. Since modern GNSS receivers, especially those for high precision applications, use carrier phase-smoothed pseudoranges to improve accuracy of position solutions, there exists the need to have a better understanding of the scintillation effects on carrier phase measurements and developing means to mitigate scintillation induced errors in navigation solutions.

In this thesis, scintillation impacts are demonstrated on carrier phase and pseudorange measurements using real scintillation data collected at high latitudes and equatorial areas, and the effect on positioning is investigated and mitigated. To obtain a more insightful and quantitative understanding of the impact, the data was used to generate position solutions using standard navigation processing algorithms. The results clearly indicate that sudden carrier phase discontinuities during strong scintillation lead to the degradation of carrier-smoothed pseudorange accuracy and consequently, results in large position errors. During strong scintillation with no carrier phase discontinuities, comparatively smaller position errors are found due to phase fluctuations that cause small changes in the range measurements.

Based on this analysis, we give examples of several approaches to mitigate these problems, and use these approaches to present adaptive positioning techniques to mitigate scintillation induced position errors. One algorithm simply replaces the carrier-smoothed pseudorange

with the unsmoothed pseudorange for satellites that are affected by outages on the carrier phase measurements, or if strong scintillation is detected. Another adaptive algorithm uses the GDOP to determine if a scintillating satellite can be completely removed from the navigation processing to improve positioning accuracy.

Results show that the algorithms that substitute the unsmoothed pseudorange increase errors by 24.5% as compared to a conventional technique that repairs cycle slips, which indicates that it is still best to use the carrier-smoothed pseudoranges as long as there are no discontinuities. Results from the adaptive technique based on the analysis of the GDOP show a reduction of maximum errors on average by 13% on all of the data sets when comparing to a conventional algorithm. It was also found that a new carrier-smoothing technique can reduce maximum errors by 7.9% on average. Alternative approaches for future improvements are also discussed.

ACKNOWLEDGEMENTS

There are several people that I would like to thank that made this project possible. My advisor, Dr. Jade Morton has helped endlessly with guidance, suggestions, and new ideas. I have learned so much from Dr. Morton starting from the very fundamentals of this field. I would also like to thank my other committee members, Dr. Jesse Wilson and Dr. Clayton Shonkwiler for asking relevant questions that could improve this work.

Several other graduate students in the GPS Lab specifically deserve gratitude. Brian Breitsch taught me technical details of how the lab operates, and helped me get up to speed when I first started research. I want to thank Ian Collett for proofreading this document, and providing valuable suggestions. Also, I'd like to thank Steve Taylor and Harrison Bourne for the development, installation, and maintenance of the data collection systems, as well as the software tools that drive our research. Without them, this research would not be possible.

Last, I want to thank my family for all of their support and encouragement with my education.

This research is sponsored by Honeywell and by a contract (FA8650-14-1735) with the Air Force Research Laboratory (AFRL) through BerriHill.

TABLE OF CONTENTS

ABSTRACT	ii
ACKNOWLEDGEMENTS	iv
CHAPTER 1 INTRODUCTION AND BACKGROUND	1
1.1 Motivation	1
1.2 GPS Signals and Signal Structure	4
1.3 GPS Positioning	9
1.3.1 Trilateration	9
1.3.2 Ionospheric Delay	11
1.3.3 Tropospheric Delay	11
1.3.4 Hardware Biases	13
1.3.5 Multipath Error	14
1.3.6 Position Estimation Using Pseudoranges	14
1.4 Receiver Reference Generation Using Precise Point Positioning (PPP)	16
1.5 Introduction to Ionospheric Scintillation	17
1.6 Prior Research	19
1.7 Contributions of Thesis Research	21
1.8 Thesis Organization	21

CHAPTER 2	IONOSPHERIC SCINTILLATION	22
2.1	Data Collection	22
2.2	Equatorial Scintillation Morphology	23
2.3	Scintillation Effects on GPS Signals and GPS Positioning	29
2.3.1	Cycle Slips	30
2.3.2	Dropped Measurements	34
2.3.3	Phase Error	38
2.3.4	Septentrio Position Errors	40
CHAPTER 3	METHODOLOGY	43
3.1	Cycle Slip Detection	44
3.2	Cycle Slip Repair	45
3.3	Carrier-Smoothing Algorithms	48
3.3.1	Hatch Filter for Carrier-Smoothing	49
3.3.2	Code-Noise Multipath Bias Estimation for Carrier-Smoothing	51
3.3.3	Hybrid Hatch Filter/CNMP for Carrier-Smoothing	54
3.4	Pseudorange Substitution During Carrier-Phase Discontinuity	58
3.5	Removing Measurements Impacted by Scintillation	61
3.6	Weighting Measurements Impacted by Scintillation	63
3.7	Adaptive Positioning Algorithms	65

3.7.1	Adaptive Positioning based on Phase Scintillation Detection ($A\text{-}\sigma_\phi$)	66
3.7.2	Adaptive Positioning based on GDOP Analysis ($A\text{-GDOP}$)	67
3.7.3	Summary of Positioning Algorithms	70
CHAPTER 4	RESULTS	72
4.1	Comparison of Positioning Algorithms During Scintillation	72
4.1.1	Positioning Results: 1 Satellite Scintillating	73
4.1.2	Positioning Results: 2 Satellites Scintillating	81
4.1.3	Positioning Results: 3 or More Satellites Scintillating	86
CHAPTER 5	CONCLUSIONS AND FUTURE WORK	92
REFERENCES	96
APPENDIX A	ADDITIONAL PLOTS	101

LIST OF TABLES

1.1	ILS Approach Categories	4
3.1	Error reduction during cycle slips	60
3.2	Summary of positioning algorithms	71
4.1	Adaptive positioning algorithm performance - 1 satellite scintillating	80
4.2	Adaptive positioning algorithm performance - 2 satellites scintillating	85
4.3	Adaptive positioning algorithm performance - scenario 3	91

LIST OF FIGURES

1.1	Aircraft approach using GPS and GBAS	2
1.2	Decision height and runway visual range	3
1.3	GPS L1 C/A signal block diagram	5
1.4	GPS L2C signal block diagram	6
1.5	Pseudorange and ADR measurements	8
1.6	2D trilateration	10
1.7	3D trilateration	10
2.1	GPS Lab data collection systems	23
2.2	Jicamarca, Peru yearly and hourly S_4 dependance	25
2.3	Jicamarca, Peru yearly and hourly σ_ϕ (radians) dependance	26
2.4	Jicamarca, Peru σ_ϕ versus S_4	27
2.5	Jicamarca, Peru seasonal scintillation events	28
2.6	Overview of ADR measurement problems	29
2.7	Peru ADR difference	30
2.8	Number of cycle slips vs. S_4 and σ_ϕ in equatorial regions	31
2.9	Number of cycle slips vs. S_4 and σ_ϕ in high latitude	32
2.10	Normalized cycle slips per 3 minutes	33
2.11	Position errors due to cycle slips	33

2.12	Position errors due to small cycle slips	34
2.13	Ascension Island dropped measurements	35
2.14	Statistics of dropped measurements	36
2.15	Position errors due to dropped measurements	37
2.16	Phase fluctuations	38
2.17	Range changes due to σ_ϕ	39
2.18	Position errors due to phase error	40
2.19	Septentrio receiver position error	41
3.1	Overview of methods to mitigate ADR measurement problems	43
3.2	Cycle slip detection	45
3.3	Satellite measurements for cycle slip repair	46
3.4	Cycle slip repair 1	47
3.5	Cycle slip repair 2	48
3.6	Hatch filter carrier-smoothing	50
3.7	CNMP error bounds	53
3.8	CNMP bias estimation	53
3.9	Hatch filter/CNMP hybrid flowchart	55
3.10	Hatch filter/CNMP hybrid carrier-smoothing	56
3.11	Poor bias estimate from hybrid Hatch filter/CNMP carrier-smoothing	57

3.12	Poker Flat, Alaska ρ_c vs. ρ_B positioning	58
3.13	Jicamarca, Peru 11/3/2014 ρ_c vs. ρ_B positioning	59
3.14	Jicamarca, Peru 11/25/2014 ρ_c vs. ρ_B positioning	60
3.15	Jicamarca, Peru skyplot	61
3.16	Jicamarca, Peru position errors after removing satellites	62
3.17	Jicamarca, Peru position errors after weighting PRN 16	64
3.18	Jicamarca, Peru position errors after weighting PRN 27	64
3.19	Visual of $A\text{-}\sigma_\phi$ algorithm	66
3.20	Block diagram of $A\text{-}\sigma_\phi$ algorithm	67
3.21	Visual of $A\text{-}GDOP$ algorithm	69
3.22	Block diagram of $A\text{-}GDOP$ algorithm	69
4.1	Ascension Island skyplot	73
4.2	Ascension Island positioning error statistics	74
4.3	Ascension Island positioning algorithms	75
4.4	Positioning error statistics: one satellite scintillating	77
4.5	Skyplots: days with one satellite scintillating	78
4.6	Ascension Island skyplot	81
4.7	Ascension Island positioning error statistics	82
4.8	Ascension Island positioning algorithms	82

4.9	Positioning error statistics: two satellites scintillating	84
4.10	Poker Flat, Alaska skyplot	86
4.11	Poker Flat, Alaska positioning error statistics	87
4.12	Poker Flat, Alaska positioning algorithms	88
4.13	Scenario 3 positioning error statistics	90
A.1	Poker Flat, Alaska 7/3/2014 skyplot	101
A.2	Poker Flat, Alaska 7/3/2014 positioning algorithms	102
A.3	Poker Flat, Alaska 10/7/2015 skyplot	102
A.4	Poker Flat, Alaska 10/7/2015 positioning algorithms	103
A.5	Poker Flat, Alaska 10/7/2015 skyplot	103
A.6	Poker Flat, Alaska 10/7/2015 positioning algorithms	104
A.7	Poker Flat, Alaska 3/30/2016 skyplot	104
A.8	Poker Flat, Alaska 3/30/2016 positioning algorithms	105
A.9	Poker Flat, Alaska 3/30/2016 skyplot	105
A.10	Poker Flat, Alaska 3/30/2016 positioning algorithms	106
A.11	Poker Flat, Alaska 4/1/2016 skyplot	106
A.12	Poker Flat, Alaska 4/1/2016 positioning algorithms	107
A.13	Ascension Island 3/2/2013 skyplot	107
A.14	Ascension Island 3/2/2013 positioning algorithms	108

A.15 Ascension Island 3/4/2013 skyplot	108
A.16 Ascension Island 3/4/2013 positioning algorithms	109
A.17 Ascension Island 3/5/2013 skyplot	109
A.18 Ascension Island 3/5/2013 positioning algorithms	110
A.19 Ascension Island 3/8/2013 skyplot	110
A.20 Ascension Island 3/8/2013 positioning algorithms	111
A.21 Ascension Island 3/9/2013 skyplot	111
A.22 Ascension Island 3/9/2013 positioning algorithms	112
A.23 Ascension Island 3/10/2013 skyplot	112
A.24 Ascension Island 3/10/2013 positioning algorithms	113
A.25 Ascension Island 3/10/2013 skyplot	113
A.26 Ascension Island 3/10/2013 positioning algorithms	114
A.27 Jicamarca, Peru 10/5/2013 skyplot	114
A.28 Jicamarca, Peru 10/5/2013 positioning algorithms	115
A.29 Jicamarca, Peru 10/5/2013 skyplot	115
A.30 Jicamarca, Peru 10/5/2013 positioning algorithms	116
A.31 Jicamarca, Peru 11/3/2014 skyplot	116
A.32 Jicamarca, Peru 11/3/2014 positioning algorithms	117
A.33 Jicamarca, Peru 11/3/2014 skyplot	117

A.34 Jicamarca, Peru 11/3/2014 positioning algorithms	118
A.35 Jicamarca, Peru 11/25/2014 skyplot	118

CHAPTER 1

INTRODUCTION AND BACKGROUND

The Global Navigation Satellite System (GNSS) is comprised of several satellite constellations developed by various countries to provide precise position, navigation, and timing (PNT). The United States' Global Positioning System (GPS), the Russian Global Navigation Satellite System (GLONASS), the European Union's satellite system (Galileo), and the Chinese BeiDou Navigation Satellite System (BDS) are all currently operational, with continuous effort for improvement. Together, these satellite systems provide world-wide coverage for countless modern applications. While it is typical to think of GNSS as a system to help users navigate on the ground with small receivers, many other industries rely on and benefit from GNSS PNT. To name a few examples, accurate positioning is useful for new transport systems, efficiency in modern agriculture, and surveying and mapping in Geographic Information Systems (GIS). Precise timing provided by atomic clocks on board the satellites is used for synchronization of power systems, weather radars, and financial transactions [1].

1.1 Motivation

Apart from previous examples, this thesis is directed towards the aviation industry, which is in heavy development of technology to exploit GNSS for the most accuracy possible. Many locations around the world utilize GNSS to increase efficiency in routing, air traffic management, and precision landings during low visibility [1]. Due to the criticality of plane landings, we must ensure reliability from GNSS receivers and ground systems. To keep the system robust, any errors along the path from each satellite must be detected and mitigated. One of the largest sources of error is the delay and interference on signals as they travel through the ionosphere. While the delay can be mitigated in many locations, the ionosphere

contains anomalies in equatorial and high latitude regions that make it difficult to accurately perform error correction. The effect of these anomalies on GNSS signals is referred to as scintillation. The aviation industry faces challenges at these locations around the world because of ionospheric scintillation. For this reason, further techniques need to be developed to provide the availability, accuracy, and integrity that is expected of GNSS [2] in these locations.

An aviation scenario is depicted in figure 1.1, where we have an aircraft approaching a runway for a landing using GPS satellites for navigation. The aircraft and ground based augmentation systems (GBAS) receive the satellite signals, and communicate with each other in order to provide the aircraft with more accurate satellite measurements to use while landing. With no irregularities in the ionosphere, GBAS have high functionality as seen on the path of the satellite signal on the left. However, the satellite's signals on the right hand side of the figure are scattered by these ionospheric anomalies, causing a loss of availability of these ground systems and a degradation of accuracy.

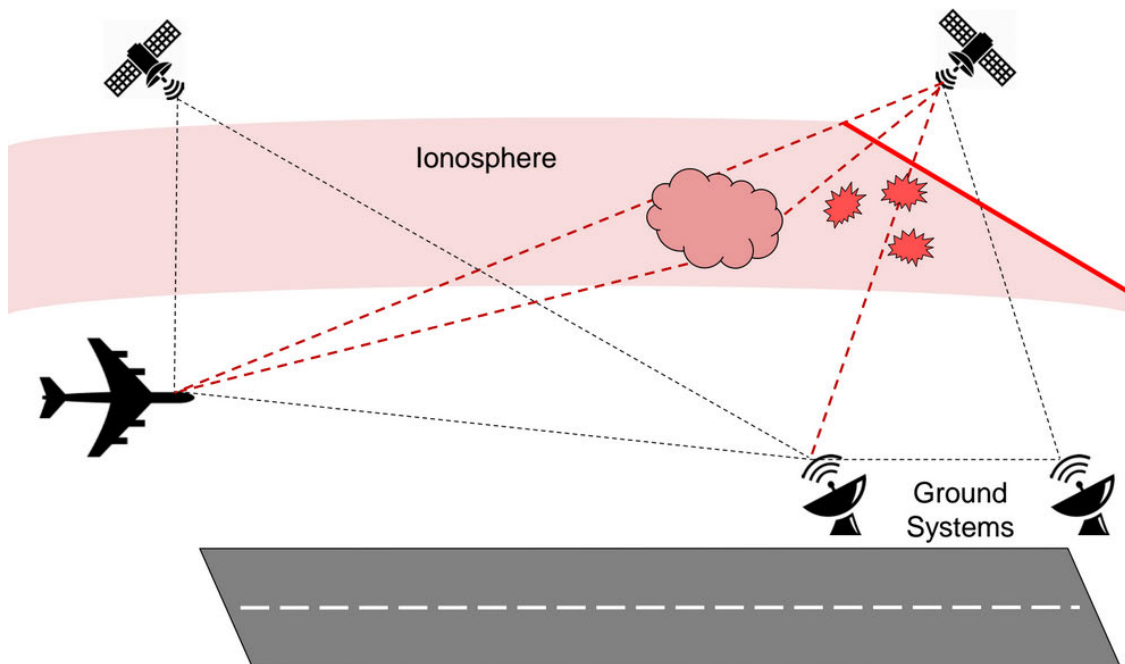


Figure 1.1: Aircraft approach using GPS and GBAS.

During a precision landing approach, there are several regulations set by the Federal Aviation Administration (FAA) that constitute the type of accuracy that is required by instrument landing systems (ILS), such as GBAS. These regulations come in three categories that are defined by two parameters for a plane landing: the decision height (DH), and runway visual range (RVR), which are shown in figure 1.2 and summarized in table 1.1. At the DH, a pilot will need to make a decision on whether to land the plane or delay the landing and circle back around. Different ILS are approved for each of the categories, where category III landings allow the instruments to guide the aircraft closer to the runway than category I landings. Currently, the use of GNSS-based GBAS is approved for category I approaches only, where the lateral accuracy requirement is 16 meters, and the vertical accuracy requirement is 7.6 meters [3]. If we can develop more robust and accurate systems, GNSS could be approved for category III approaches, where the vertical requirement is at the sub-meter level. It is not the intention of this thesis work to achieve the type of accuracy required for category III approaches, because the algorithms in this thesis consist of standard positioning techniques for a single receiver. In reality, arrays of receivers are used for more advanced techniques that are able to achieve much more accuracy. The analysis and methodologies presented here will offer insights and guidance for future development of accurate PVT solution under disturbed ionospheric conditions.

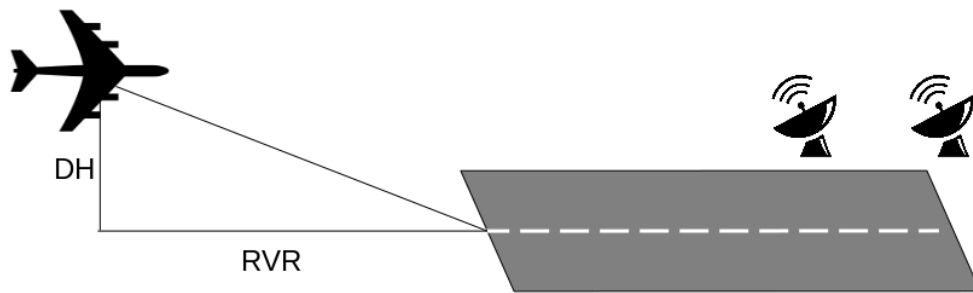


Figure 1.2: Decision height and runway visual range. Parameters for plane landing.

Due to restrictions set by the FAA, many of the industrial applications in the United States are restricted to only GPS in order to retain control of operations. To maintain

Table 1.1: Categories of ILS Approaches

Category	Minimum DH	Minimum RVR
I	200 ft (61 m)	1800 ft (550 m)
II	100 ft (30 m)	1000 ft (300 m)
III	< 100 ft (30 m)	< 1000 ft (300 m)

relevance with FAA regulations, the studies in this thesis will be confined to GPS. However, the topics and algorithms in this thesis are still applicable to other satellite constellations.

In addition to attempting to gain more accuracy in navigation solutions, this thesis could also be applicable to problems related to jamming and interference. Scintillation and interference can cause similar effects on signals that are often hard to distinguish. Therefore, if we were to treat jamming and interference as scintillation, these new scintillation-targeted algorithms could also be applied to reduce the impact of these problems as well.

The goal of this thesis is to evaluate the impact of ionospheric scintillation on carrier phase and pseudorange measurements, and to present several algorithms for mitigating and reducing errors in a standard navigation solution using a single receiver during ionospheric anomalies. First, ionospheric effects on GPS signals will be presented to clarify the problems that the industry faces. Then, variations on current algorithms as well as new approaches to reducing these problems will be derived, analyzed, and compared to conventional algorithms to determine the feasibility of application into existing systems. The following section explains the GPS fundamentals relevant to this work.

1.2 GPS Signals and Signal Structure

Calculating the receiver's position begins with understanding the signals being transmitted by the satellites. Older generation satellites transmit signals at two frequencies: 1.57542 GHz (L1), and 1.2276 GHz (L2). The L1 band contains a Course/Acquisition (L1 C/A) signal to be used by civilians, an encrypted precision code (L1P), and a restricted military signal. A new L1 civilian signal (L1C) is planned for launch this year (2017). The L2 band is composed of a relatively new civilian signal (L2C), encrypted precision code (L2P), and a

restricted military signal. Currently, 19 of the 32 satellites that comprise the GPS constellation transmit L2C, while all of them transmit L2P. The newest generation of satellites also transmit signals at a third frequency of 1.17645 GHz (L5), which is intended for aviation. At this time, 11 of 32 satellites transmit L5. The L1C and L5 signals are not yet considered operational due to the few number satellites transmitting these signals. For purposes of this thesis, L1 will refer to the L1 C/A signal. L2 will refer to either L2C or L2P, on the condition that L2C is favored over L2P.

The L1 signal is used extensively in this work, so it is important to point out its characteristics. Each GPS L1 signal consists of the modulation of a unique pseudorandom noise (PRN) code at a chipping rate of 1.023 MHz, a navigation data stream at 50 Hz, and a carrier at 1.57542 GHz to produce the signal in figure 1.3 below.

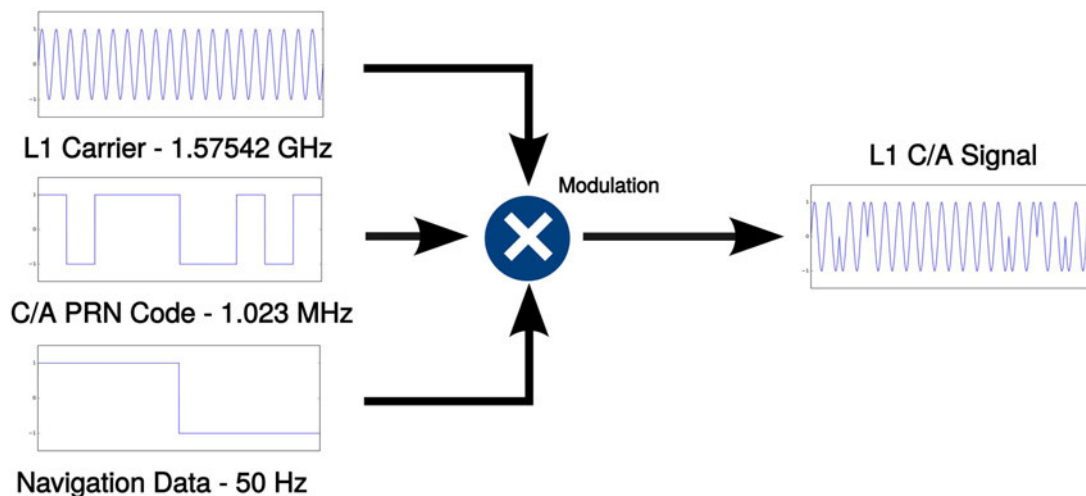


Figure 1.3: GPS L1 C/A signal block diagram.

The L2P signal is similar to L1 C/A, but the L2C signal is slightly more complex with a moderate-length code (CM), and a long code (CL) that are multiplexed together, and have a chipping rate of 1.023 MHz. The navigation data is only modulated with the CM code. The navigation data and is transmitted at 25 Hz, then encoded with forward error correction (FEC) code to convert it to a rate of 50 symbols per second (sps) [4]. This code is modulated with the L2 carrier at 1.2276 GHz to create the L2C signal in figure 1.4.

The navigation data on these signals gives relevant information about the satellite’s orbit and time stamps for the transmitted codes. The job of a GPS receiver is to continuously

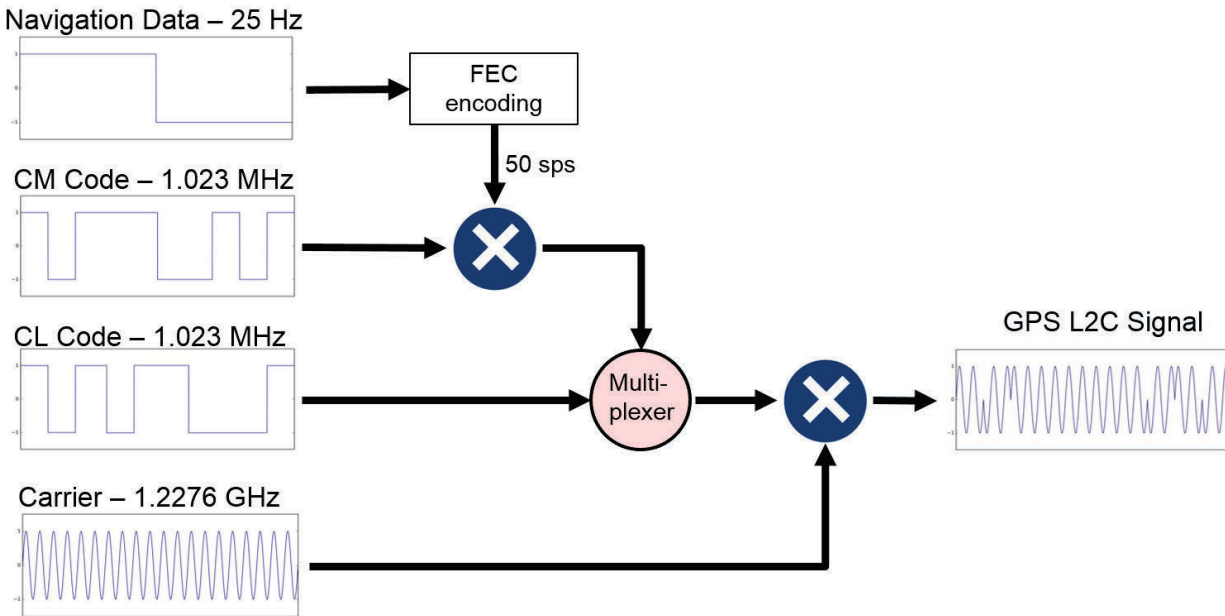


Figure 1.4: GPS L2C signal block diagram.

track the code phase and carrier phase. Code phase estimation allows for range measurement by making a fine adjustment to the time the signal was received from the time stamp of when it was transmitted. A range can be calculated by multiplying this time difference by the speed of light. Since the carrier frequency is roughly 1500 times the chipping rate of the code, tracking the carrier phase can produce more precise measurements with a great reduction in noise compared to the measurements from the code. The carrier signal cannot be time stamped, which results in relative range measurements that have an unknown integer ambiguity [5]. This means the range measurements from the carrier phase have high precision, but only a relative range accuracy, while the code’s range measurements have lower precision and an absolute range accuracy.

Due to many error sources on the code’s range measurements, we refer to them as the pseudorange. The full measurement model for the pseudorange in the unit of meters is shown in equation 1.1. Most of the error sources in these measurement models can be corrected for

using standard techniques, which will be discussed in this chapter, and in chapter 3.

$$\rho_f = r + \delta r + c(\delta t_r - \delta t_s) + c(b_r + b_s) + T + I_{\rho,f} + M_{\rho,f} + \epsilon_{\rho,f} \quad (1.1)$$

The preceding symbols are defined as

ρ_f : pseudorange [m]

r : true range from the satellite to the receiver [m]

δr : satellite orbit errors [m]

c : speed of light [m/s]

δt_r : receiver clock errors [s]

δt_s : satellite clock errors [s]

b_r : receiver hardware delay [s]

b_s : satellite hardware delay [s]

T : troposphere delay [m]

$I_{\rho,f}$: ionosphere delay [m]

$M_{\rho,f}$: multipath errors [m]

$\epsilon_{\rho,f}$: other unmodelled errors and noise [m]

and the subscripts f and ρ represent terms that are frequency dependent and unique to the pseudorange measurements, respectively. The measurement model for the carrier phase in units of meters, also known as the accumulated Doppler range (ADR), is shown in equation 1.2

$$adr_f = r + \delta r + c(\delta t_r - \delta t_s) + c(b_r + b_s) + T - I_{adr,f} + M_{adr,f} + \epsilon_{adr,f} + \lambda_f N_f \quad (1.2)$$

where the N is the integer ambiguity and λ is the wavelength at a particular frequency. The ionosphere causes an advance on the carrier signal rather than a delay, which is why the $I_{adr,f}$ term is negative as opposed to equation 1.1. The ADR in equation 1.2 is often referred to as the carrier phase in units of cycles. The straight-forward conversion from meters to cycles is shown in equation 1.3.

$$\phi_f = \frac{adr_f}{\lambda_f} \quad (1.3)$$

The pseudorange and ADR measurements for a single satellite are shown in the first subplot of 1.5. Notice the pseudorange measurements are on the order of 20000-25000 km.

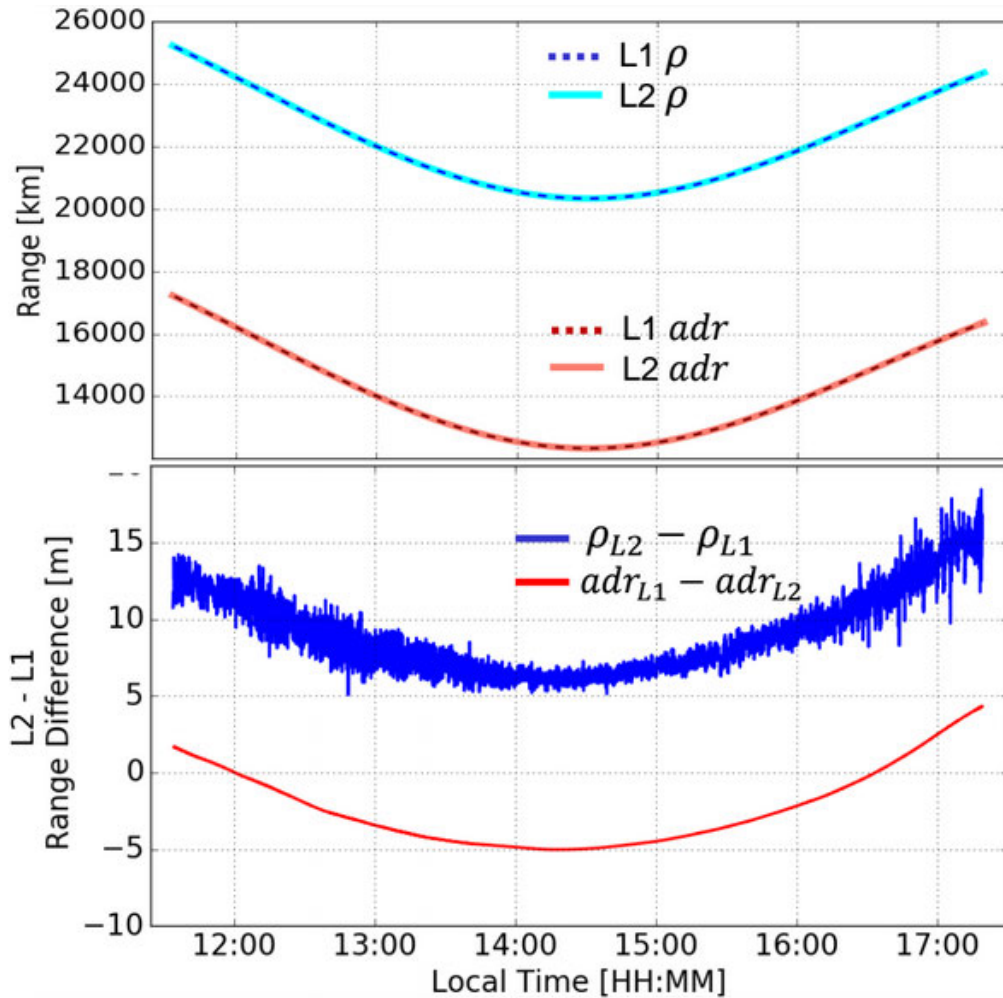


Figure 1.5: Pseudorange and ADR measurements. Top subplot: raw pseudorange (blue) and ADR measurements (red). Bottom subplot: dual-frequency difference of the pseudorange and ADR measurements. Data from PRN Jicamarca, Peru on 11/3/2014.

The ADR measurements have the same overall trend, but they have the integer ambiguity term from equation 1.2. The bottom subplot shows a difference of the pseudorange and ADR measurements between the L1 and L2 frequencies. This difference shows how much noisier the pseudorange measurements are than the ADR measurements. Techniques to yield the relative precision of the ADR measurements and absolute range accuracy of the pseudorange measurements are discussed in section 3.3. One other note is that the parabolic trend of

the bottom plot is due to the ionospheric delay on each frequency. When the satellite is at the horizon, the signal travels a longer distance through the ionosphere, which creates a larger separation in the range measurements between each frequency than when the satellite is overhead.

1.3 GPS Positioning

1.3.1 Trilateration

Using GPS for navigation is based on trilateration. If a user is at an unknown location, the basic idea of trilateration is that we can utilize known distances to reference points in order to pinpoint the user's location [4]. For the moment, visualize a two-dimensional (2D) plane with reference points P_1 and P_2 that have known locations (x_1, y_1) and (x_2, y_2) as shown in figure 1.6. Assume we also have accurate distance measurements r_1 and r_2 from the user to each one of the reference points. Only taking into account the measurement r_1 , the user could be located anywhere on the circle that is a distance of r_1 away from P_1 . Bringing in the second measurement puts the user at one of the two intersection points of the circles around P_1 and P_2 . To isolate the user's position to just one point, a third range measurement r_3 is needed from an additional reference point P_3 located at (x_3, y_3) . The intersection of all three circles reveals the user's location in this 2D coordinate system as the red triangle in figure 1.6. GPS works on the same principle. The reference points are the satellites, which constantly transmit information used to calculate their three dimensional (3D) position to users near Earth through the GPS ephemeris, which is part of the navigation data. Range measurements from the satellite to the receiver can be produced by multiplying the propagation time by the speed of light. These range measurements are the pseudorange from equation 1.1. Therefore, as long as there is a minimum of four satellites in view of the receiver, we can calculate a position for the user at the intersection of four spheres as seen in figure 1.7. In reality, there are many error sources that must be accounted for in order to adjust range measurements to produce an accurate position. Traditional methods of

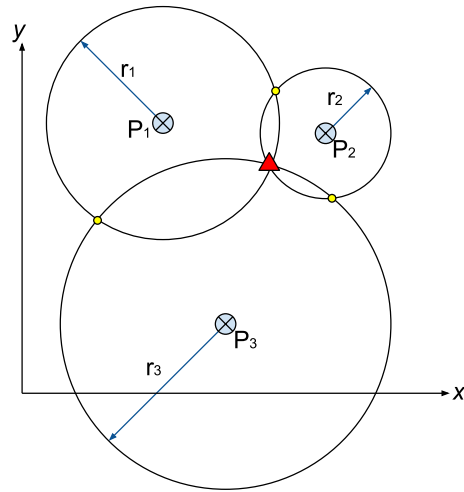


Figure 1.6: 2D trilateration. Reference points are shown in light blue, and the user's location is shown as the red triangle.

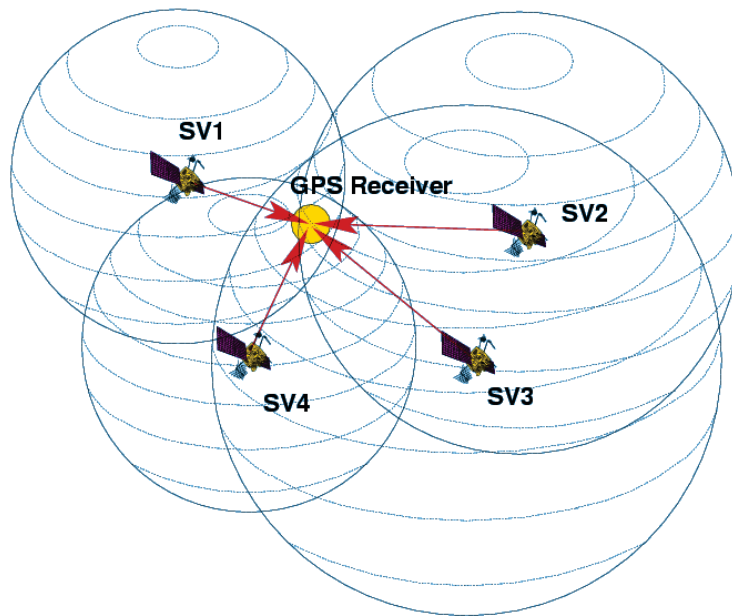


Figure 1.7: 3D trilateration. [6]

calculating the receiver's position and correcting range errors are briefly explained in sections 1.3.2 - 1.3.6.

1.3.2 Ionospheric Delay

One of the largest errors on GPS range measurements is the signal delay as it propagates through the ionosphere. The ionosphere is the region above the Earth at altitudes of about 50 km to 1000 km containing a mixture of ions and electrons that cause a group delay on radio frequency (RF) signals [7]. The ionosphere can be separated into several different regions according to the electron density at various altitudes, but we will look at the ionosphere as one integrated region for the purpose of calculating the ionospheric delay. This delay is typically on the order of 5-120 meters depending on the latitude, time of day, and elevation angle of the satellite [4]. Since the ionospheric delay is dependent on the frequency of the propagating signal, the L1 and L2 GPS frequencies are utilized to estimate the ionospheric delay. This process begins with calculating the total electron content (TEC), which is defined as the total number of electrons in a tube of 1 m² cross section from the receiver to the satellite [4]. The TEC is computed using the L1 and L2 frequencies and range measurements in equation 1.4.

$$TEC = \frac{f_{L1}^2 f_{L2}^2}{40.3(f_{L1}^2 - f_{L2}^2)}(\rho_{L2} - \rho_{L1}) \quad (1.4)$$

While the TEC is useful for atmospheric studies, it is converted to a range delay on a particular frequency for purposes of positioning using equation 1.5.

$$I_\rho = \frac{40.3TEC}{f^2} \quad (1.5)$$

Subtracting this delay from the measured pseudorange mitigates ionospheric effects.

1.3.3 Tropospheric Delay

The troposphere is defined as the region from 7-17 km above the Earth's surface containing about 90% dry gases and 10% water vapor. The signal delay due to the dry and wet conditions can contribute 2-25 m of range error [8]. Since all GPS frequencies propagate through the troposphere with a common delay, dual frequency correction techniques cannot be used as they were to find the ionospheric delay [4]. Models must be used to make this

correction; the Hopfield model was used in this study. This model is based on dry and wet zenith delays $T_{z,dry}$ and $T_{z,wet}$. The delay along each satellite path is dependent on the elevation angle, which leaves the total tropospheric delay T in meters to be calculated from the dry and wet zenith delays, multiplied by dry and wet elevation mapping functions m_{dry} and m_{wet} as in equation 1.6.

$$T = T_{z,dry} \cdot m_{dry}(el) + T_{z,wet} \cdot m_{wet}(el) \quad (1.6)$$

The dry and wet zenith delays are calculated with equations 1.7 and 1.8 where

P_0 : total pressure [mbar]

h_d : height where the dry refractivity is zero [km]

T_0 : temperature [K]

e_0 : partial pressure due to water vapor [mbar]

h_w : height where the wet refractivity is zero [km]

$$T_{z,dry} = 0.0776 \frac{P_0 h_d}{5T_0} \quad (1.7)$$

$$T_{z,wet} = 0.373 \frac{e_0 h_w}{5T_0^2} \quad (1.8)$$

In this study, values for the temperature, pressure, mapping functions of the elevation angle for dry and wet delays are shown in the following equations.

$$m_{dry}(el) = \frac{1}{\sin(el) + \frac{0.00143}{\tan(el)+0.0445}} \quad (1.9)$$

$$m_{wet}(el) = \frac{1}{\sin(el) + \frac{0.00035}{\tan(el)+0.017}} \quad (1.10)$$

This is a standard technique for correcting tropospheric delay, and detailed derivations of the Hopfield model, mapping functions, and additional models can be found in [4].

1.3.4 Hardware Biases

An error source on the range measurements that must be accounted for in any advanced receiver is the hardware bias. Put simply, this is the time delay on the signals as they travel through the hardware of the satellites and receiver. There are two types of hardware biases: one that is caused by the different carrier frequencies of GPS signals, and another that is caused by the different code modulations on the signals within each frequency.

The inter frequency bias (IFB) is the difference in delay of two frequencies within the satellite and receiver hardware. The magnitude of most satellite IFBs is on the order of a few ns, but can reach up to 12 ns which can introduce several meters of range error [9]. This needs to be corrected individually on each satellite measurement.

Each GPS signal within the same frequency uses different modulating codes. The modulation on each signal corresponds with different pseudorange measurements. For example, the L1 C/A signal has a different coding scheme than the restricted L1P signal. The different modulations cause contrasting delays in the hardware, which is known as a differential code bias (DCB) [5]. Currently, the largest DCB value from a GPS satellite is around 2.6 ns.

These measurement calibrations are needed to ensure all signals are synchronous. While rough corrections are provided by the GPS ephemeris, we can get more accuracy by using an outside resource. The Center for Orbit Determination in Europe (CODE) provides monthly IFB and DCB corrections for satellites that are publicly available online. It is only necessary to update the biases month-to-month because the errors are fairly stable over time with no rapid fluctuation [9].

While the IFB and DCB corrections are made for each individual satellite, they are typically estimated together as one hardware bias within the receiver's hardware. CODE also provides these receiver hardware bias estimates for their network of receivers around the world. From the latest DCB file from CODE, the largest hardware bias out of all of their receivers was found to be 37.7 ns, but the majority of receivers had a bias less than 15 ns. Receiver hardware biases for the receivers deployed by the CSU GPS Lab were roughly

estimated with the algorithm presented in [5]. These receivers all had hardware biases less than 5 ns, which translates to less than 1.5 m of error. This algorithm will not be explained in detail because the correction of our receiver hardware biases does not have a large effect on the positioning algorithms in this thesis. However, the satellite corrections are necessary.

1.3.5 Multipath Error

Another error source in the range measurements includes multipath, or the reception of the direct signal, and the reflection of the same signal from the ground or other structures. This results in the sum of the signals, and thus, errors in the range measurements. The distinguishing factors on reflected signals are that they have a delay due to the longer distance they travelled, and they are often a weaker version of the direct signal. Typically, multipath error on the pseudorange measurements is 1-5 m, while the multipath error on the carrier phase is typically 1-5 cm [4].

Multipath is often mitigated through antenna design. Many GNSS antennas are designed to weaken the signals that are received from the underside of the antenna (indicating a reflection from the ground). Since it is not practical to only rely on antenna design to mitigate multipath, the best method is to perform carrier-smoothing of the pseudorange measurements. This way, we will only see the multipath effects of the carrier phase, which are comparatively negligible.

1.3.6 Position Estimation Using Pseudoranges

Correcting the pseudorange from each individual satellite in view for the ionospheric delay, tropospheric delay, hardware biases, multipath, and receiver clock offsets is critical to achieving the range accuracy needed to calculate the user position. Clock corrections will be briefly discussed in this section along with the overall positioning algorithm using the least squares estimation (LSE) technique based on a linear model [4].

Similar to trilateration, the LSE technique needs two important parameters: the position of each satellite, and the distance to each satellite. For these, we use the satellite

coordinates calculated from orbit parameters broadcast by the GPS ephemeris, and the corrected pseudorange measurements. Along with the satellite positions, the GPS ephemeris also transmits important information about the satellite's clock offset from the GPS time standard. Detailed calculations of the satellite position can be found in [10].

Denote the vector $\vec{x}_u = (x_u, y_u, z_u)$ as the unknown coordinates of the user, and the vector $\vec{x}^s = (x^s, y^s, z^s)$ as the known satellite coordinates at a particular epoch. This leaves the true geometric range from the user to the satellite to be

$$r = \sqrt{(x^s - x_u)^2 + (y^s - y_u)^2 + (z^s - z_u)^2} = \|\vec{x}^s - \vec{x}_u\| \quad (1.11)$$

After neglecting hardware delays, assuming precise satellite coordinates, and applying ionosphere, troposphere, and satellite clock corrections, the corrected pseudorange from equation 1.1 can be written as

$$\begin{aligned} \rho_c &= r + c(\delta t_u) + M_\rho + \epsilon_\rho \\ &= \|\vec{x}^s - \vec{x}_u\| + b + \varepsilon_\rho \end{aligned} \quad (1.12)$$

Now the remaining error on the corrected pseudorange only contains multipath and unmodelled errors. These errors have been grouped together in the ε_ρ term. The receiver clock bias $c(\delta t_u)$ will be re-written as b for consistent, simplified notation. Without much control over ε_ρ , the goal is to estimate \vec{x}_u and b . This is where the linear model becomes of use. Following the derivation in [4], we can make this estimation by using an LSE solution for an overdetermined system in equation 1.13. In this equation, the geometry matrix \mathbf{G} is derived from direction vectors between the estimated receiver position and the position of each satellite.

$$\begin{bmatrix} \delta \vec{x} \\ \delta b \end{bmatrix} = (\mathbf{G}^T \mathbf{G})^{-1} \mathbf{G}^T \delta \vec{\rho} \quad (1.13)$$

This will give us the best estimate of a solution in terms of a least squared error minimization based on initial position and receiver clock estimates. For more accuracy, it is necessary to update our initial estimates with equation 1.14 and continue to iterate through the process

until the change between successive iterations falls below a set threshold. Typically, it takes 2-4 iterations for convergence [4].

$$\begin{aligned} \vec{x}_0 &= \vec{x}_0 + \delta\vec{x} \\ b_0 &= b_0 + \delta b \end{aligned} \tag{1.14}$$

1.4 Receiver Reference Generation Using Precise Point Positioning (PPP)

Throughout this thesis, the position error is analyzed, and it is necessary to explain how to accurately determine position errors. We know each receiver's approximate stationary coordinates. But with the help of precise point positioning (PPP) services, we are able to pinpoint each receiver's precise location with centimeter accuracy.

PPP is a technique that is applied in post processing that uses the most accurate resources available to calculate the receiver's position. Carrier phase and pseudorange observables are inputs to most PPP algorithms. Precise satellite position and clock data is taken from an online resource, which produce more accuracy than the GPS ephemeris. Each measurement is carefully analyzed for errors before being used in the algorithms, and extraneous measurements are discarded. The ability to use information about future measurements from multiple constellations, advanced post-processed filtering and optimization techniques, and outside resources gives PPP the most accuracy of any positioning algorithm for a static receiver [11].

There are several online PPP services available to anyone with GNSS receiver data. Two services were used to pinpoint the location of our receivers. The first was the Canadian Spatial Reference System (CSRS) - PPP, and the second was the GNSS Analysis and Positioning Software (GAPS), which was developed by the University of New Brunswick (UNB). Both services allow the upload of a data file with GNSS observables, and then precise results are returned to the user via email.

For each receiver, several data sets from various months and years were uploaded during times of low ionosphere activity to each of these services. A static "surveyed" position was produced for each upload and each PPP service. Each surveyed receiver position was in close agreement between services and data sets. To be thorough, all results were averaged at each location to determine the final receiver coordinates to be used for a comparison in this study. The error of our positioning algorithms at every point can be found by calculating the distance from the receiver's final static location.

1.5 Introduction to Ionospheric Scintillation

Most error mitigation techniques are very effective under nominal environmental conditions. However, in equatorial and high latitude regions, the ionosphere contains anomalies within several hours of local midnight. RF signals are scattered when they propagate through these anomalies. As a result, a GPS receiver will see amplitude and phase fluctuations on the incoming signal, which is known as ionospheric scintillation [12–14].

Typically there are two indicators that are used to quantify the severity of scintillation: the amplitude fluctuation indicator (S_4), and the phase fluctuation indicator (σ_ϕ). S_4 is calculated using the signal intensity (SI). This starts with acquiring the in-phase (I) and quadrature-phase (Q) samples that are obtained during carrier phase tracking. The Septentrio PolaRxS receiver used in this study outputs I and Q samples at a rate of 100 Hz. With these samples, the narrow-band power (NBP) and wide-band power (WBP) can be calculated through equations 1.15 and 1.16. In order to maintain output samples every 20 ms (50 Hz), we sum over 2 consecutive samples by setting M equal to 2 [15].

$$NBP = \left(\sum_{i=1}^M I_i \right)^2 + \left(\sum_{i=1}^M Q_i \right)^2 \quad (1.15)$$

$$WBP = \sum_{i=1}^M (I_i^2 + Q_i^2) \quad (1.16)$$

With these calculations, the raw SI is found through the subtraction of the WBP from the NBP as in equation 1.17.

$$SI_{raw} = NBP - WBP \quad (1.17)$$

When S_4 is calculated, we need to remove the low frequency trend in SI_{raw} due to the satellite dynamics relative to the receiver. A 6th order low-pass Butterworth filter with a 1 Hz cut-off frequency is used to find the trend in SI [15], which will be designated as SI_{filt} . Equation 1.18 defines the normalized SI that is used to calculate the S_4 index.

$$SI = \frac{SI_{raw}}{SI_{filt}} \quad (1.18)$$

S_4 is then calculated in equation 1.19 as the standard deviation of the SI, normalized by the average SI [13, 16].

$$S_4 = \sqrt{\frac{\langle SI^2 \rangle - \langle SI \rangle^2}{\langle SI \rangle^2}} \quad (1.19)$$

The σ_ϕ calculation begins with the carrier phase measurements (ϕ). First, the trend due to the satellite's geometry must be removed. This is done with a 6th order high-pass Butterworth filter with a cut-off frequency of 0.1 Hz [17]. While there is some debate about various detrending methods, the Butterworth filter is the frequently adopted method for calculating σ_ϕ [15]. Once detrended, σ_ϕ can easily be calculated with the standard deviation in equation 1.20 [13, 14].

$$\sigma_\phi = \sqrt{\langle \phi^2 \rangle - \langle \phi \rangle^2} \quad (1.20)$$

Both the σ_ϕ and S_4 calculations in this study were done with a sliding window integration time of 10 seconds.

It is important to monitor the amplitude and phase because large fluctuations can cause the receiver to lose lock of signals. Fluctuations in the amplitude can correspond to low signal power, making the signal difficult to track. Rapid fluctuations in the phase can lead to cycle slips. A cycle slip is defined as a discontinuity in the carrier phase measurement [18]. In addition, when large phase fluctuations occur, carrier phase measurements are often not able to be produced while pseudorange measurements remain intact [19–21]. Chapter 2

will further discuss the effect scintillation has on pseudorange and carrier phase measurements including cycle slips and dropped measurements, as well as the seasonal and hourly dependence for different locations around the world.

1.6 Prior Research

Many techniques have been developed with the intent of mitigating the effects of ionospheric scintillation on GNSS signals. A majority of research has gone into the tracking stage of a GPS receiver. If the signal is tracked with more accuracy, higher quality measurements can be produced during scintillation. This thesis focuses on the measurements that are output from the tracking stage, but it is important to note that robust tracking is fundamental to the work presented in this thesis. Examples of improvements on traditional tracking algorithms during scintillation can be found in [22, 23].

Prior research thoroughly explains the problems that are at hand with GPS positioning during scintillation. There have been a few techniques presented in the past to help improve the navigation solution at the measurement level. The most prominent technique is to add weights when calculating the receiver's position. This involves the introduction of a weight matrix to equation 1.13. [24] discusses the relationship between dropped measurements during scintillation versus the elevation angle of the satellite. Scintillation effects often appear more severe at lower elevations since the signal travels through more of the ionosphere, and multipath effects are usually stronger. Applying the weight matrix gives the satellites at higher elevations a stronger influence in the overdetermined system of equations to minimize scintillation effects on the satellites at low elevations.

Along the same lines, a second technique presented by [19] discusses the possibility of weighting the LSE solution by the scintillation indices through the application of various ionospheric scintillation models. Further approaches are explored by this author which weight the LSE solution by code-carrier divergence. These positioning solutions were able to achieve 17 - 38% improvement in accuracy. This paper also explains how applying these weights can

help reduce the impact of problematic ambiguity resolution during phase scintillation, which we will see is a big part of accurate positioning.

Another technique that has been used in the past is to repair carrier phase discontinuity induced by scintillation. There are many different ways to detect cycle slips, but repairing cycle slips can be a challenge, especially on a highly dynamic platform. Past research indicates that cycle slip repair is essential to maintaining position solution accuracy. Discussions in [25] were helpful for the cycle slip repair techniques used in this thesis.

Previous research such as the paper presented in [20] establishes thresholds for σ_ϕ in which the carrier phase tracking is considered to have lost lock. This impacts the geometric dilution of precision (GDOP), which is a measure of the geometric layout of the visible satellites. Thresholds from this research will be used to our advantage in the development of algorithms in chapter 3.

Prior studies often discard measurements from semi-low elevation satellites with the assumption that they will be problematic. Ideally we still want to use measurements from these low elevation satellites, as they have an important role in the GDOP. It is crucial to classify the scenarios where we can discard satellite measurements without impairing the position solution. This thesis will tackle this assumption by using a smaller elevation mask, and analyzing the GDOP. In addition, many techniques that have been used in the past do not directly address positioning improvements during ionospheric scintillation. This thesis will apply them in a way that specifically adapts to ionospheric scintillation. Another problem with some of the previous work is that the use of ionospheric scintillation models may be hindered by accuracy, and are too general for real-time processing. Therefore, algorithms still need to be developed and improved to get the best performance out of GPS in real time under all conditions. The following section clearly describes the goals of this thesis, and how it will contribute to current research.

1.7 Contributions of Thesis Research

This thesis aims to improve current GPS receiver software during strong scintillation events. The overall contributions of this thesis to the field are as follows:

- Further understand the impact of scintillation on GPS signals and positioning algorithms using real scintillation data
- Evaluate and compare typical carrier-smoothing algorithms, and propose a new method of real time carrier-smoothing, which utilizes advantageous properties of two common techniques to create a high-performance hybrid technique
- Develop algorithms that improve upon typical positioning algorithms during scintillation by using approaches such as repairing cycle slips, substituting pseudorange measurements for carrier phase measurements, weighting the positioning solution, and completely excluding scintillating satellites from the navigation processing
- Maintain algorithm simplicity for the potential implementation into existing receivers, and easy approval from regulatory organizations, such as the FAA
- Evaluate the performance of these algorithms, and provide a statistical comparison

1.8 Thesis Organization

This thesis contains five chapters. Chapter 1 provides background information for GPS positioning algorithms and scintillation. Chapter 2 contains a more detailed discussion on scintillation, the effect it has on GPS signals, and a description of our data collection systems. More advanced techniques and methods intended to mitigate scintillation effects are derived in chapter 3. Results using real scintillation data are shown and interpreted in in chapter 4. A summary, conclusions, and future work is discussed in the last chapter.

CHAPTER 2

IONOSPHERIC SCINTILLATION

This chapter discusses the characteristics of ionospheric scintillation, and how GNSS signals are affected. A study is also performed about the seasonal and hourly dependence of scintillation at equatorial regions. Understanding ionospheric scintillation will give intuition on when and how to mitigate its impact. This chapter is split into four sections which briefly discuss the data collection systems, the morphology of scintillation, common problems on GPS signals due to scintillation, and how these problems impact the position calculation.

2.1 Data Collection

To most effectively study ionospheric scintillation, data is collected at a variety of locations around the world where scintillation typically occurs. The CSU GPS Laboratory has deployed a network of ionospheric scintillation monitoring and data collection systems. Figure 2.1 shows where these data collection systems are scattered over the world, as well as planned sites for future studies. The geomagnetic equator and relevant geomagnetic latitudes are included to justify the location of these systems for scintillation studies. Each of the locations used in this study have a data collection system that holds a Septentrio PolaRxS receiver and a series of Universal Software Radio Peripherals (USRP) devices. The Septentrio receivers are set up to collect data from most satellite constellations. Carrier phase and I and Q correlator outputs are logged at the high rate of 100 Hz, while other common observables such as the pseudorange and carrier-to-noise ratio (C/N_0) are calculated and recorded at 1 Hz. The USRP radio front ends continuously collect raw intermediate frequency (IF) data into a circular buffer. When scintillation is detected, the IF data is stored [26]. Raw IF data is used by the GPS lab to develop advanced tracking algorithms.

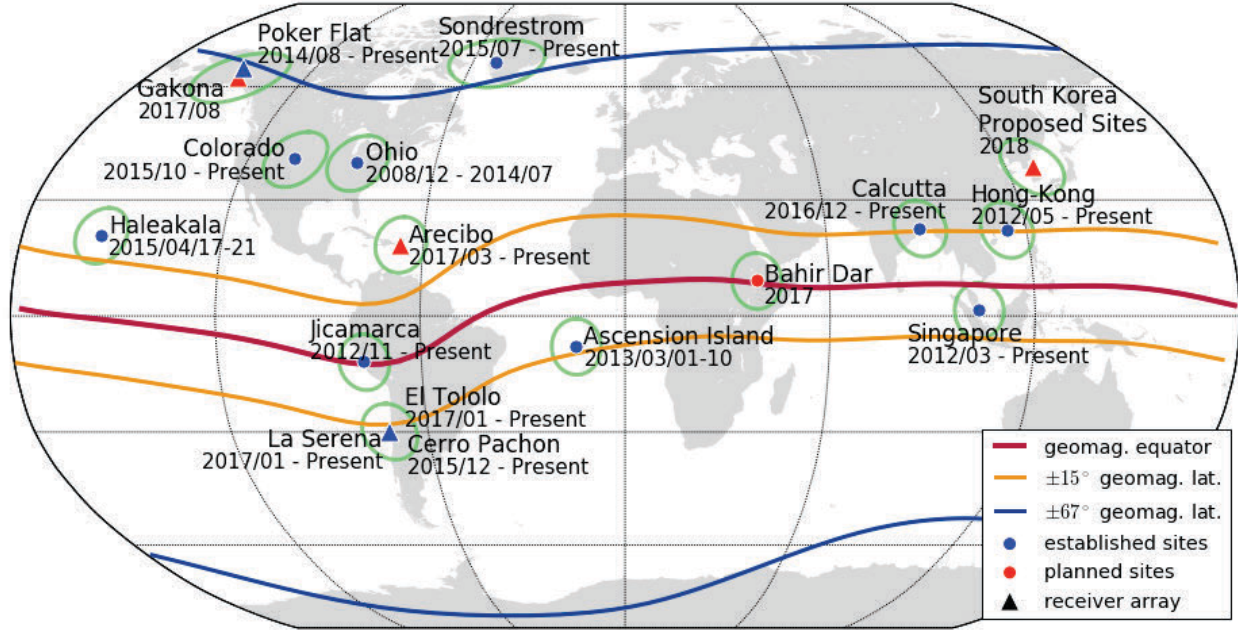


Figure 2.1: GPS Lab data collection systems.

A majority of the data that is publicly available on world-wide GPS networks is logged at 30 second increments, which makes our data collection systems more advantageous for research related to positioning errors.

2.2 Equatorial Scintillation Morphology

Ionospheric scintillation is a significant problem for radio signals around the geomagnetic equator and in high latitude auroral zones [27]. In contrast, much smaller phase and amplitude fluctuations in middle latitude regions are easily handled by most receivers [28]. Understanding how, where, and when severe ionospheric scintillation occurs is vital for developing algorithms intended to improve receiver performance in all geographic locations.

Scintillation is dependent upon a variety of factors including solar and geomagnetic activity, frequency of the radio wave, season, geodetic latitude, and time of day. In the equatorial region, ionospheric irregularities form large upward moving plasma bubbles, leaving behind smaller irregularities (up to tens of kilometers) that cause the diffraction of radio signals [29]. This is extremely difficult to model accurately because the true variations of the ionosphere

are unpredictable [27]. However, data driven research helps us understand hourly, monthly, and yearly patterns of scintillation occurrence.

Using data from Peru and Ascension Island, the study in [28] found increased scintillation activity near the equinoctial months. In addition, scintillation activity was found to be most common after local sunset, and more frequent during magnetic storms at high latitudes. This study was performed with a series of non-navigation satellites transmitting at a wide range of frequencies. These findings were later confirmed for GNSS constellations in various other studies, including [29]. Peak hours of scintillation were found to be in the evening hours before midnight with a large increase in activity around equinoxes, which is consistent with previous studies.

The GPS Lab has been collecting data from Jicamarca, Peru since late 2012. Morphology studies were performed with our new data to ensure it is consistent and accurate when comparing to previous studies. Figure 2.2 below shows the hourly and monthly dependencies of amplitude scintillation. For each day of data, the mean S_4 over all visible satellites was calculated. We get a better idea of how many satellites were experiencing strong scintillation by taking the mean, and it also helps to eliminate outlying measurements that were missed when filtering out poor measurements from of these data sets. From the calculated mean, the maximum value was plotted for each hour in the day. From this heatmap, we can clearly see more amplitude scintillation activity from February to April, and September to December, or near the equinoxes. We see no activity in the Summer months, and little activity through the Winter. In addition, the majority of scintillation activity happens between 19:00 and 2:00 local time (LT), which are the hours following the local sunset. This experiment was repeated while focusing on the phase scintillation activity, and is depicted in figure 2.3. We see the same result with σ_ϕ in the sense that phase fluctuations are more frequent around the equinoxes and in the hours following local sunset. This also implies a correlation between amplitude and phase scintillation near the geomagnetic equator. A direct comparison of S_4 and σ_ϕ (in radians) for one day of data in Jicamarca is displayed in figure 2.4. This

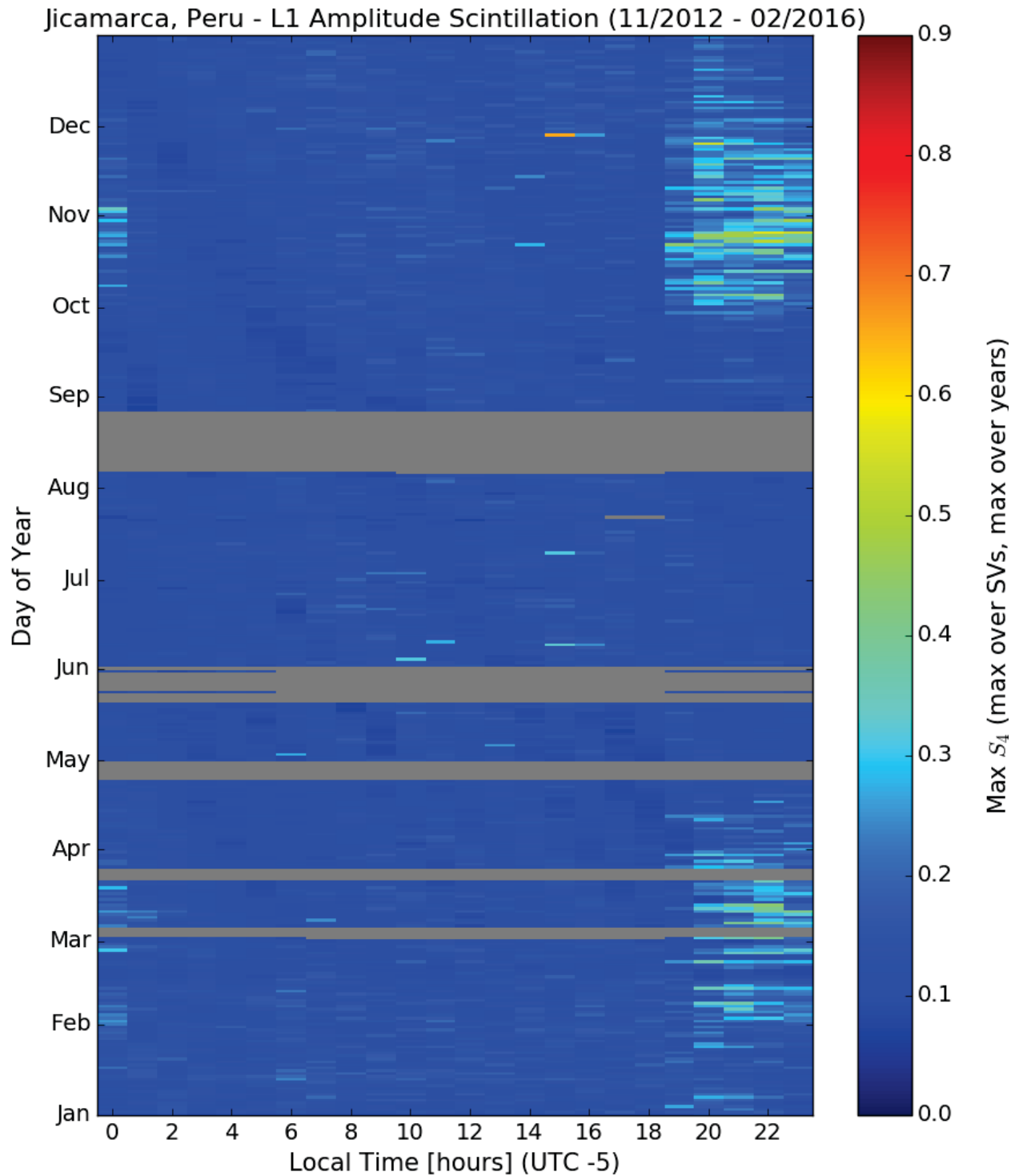


Figure 2.2: Jicamarca, Peru yearly and hourly S_4 dependence. Maximum hourly L1 S_4 values after taking the mean across all satellites. The maximum value is used for days that overlap from year to year. The gray coloring indicates data outages.

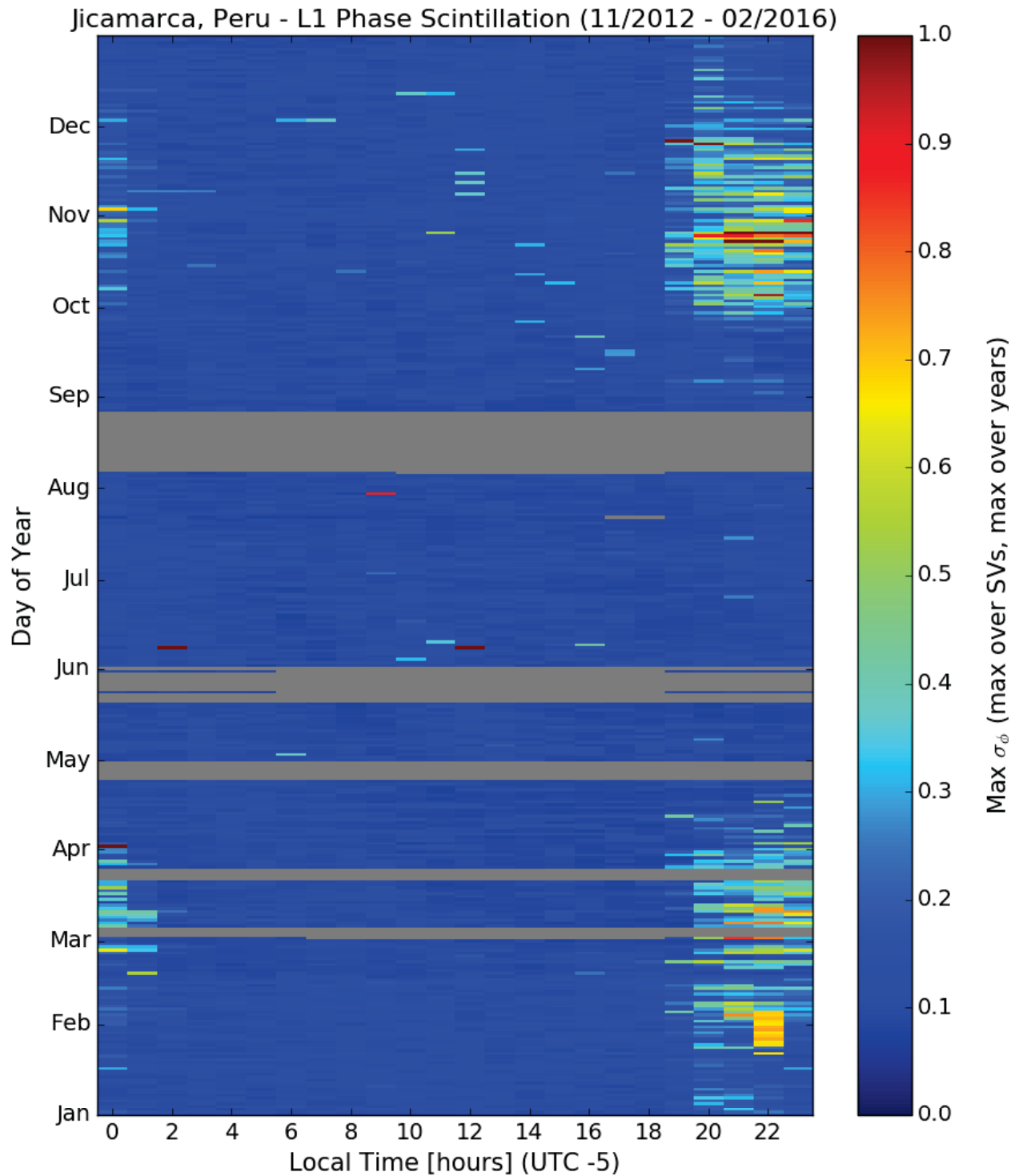


Figure 2.3: Jicamarca, Peru yearly and hourly σ_ϕ (radians) dependence. Maximum hourly L1 σ_ϕ taking the mean across all satellites. The maximum value is used for days that overlap from year to year. The gray coloring indicates data outages.

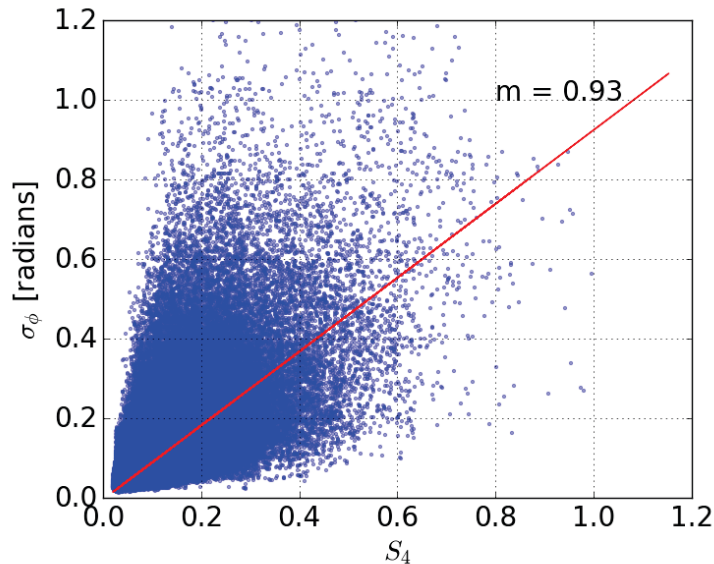


Figure 2.4: Jicamarca, Peru σ_ϕ versus S_4 . Relationship of L1 S_4 and σ_ϕ (radians) in Jicamarca, Peru on 11/3/2014. All satellites and all scintillation measurements for this day are included.

direct plot of the scintillation indices confirms a strong relationship of phase and amplitude scintillation for this equatorial data set with a linear correlation of 0.93. Studies presented in [30] selected 15 segments of scintillation data from Jicamarca, Singapore, and Hong Kong, which are all within 15 degrees of latitude of the geomagnetic equator. During only these 15 satellite passes with strong scintillation, a smaller linear correlation of 0.70 was reported. The difference of the correlation in these two studies is due to the different data sets used. Here, we have only used one day of data for all satellites, and the other study individually selected specific satellite passes in multiple locations. Both studies still show a relationship between S_4 and σ_ϕ near the equator.

Furthermore, the occurrence frequency of scintillation was shown to be related to solar activity, with more intensity during years that have a high number of sun spots [31]. All of the Peru data was grouped into each season, and plotted as a timeline in the figure 2.5. This figure shows the percentage of days in each season that contained a scintillation event defined by thresholds of 0.2 for S_4 and 0.2 radians for σ_ϕ . In addition, sunspot numbers were

averaged for each season and plotted. Solar cycle sunspot number data was provided by the National Oceanic and Atmospheric Administration (NOAA). While some of the seasons

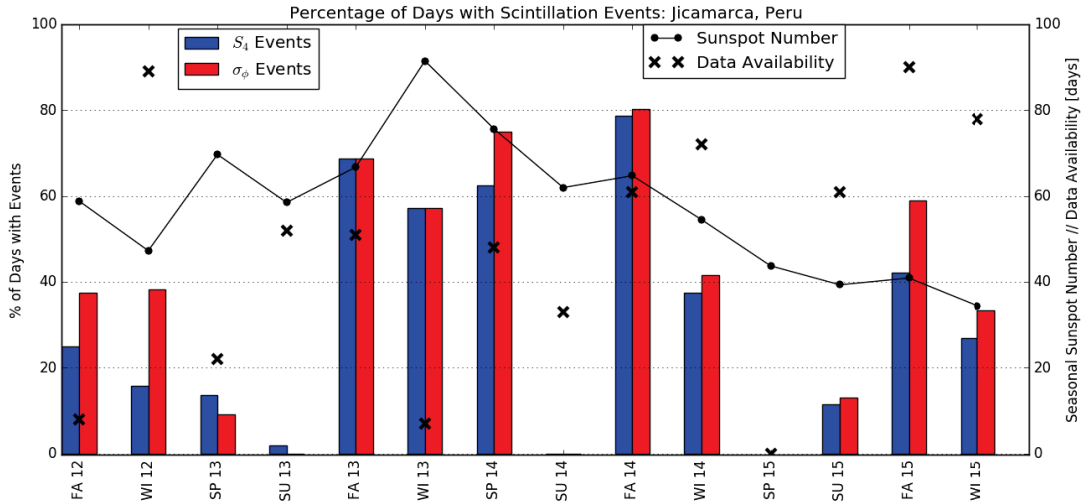


Figure 2.5: Jicamarca, Peru seasonal scintillation events. Percentage of days with a scintillation event defined by thresholds of 0.2 for S_4 and 0.2 radians for σ_ϕ . Sunspots are averaged for each season, and the data availability for each season is shown by a crossed marker.

are slightly misleading due to low data availability, the seasons with the equinoxes (Fall and Spring) show increased scintillation activity, and a null in the Summer months. The percentage of days with scintillation events (which were defined by relatively low thresholds) generally follows the trend of the sunspot number. The months during the peak of the sunspots is associated with an increase in activity while it seems to subside as the time line approaches 2016. Also, the number of S_4 events in each season is agreeable with the number of σ_ϕ events. This is further justification that the conclusion from figure 2.4 holds true for all of the Peru data.

A similar study using our high latitude Alaska data was performed in [13], which showed that high latitudes are more closely related to the sunspot number as well as geomagnetic activity. The conclusions of these morphology studies have already been defined in cited literature, but they were necessary to ensure all of our data follows the established patterns. This agreement builds confidence that any algorithms tested on this scintillation data will be consistent with similar regions and different data collection systems.

2.3 Scintillation Effects on GPS Signals and GPS Positioning

The previous section describes why and when scintillation occurs, and this section shows how scintillation negatively affects GNSS measurements, and how these measurements impact the position solution. Scintillation results in three primary problems with the ADR measurements that are used for positioning: cycle slips, dropped measurements, and phase scintillation induced phase error. Refer to figure 2.6 below, which shows these three primary problems with the ADR, some approaches that can be taken to mitigate each one of the problems, and algorithms that were developed based on the approaches. The following sections (2.3.1 - 2.3.3) discuss each of these problems. The approaches and adaptive algorithms will be covered in later chapters.

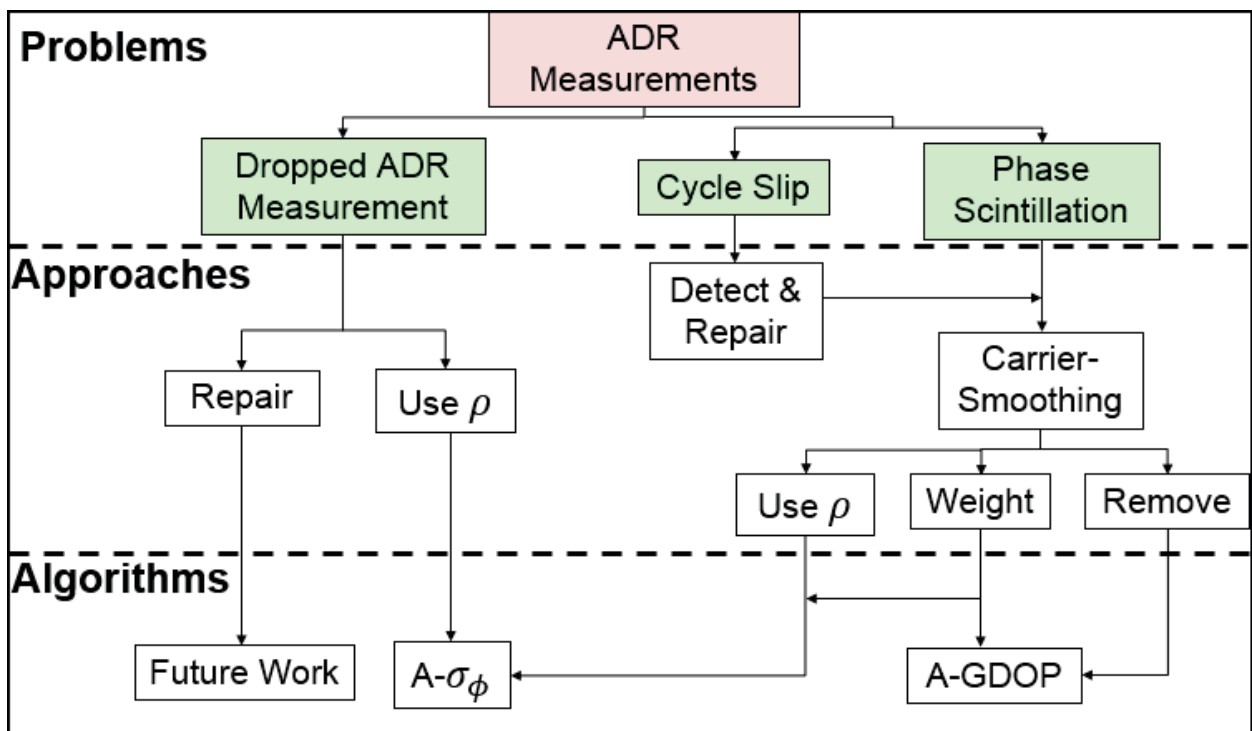


Figure 2.6: Overview of ADR measurement problems. Problems, mitigation approaches, and algorithms. The blocks in green are covered in this section.

2.3.1 Cycle Slips

To begin with explaining the problems of cycle slips, we need to understand what a cycle slip is. As stated in [18], a cycle slip can be defined as carrier phase measurement discontinuity. Cycle slips occur when the carrier phase measurement on a particular frequency suddenly jumps by an integer number of cycles. This happens during the temporary loss-of-lock and re-acquisition of the tracked signal due to deep amplitude fading, low signal-to-noise ratio (SNR), or large phase fluctuations, resulting in a drastic change in the range measurement in between measurements. These large changes in the range measurements from a satellite to a receiver are problematic for calculating the receiver position.

Cycle slips are often detected and viewed using a dual-frequency difference of the ADR measurements. In figure 1.5, we showed this difference for a single satellite pass. This same L2 - L1 range difference is shown in figure 2.7 by different colored lines for every satellite pass throughout an entire day. These ADR measurements have "smoothed" the noisier pseudorange measurements shown in the background in light blue. Methods to do this carrier-smoothing are discussed in chapter 3. Cycle slips are fairly easy to distinguish

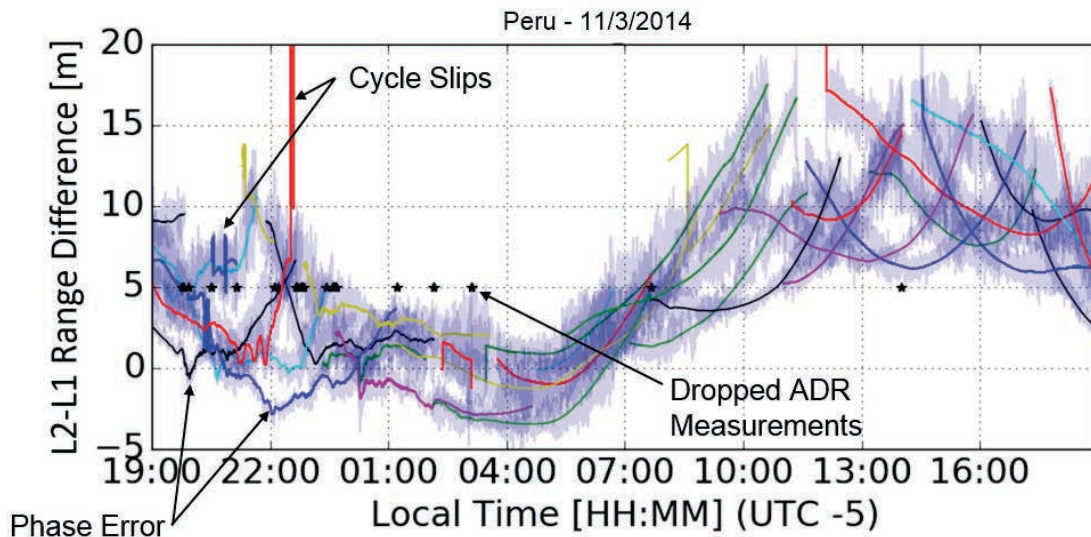


Figure 2.7: Peru ADR difference. L2 - L1 unsmoothed pseudorange measurements (light blue) and carrier-smoothed pseudoranges (colored) displaying cycle slips and phase fluctuations at Jicamarca, Peru on 11/3/2014. Points that contain a pseudorange measurement, but have a missing ADR measurement for any satellite are marked with a black star.

in the carrier-smoothed pseudoranges. We know a cycle slip occurs because of the abrupt change in range measurements. We see large cycle slips in red just after 22:00 LT. Notice that we do not have any cycle slips on the raw pseudorange measurements in light blue, since these are derived from the PRN codes. As shown in the previous section, scintillation happens within hours after local sunset, which is around 19:00 - 2:00 LT. The majority of the visible cycle slips happen in this time range, showing that scintillation is a major culprit. Also during this time frame, fluctuations in the ADR measurements are more abundant as opposed to the smoother curves that happen later in the day. These are scintillation induced phase fluctuations. An additional note is that more dropped measurements occur during this time, which are marked by black stars.

The work in [32] confirmed a relationship of cycle slips to scintillation. Refer to figure 2.8 where this relationship is investigated for the 12 scintillation data segments equatorial regions of Jicamarca, Peru, and Ascension Island. This figure counts the total number of

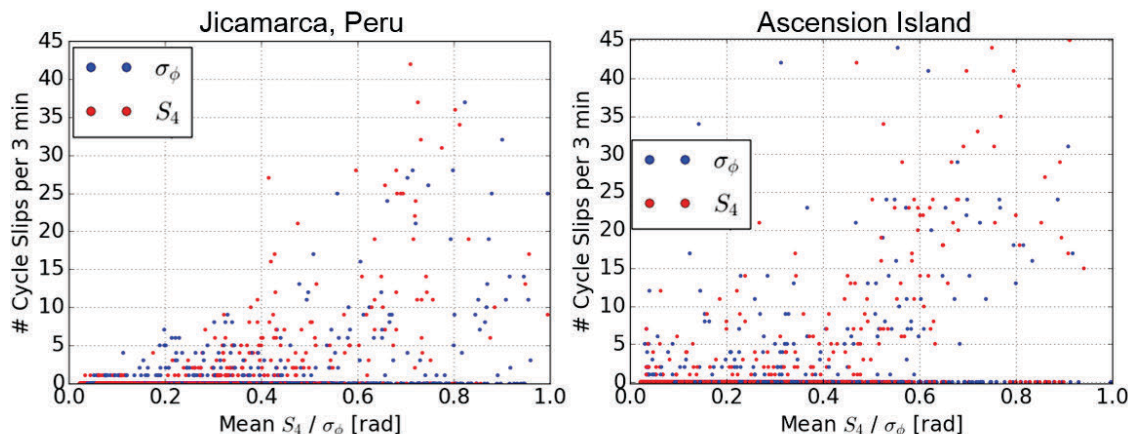


Figure 2.8: Number of cycle slips vs. S_4 and σ_ϕ in equatorial regions. Cycle slips per 3 minutes versus S_4 and σ_ϕ at Jicamarca, Peru (left) and Ascension Island (right). σ_ϕ is plotted in blue, and S_4 is plotted in red.

cycle slips that occurred on all satellites for every 3 minute data segment. This is plotted against the maximum σ_ϕ and S_4 values in the same 3 minutes after taking the mean σ_ϕ and S_4 for each satellite. Figure 2.9 shows this relationship for 6 additional high latitude data segments from Poker Flat, Alaska. The data used in these plots is the same data shown in

the results of chapter 4. In the data sets from the equatorial regions, the number of cycle slips generally increases with higher values of σ_ϕ . With the established relationship of S_4 and σ_ϕ at equatorial locations, the same general trend is seen in S_4 . This trend is not as

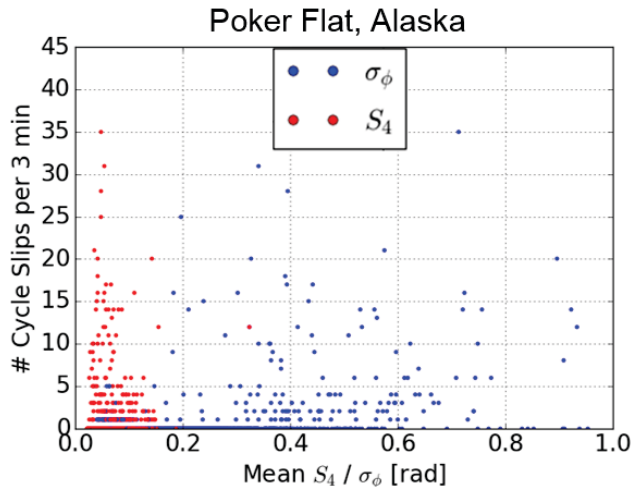


Figure 2.9: Number of cycle slips vs. S_4 and σ_ϕ in high latitude. Cycle slips per 3 minutes versus S_4 and σ_ϕ at Poker Flat, Alaska. σ_ϕ is plotted in blue, and S_4 is plotted in red.

visible in the Alaska data sets where we still see cycle slips happening at lower σ_ϕ values. All of the cycle slips in the Alaska data sets occur at very low S_4 values, since there is minimal amplitude scintillation near the poles. This is due to different scintillation physics mechanisms at the two locations. In the high latitude locations, there is a much thinner, more turbulent ionosphere. At equatorial regions, the ionosphere is much thicker, resulting in more amplitude scintillation than at high latitudes.

This data was also used to produce figure 2.10, where each 3 minute segment for each σ_ϕ bin was normalized to find the average number of cycle slips that occurred in each bin at each location. The averaging was performed only over the 3 minute segments that had at least 1 cycle slip. For the two equatorial regions, there are more cycle slips at increased values of σ_ϕ . We also see more cycle slips happening in the Ascension Island data than at Peru. In the Alaska data, we see slightly fewer cycle slips, with a trend that is not quite as clear as the equatorial regions.

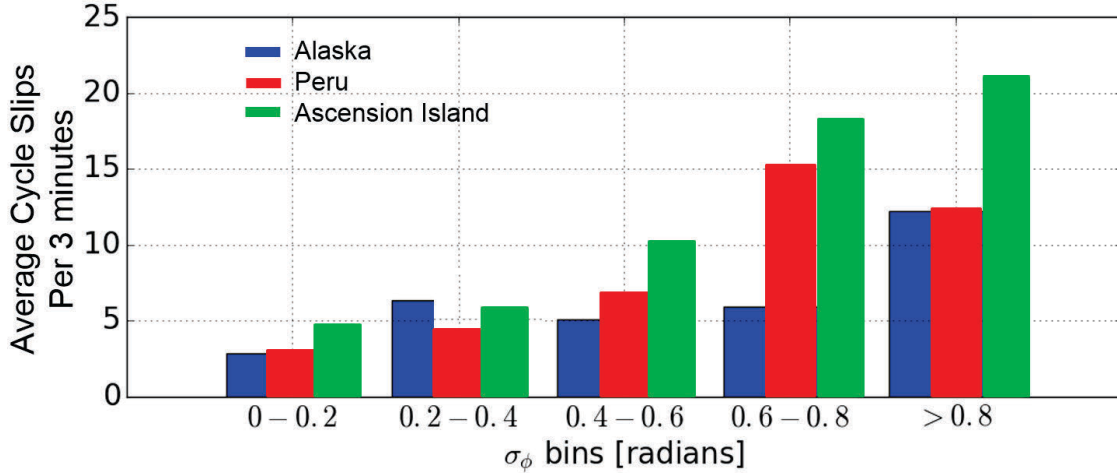


Figure 2.10: Normalized cycle slips per 3 minutes. Cycle slips per 3 minutes versus mean σ_ϕ at Poker Flat, Alaska (blue), Jicamarca, Peru (red), and Ascension Island (green).

With a GPS-only positioning algorithm, we want to see exactly how these range changes due to cycle slips cause position errors. Using the same range measurements from figure 2.7, the receiver position was calculated resulting in the position errors in figure 2.11.

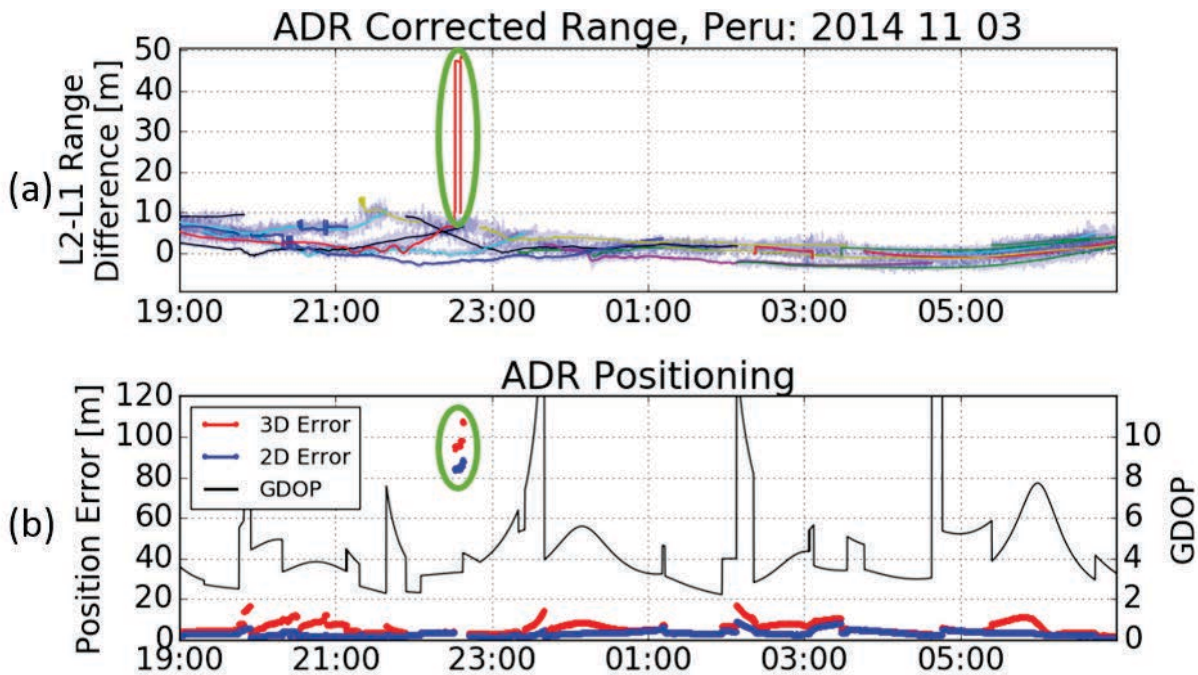


Figure 2.11: Position errors due to cycle slips. (a) L2 - L1 ADR range difference. (b) 2D (blue) and 3D (red) position error in Jicamarca, Peru on 11/3/2014. The GDOP is shown in black. The green oval indicates a large cycle slip and the corresponding position errors.

The large cycle slip highlighted in subplot (a) directly corresponds with the position errors of over 80 meters. A magnified version of this plot is provided in figure 2.12 to show the impact of the smaller cycle slips. Here, it is clear that the position errors mirror the range changes from the cycle slips. If cycle slips are left unaccounted for, errors will always appear in the position solution. Chapter 3 will discuss methods to detect and repair cycle slips.

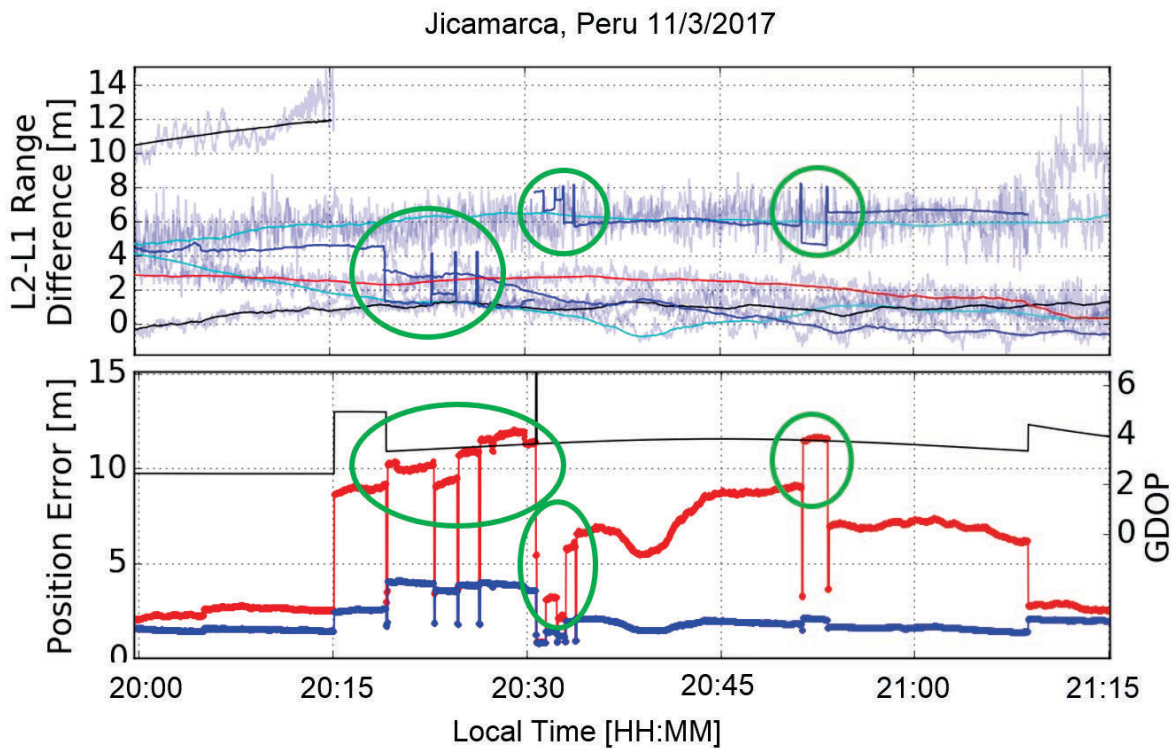


Figure 2.12: Position errors due to small cycle slips. Top: L2 - L1 ADR range difference with different colors for different satellites. Unsmoothed pseudoranges are shown in the background in light blue. Bottom: 2D and 3D position errors in Jicamarca, Peru on 11/3/2014. The GDOP is shown in black. The green ovals indicate small cycle slips and the corresponding position errors.

2.3.2 Dropped Measurements

In addition to cycle slips, dropped measurements or outages are another problem that must be anticipated in the presence of scintillation. If the receiver loses lock of the satellite due to large phase changes or deep fading in the signal power, measurements will not be

produced. Figure 2.13 shows the visibility of each satellite for a time duration of about 5 hours at Ascension Island to give an example of how scintillation causes data outages. Dropped ADR measurements for each GPS frequency are plotted on each colored satellite visibility line. Note that only two satellites that transmit L5 are present in this data set. The bottom subplot displays the σ_ϕ values for each of the visible satellites in the top subplot.

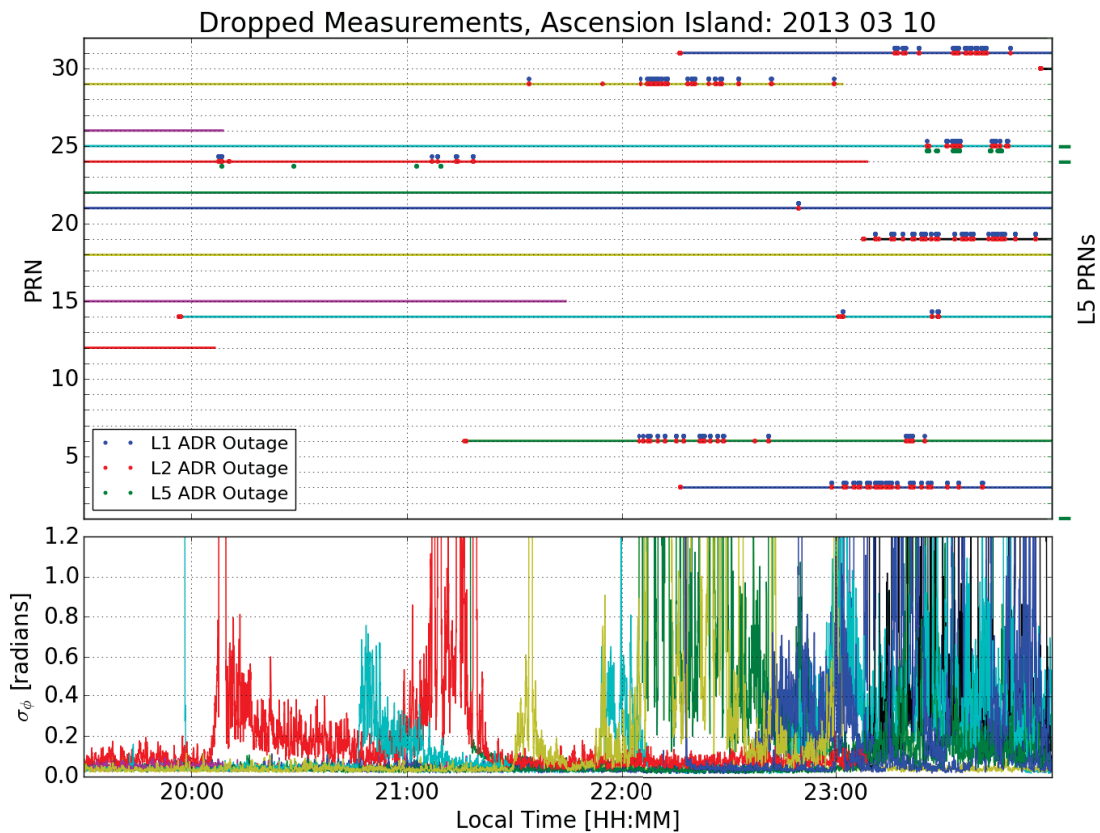


Figure 2.13: Ascension Island dropped measurements. Dropped ADR measurements for L1 (blue), L2 (red), and L5 (green) at Ascension Island on 3/10/2013. Bottom subplot: σ_ϕ values for each satellite. Different colors are used for each satellite, and the colors correspond with the top subplot.

This figure gives an idea of the level of phase scintillation that causes measurements to be dropped. Just after 21:00 LT, PRN 24 (plotted in red) has dropped measurements on all three frequencies due to strong σ_ϕ values that reach over 1 radian. PRNs 6 and 29 (in

green and yellow) have longer stretches of outages as a result of the lasting phase scintillation between 22:00 and 23:00 LT. Similarly, several satellites see outages after 23:00 LT because of the high σ_ϕ values. For this particular time range, at least one satellite experienced an outage 4.10% of the time. To verify these findings, the study in [24] used a data set from Brazil to find that there was at least one satellite missing data 4.69% of the time during a period of strong scintillation.

To establish more of a statistical relationship, the dropped measurements in the Ascension Island data set were grouped into bins of σ_ϕ , and the percentage of the total number of dropped measurements on each frequency was plotted in the bar graph in figure 2.14. This figure shows that about 50% of the dropped measurements happened when σ_ϕ was at a value greater than 0.8 radians. Another 20-25% of dropped measurements occurred during a σ_ϕ value between 0.6-0.8 radians, and there were no dropped measurements during a σ_ϕ value below 0.2 radians.

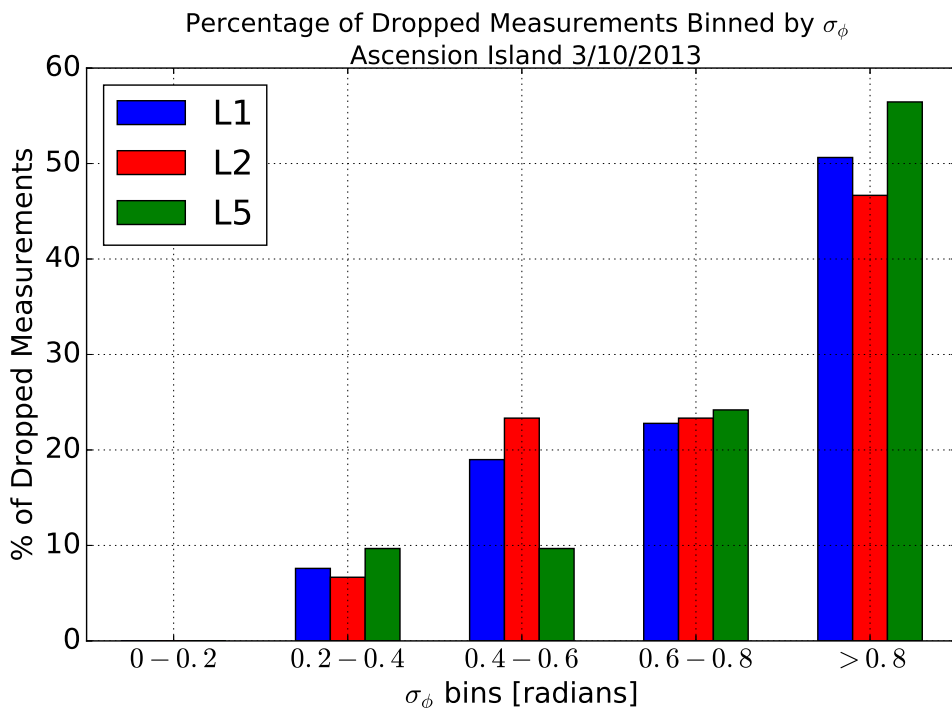


Figure 2.14: Statistics of dropped measurements. Percentage of dropped ADR measurements for L1 (blue), L2 (red), and L5 (green) binned by σ_ϕ [radians] at Ascension Island on 3/10/2013.

Dropped measurements are primarily a problem for positioning algorithms because they impair the GDOP, which is a measure of the geometry of the satellites from the receiver's perspective. In general, lower GDOP values show better geometry that improves the position calculation [4]. When a measurement is dropped from a satellite, the GDOP increases because there are fewer satellites available for a position estimate. In figure 2.15, ADR measurements are temporarily dropped on PRN 31 during strong scintillation. This is outlined with the thick black box. These dropped measurements caused an increase in GDOP, which

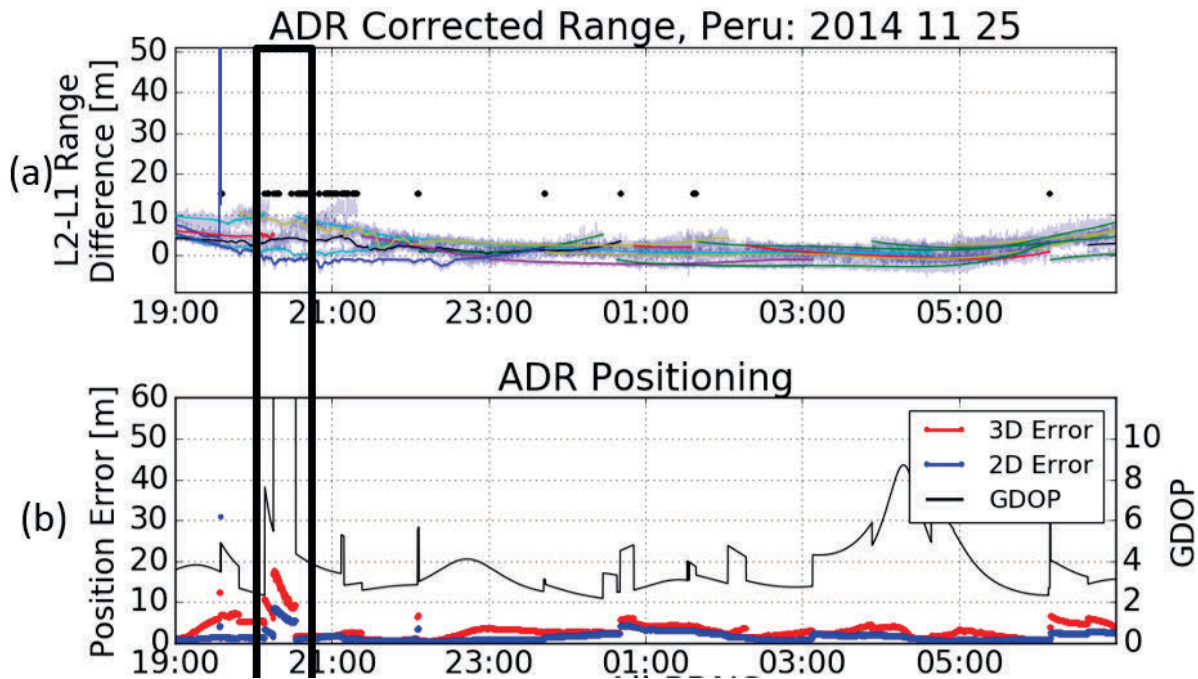


Figure 2.15: Position errors due to dropped measurements. Subplot (a): L2 - L1 ADR range difference showing dropped measurements with black points. Subplot (b): 2D (blue) and 3D (red) position error in Jicamarca, Peru on 11/3/2014. The GDOP is shown with the thin black line.

translates to position errors between 10 and 20 meters. When this satellite's measurements are reacquired, the errors diminish to less than 5 meters. If we were to include other satellite constellations, this increase in GDOP would not have been so large, and the position solution could have remained accurate.

2.3.3 Phase Error

Phase error associated with phase scintillation is also problematic for obtaining accurate range measurements. When the receiver maintains lock of the satellite through phase scintillation, the phase fluctuations translate to changes in the range measurements. The top subplot of figure 2.16 shows the carrier-smoothed pseudoranges on PRN 5 and PRN 9, and how they change with the σ_ϕ values in the bottom subplot.

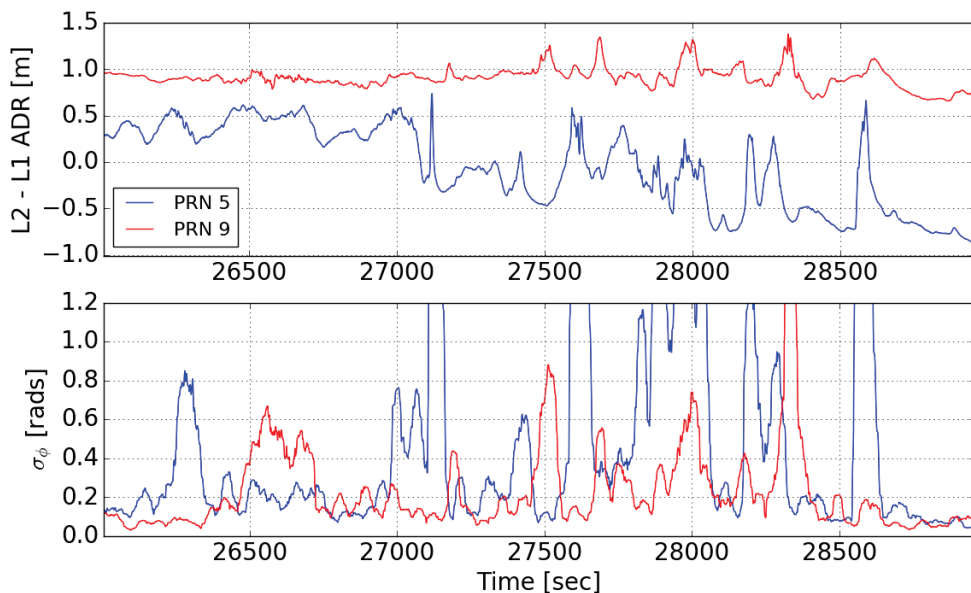


Figure 2.16: Phase fluctuations. Top: L2-L1 carrier-smoothed pseudoranges showing phase fluctuations on PRN 5 (blue) and PRN 9 (red). Bottom: L1 σ_ϕ [radians] on PRN 5 (blue) and PRN 9 (red) at Poker Flat, Alaska on 10/7/2015 from 23:13 - 00:03 LT.

PRN 5 in blue has values of σ_ϕ that exceed 0.8 radians several times in this satellite pass. Spikes greater than 1 meter are seen in the range measurements during these times. PRN 9 shows smaller values of σ_ϕ that correspond with range changes of about 0.5 meters. Figure 2.17 plots the change in range measurements versus the mean σ_ϕ value in 3-minute intervals for all satellites throughout the entire day. Generally, smaller values of σ_ϕ have less of an impact in the range measurements, as most of them stay below 0.5 meters. It is more common to see range changes greater than 0.5 meters with higher values of σ_ϕ , and the

maximum range within 3 minutes reaches a value greater than 2 meters only once. These changes in the range measurements introduce an error source that cannot be easily predicted or corrected. Although this range error is not near the same magnitude as a large cycle slip, it still takes away from the precision that is expected from the carrier phase measurements, and it is much harder to detect.

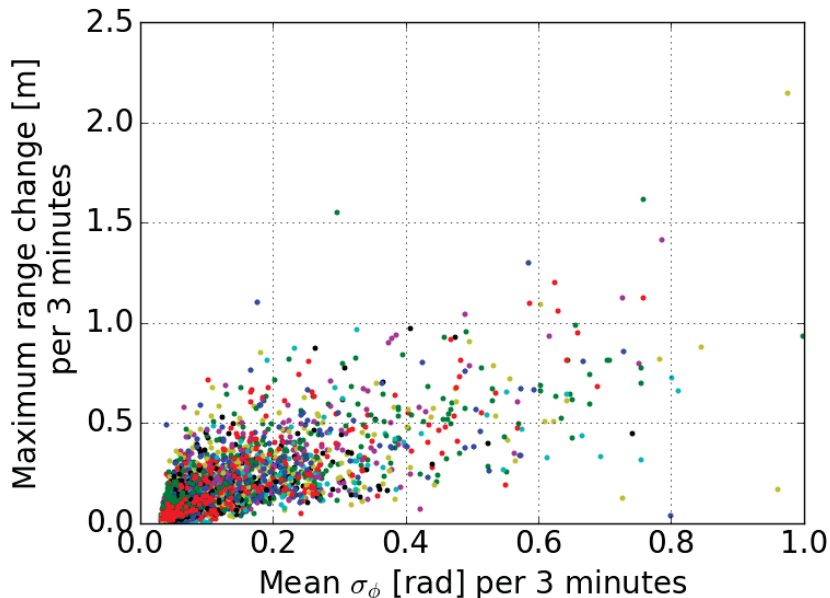


Figure 2.17: Range changes due to σ_ϕ . Change in range [meters] versus mean σ_ϕ [radians] per 3 minutes. Different colors represent different satellites. Data taken from Poker Flat, Alaska on 10/7/2015.

These scintillation induced phase fluctuations can cause an increase in error and add more variation to the position solutions as demonstrated in figure 2.18. In this figure, we can tell from the first subplot that many of the satellites are affected by phase scintillation in the first half of this time frame. The scintillation effects diminish on the majority of satellites around 22:50 LT. The 3D position error in the first half contains a couple sporadic jumps of about 2 meters because of the changes in the corresponding range measurements. Also, the 3D error is reduced from about 7 meters to less than 3 meters during this time of scintillation while the GDOP stays fairly consistent. This possibly shows how larger ionospheric structures can cause larger, gradual changes in the range measurements as well as smaller fluctuations. In

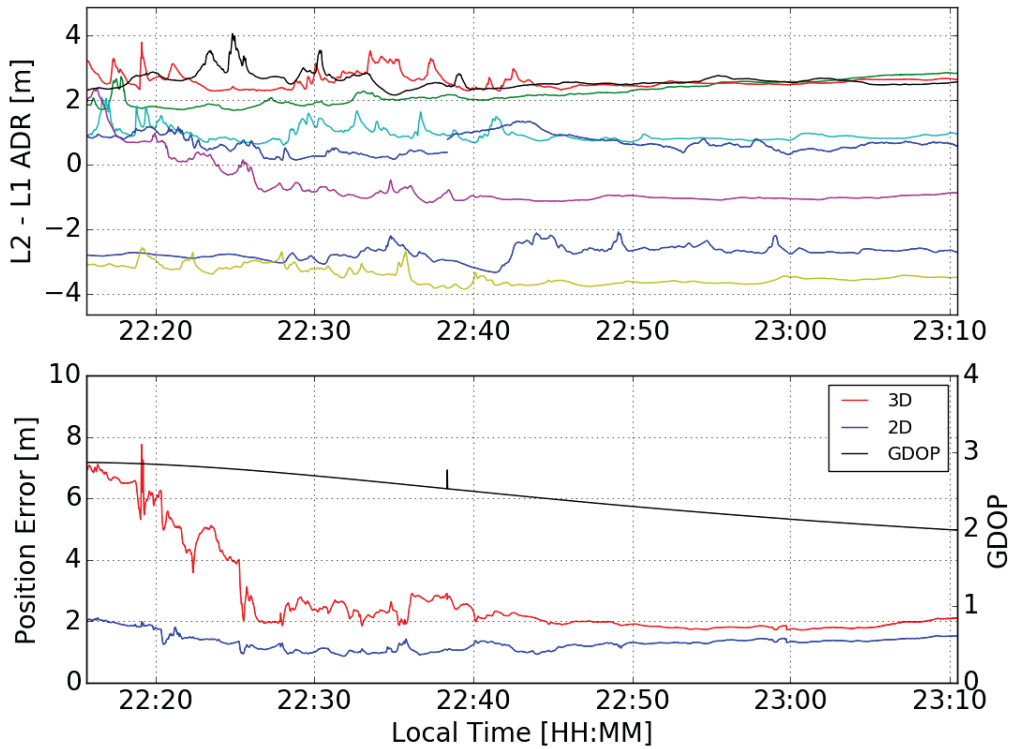


Figure 2.18: Position errors due to phase error. Top: L2 - L1 ADR range difference. Each satellite is plotted with a different color. Bottom: 2D (blue) and 3D (red) position error in Poker Flat, Alaska on 10/7/2015. The GDOP is shown in black.

the second half of the time frame, we see more consistent calculated positions that are not impacted by phase scintillation. In order to avoid the types of positioning errors presented in this chapter, algorithms must be applied to maintain the accuracy that is expected and required of GPS.

2.3.4 Septentrio Position Errors

It is worth noting that the Septentrio PolaRxS receivers perform their own proprietary positioning calculation that uses multiple satellite constellations. This section quickly shows that these receivers also experience errors during scintillation. 2D and 3D positioning errors are shown in figure 2.19, along with the mean S_4 and σ_ϕ values over all visible satellites.

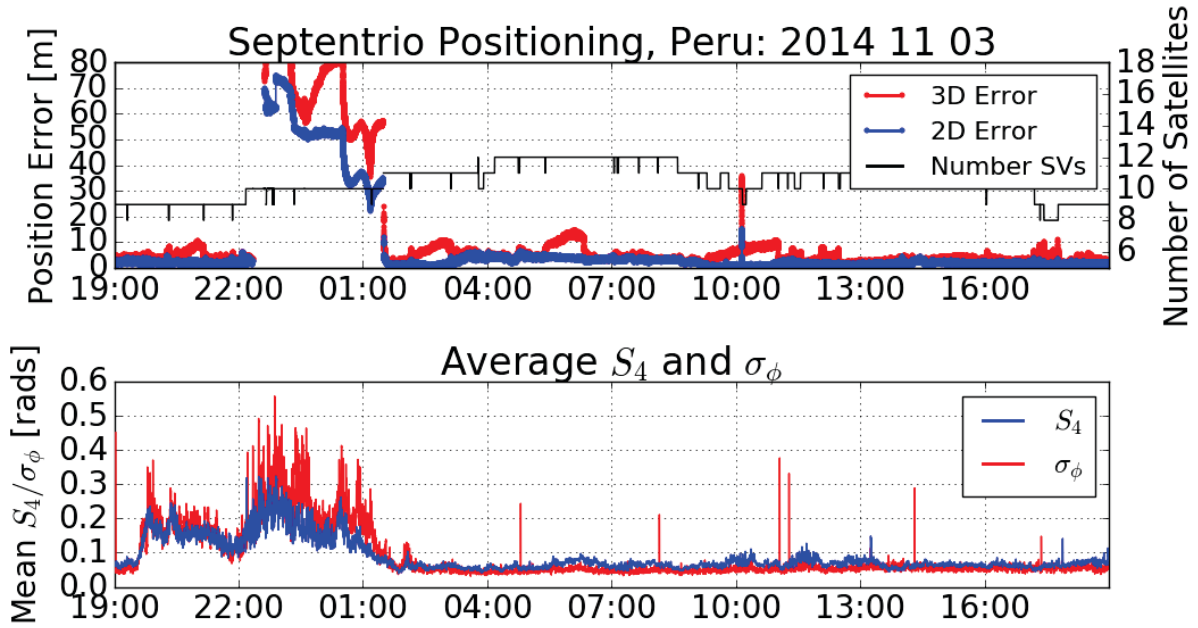


Figure 2.19: Septentrio receiver position error. Subplot 1: Septentrio PolaRxS 2D (blue) and 3D (red) position error in Jicamarca, Peru on 11/3/2014. The number of satellites used in the position solution is shown in black. Subplot 2: mean S_4 (blue) and σ_ϕ (red) values over all visible satellites.

As a result of the scintillation between 22:00 and 1:00 LT, the Septentrio’s position solution showed 3D errors upwards of 80 meters. It is difficult to pinpoint the cause of this large error during scintillation because we do not have all of the information from the Septentrio receiver such as the satellites that were used/omitted, which types of signals were used, and exactly how range corrections were applied. The receiver may have been using range measurements from a satellite (or satellites) that experienced scintillation induced cycle slips. While it is a safe assumption that fairly standard positioning techniques are used, the details of the commercial receiver’s algorithms are in-disclosed proprietary information. A direct comparison to the Septentrio calculations will not be provided in this thesis for a couple reasons. First, we are mostly interested in a GPS only position solution since this is directed towards the aviation industry. Second, there are too many differences and unknown sources of error between the Septentrio multi-GNSS position solution and a custom GPS

only position solution to be able to provide a fair comparison. For these reasons, custom GPS-only positioning algorithms will be analyzed in following chapters. In order to avoid the types of positioning errors presented in this chapter, algorithms must be applied to maintain the accuracy that is expected and required of GPS.

CHAPTER 3

METHODOLOGY

This chapter will present some of the approaches that we can use to mitigate the three scintillation induced problems discussed in the previous chapter. For a scintillating satellite signal, these approaches include substituting the unsmoothed pseudorange for the carrier-smoothed pseudorange, weighting a satellite's measurements in the navigation processing, or completely removing the satellite from the navigation processing. Examples of how these approaches impact the position solution will be shown. In addition, we will present the adaptive positioning algorithms that use these approaches. Figure 3.1 highlights the approaches and algorithms that will be discussed in this chapter with the green colored blocks.

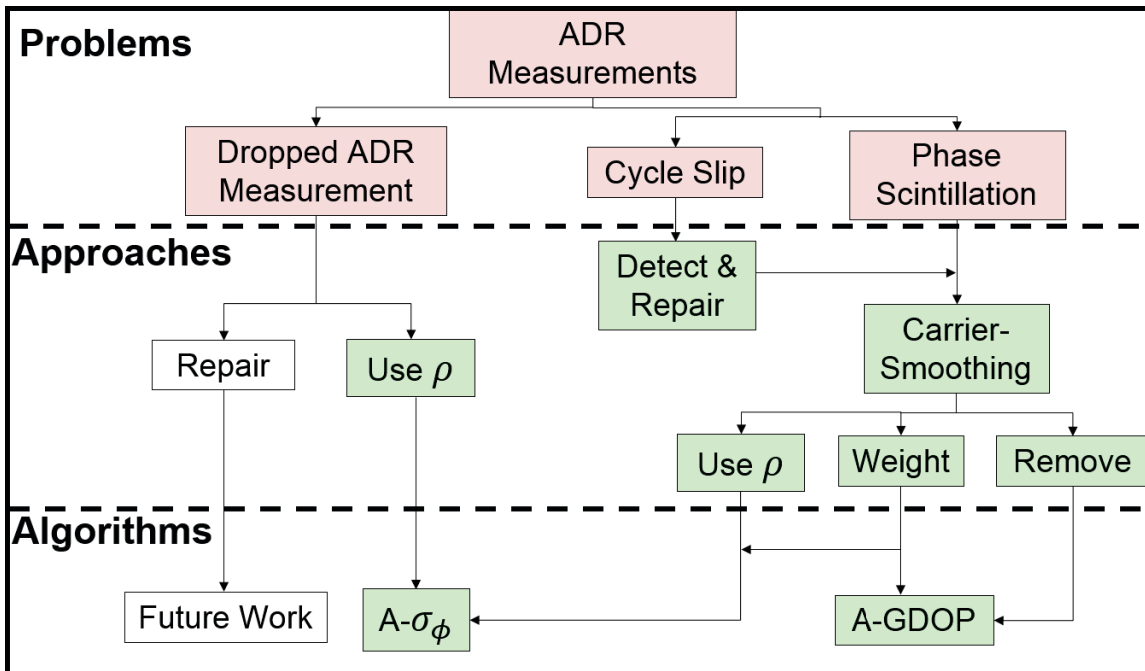


Figure 3.1: Overview of methods to mitigate ADR measurement problems. The blocks in green are covered in this chapter. Blocks in red have previously been discussed.

3.1 Cycle Slip Detection

We will begin this chapter by looking at approaches to mitigating cycle slips. Any application that uses the carrier phase/ADR measurements must take into account problematic cycle slips and how to identify them. Cycle slip detection can be performed with many different methods. Some of the most popular include calculating higher order differences of the ADR [33], looking at the difference in TEC measurements [32], and finding discrepancies in polynomial fits of the ADR [18]. In this study, cycle slips are always detected using a simple difference of two frequencies from epoch to epoch, which is similar to the TEC method presented in [32]. Advantages of this method include the ability to simultaneously detect cycle slips on both the L1 and L2 ADR while operating in real time.

This algorithm begins with the subtraction of the L1 ADR from the L2 ADR at the time of the current measurement t . Then, the ADR difference at the time of the previous measurement $t - \delta t$ is subtracted from the current value to find the quantity Δadr defined in equation 3.1. 1 Hz data is used in this study, so the time between measurements δt is 1 second.

$$\Delta adr = (adr_{L2} - adr_{L1})_t - (adr_{L2} - adr_{L1})_{t-1} \quad (3.1)$$

From here, a threshold V_T can be chosen such that exceeding the threshold indicates a positive detection of a cycle slip shown in equation 3.2.

$$|\Delta adr| > V_T \rightarrow \text{cycle slip detected} \quad (3.2)$$

A threshold V_T of 0.5 meters was used in all algorithms in this thesis. This threshold was based on a similar threshold used in [32]. In the visual of this simple method in figure 3.2, each point above the threshold line indicates a cycle slip.

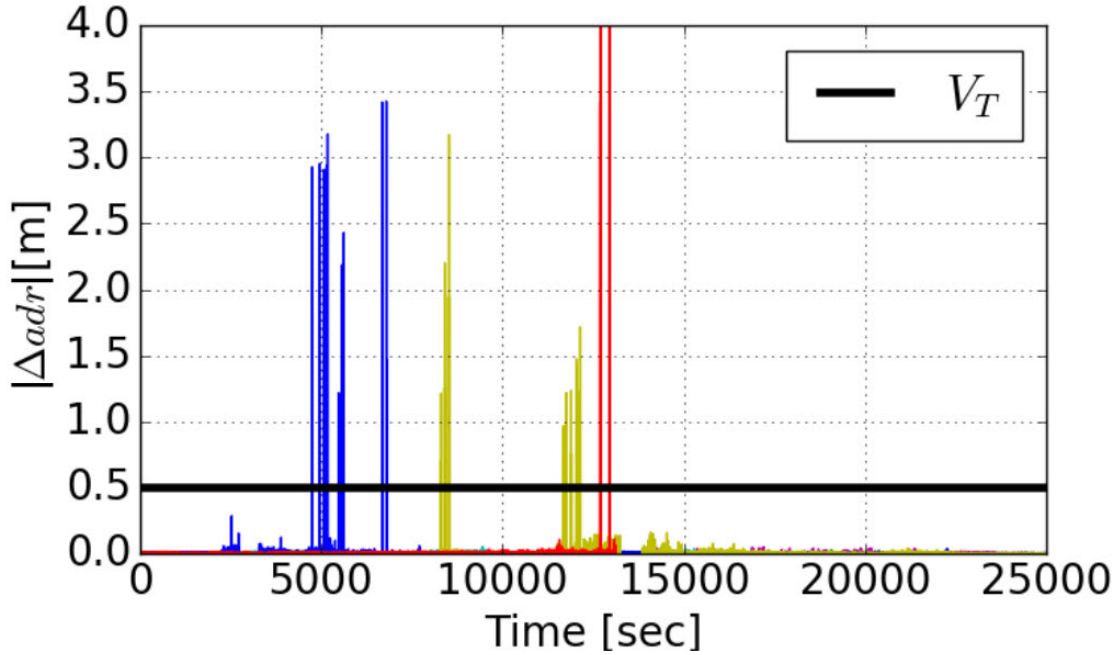


Figure 3.2: Cycle slip detection. Jicamarca, Peru - 11/3/2014 cycle slip detection method with a threshold of 0.5 meters. $|\Delta adr|$ was plotted with a different color for every visible satellite.

3.2 Cycle Slip Repair

Once cycle slips have been detected, we want to repair them to prevent sudden changes on the ADR measurements that will be used in positioning. One of the main challenges of repairing cycle slips is that most methods are heuristic, without much validation. The algorithms that have some mathematical justification often use advanced filtering techniques that are performed in post processing rather than real time. In this study, a technique is used that was derived from discussions in [25]. This cycle slip repair comes in four simple steps:

1. Detect the cycle slip
2. Determine the frequency that the cycle slip occurred on
3. Calculate the approximate number of integer cycles that the measurements jumped
4. Adjust the appropriate frequency's measurements by the approximation found in step

(3)

Cycle slip detection is performed with equation 3.2 from the previous section. Since this cycle slip detection method uses a difference of two frequencies, we need to be able to determine if the cycle slip happened on the L1 or L2 ADR measurements. Refer to figure 3.3, which shows a satellite's orbit and three different distance measurements d_1 through d_3 at three consecutive epochs. This method of repairing cycle slips requires the measurement at the current time t , and measurements at the two previous epochs $t - \delta t$, and $t - 2\delta t$. For

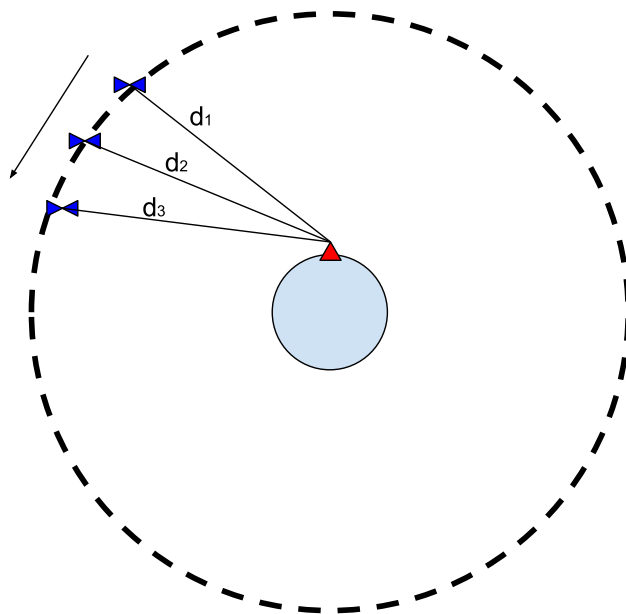


Figure 3.3: Satellite measurements for cycle slip repair. A satellite (blue triangles) approaching the horizon with three distance measurements d_1 , d_2 , and d_3 at times t_1 , t_2 , and t_3 . The red triangle represents the receiver's arbitrary location on Earth.

the moment, assume no cycle slips occurred. If this is the case, then the three consecutive distance measurements will have the relationship in equation 3.3 at all times during a satellite pass where V_T is the same threshold of 0.5 meters used in cycle slip detection.

$$|(d_3 - d_2) - (d_2 - d_1)| < V_T \quad (3.3)$$

This equation holds as long as the measurements are at a fairly high rate ($\geq 1\text{Hz}$), otherwise this assumption is not always true. Now, imagine a cycle slip occurred in between measurements 2 and 3. In this case, equation 3.3 is not true.

$$|(d_3 - d_2) - (d_2 - d_1)| > V_T \quad (3.4)$$

We can perform this calculation individually on each frequency to isolate which one jumped. To satisfy step (3) of cycle slip repair, the difference on the left side of the inequality is used to approximate the magnitude of the cycle slip d_{cs} as in equation 3.5.

$$d_{cs} \approx (d_3 - d_2) - (d_2 - d_1) \quad (3.5)$$

Then, this approximation d_{cs} is added to the measurements following the cycle slip to derive a new ADR measurement that is corrected for the cycle slip. This process is shown in figures 3.4 and 3.5.

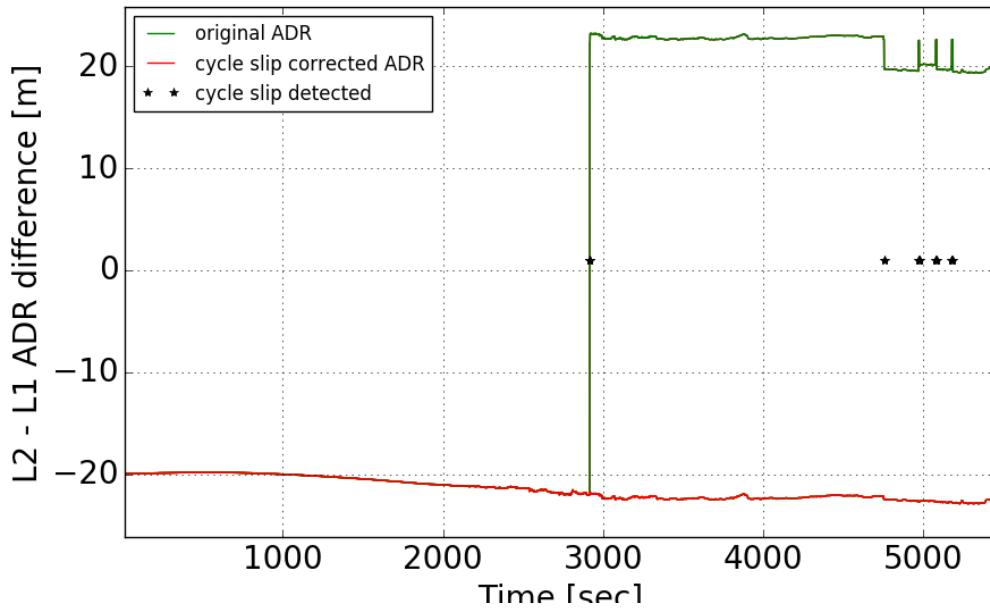


Figure 3.4: Cycle slip repair 1. Cycle slip-free ADR measurements (red) after repairing the original ADR measurements (green). Black stars show where a cycle slip was detected. Data was taken in Jicamarca, Peru on 11/3/2014 from 19:00-20:25 LT.

In these plots, the green line represents a dual frequency combination of the original ADR measurements that clearly have cycle slips. A black star marks the points where a

cycle slip was detected, and the red line shows the new ADR measurements after performing this correction.

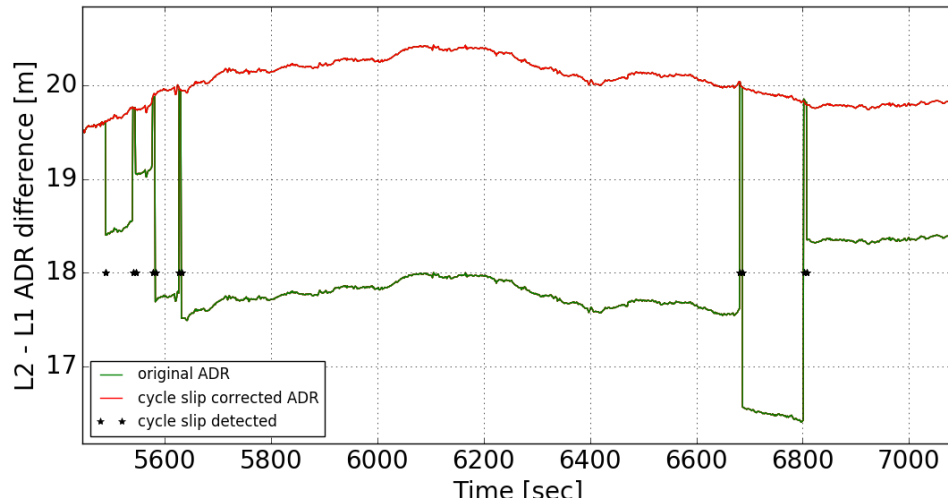


Figure 3.5: Cycle slip repair 2. Cycle slip-free ADR measurements (red) after repairing the original ADR measurements (green). Black stars show where a cycle slip was detected. Data was taken in Jicamarca, Peru on 11/3/2014 from 20:30-20:58 LT.

This algorithm successfully detects and repairs ADR measurements on multiple frequencies. It is important to note that this algorithm is most effective on stationary or slow moving receivers. On a highly dynamic platform, a more advanced technique would be required for cycle slip repair. After correcting cycle slips, other algorithms including carrier-smoothing can be performed with a reduced likelihood of malfunction.

3.3 Carrier-Smoothing Algorithms

As stated in chapter 1, users would like to have the most precision by using the low-noise carrier phase for range measurements. However, these measurements lack absolute range accuracy due to the integer ambiguity term from equation 1.3. This section discusses two methods that are commonly used to calculate carrier-smoothed pseudoranges, and proposes one new method that employs advantages from each of the two common techniques.

3.3.1 Hatch Filter for Carrier-Smoothing

The first carrier-smoothing method is the well-known Hatch filter, which was introduced in [34]. This real time technique combines the ADR and pseudorange to create a filtered version of the pseudorange on each individual frequency. For an arbitrary frequency, this will be denoted as ρ_H , and can be computed at time t through equations 3.6 and 3.7 below. The pseudorange at time t is given by ρ_t .

$$\rho_{H,t} = \frac{1}{n}\rho_t + \frac{n-1}{n}(\rho_{H,t-1} + adr_t - adr_{t-1}) \quad (3.6)$$

where

$$n = \begin{cases} t, & t < N \\ N, & t \geq N \end{cases} \quad (3.7)$$

and N is the maximum window size, and n is a variable window size. The nominally used maximum window size for this algorithm is 5 minutes (300 seconds), and it is initialized by equating the first ρ_H value to the ρ measurement at the first epoch [34] as in equation 3.8.

$$\rho_{H,1} = \rho_1 \quad (3.8)$$

Once the Hatch filter is initialized, the window n grows until it reaches the maximum value of N seconds. At this point, the window stays fixed at N seconds and the filtering continues. If a cycle slip is detected through equation 3.2 at any point during the filtering, ρ_H must be re-initialized through equation 3.8 and the window resets by setting n to 1 second. The variable window n continues to grow until reaching the maximum fixed value of N once again. If the cycle slip is repaired, ρ_H does not need to be re-initialized. However, if there is a dropped ADR measurement, we do need to re-initialize the filtering. Applying this process to the L1 and L2C signals on PRN 30 results in figure 3.6.

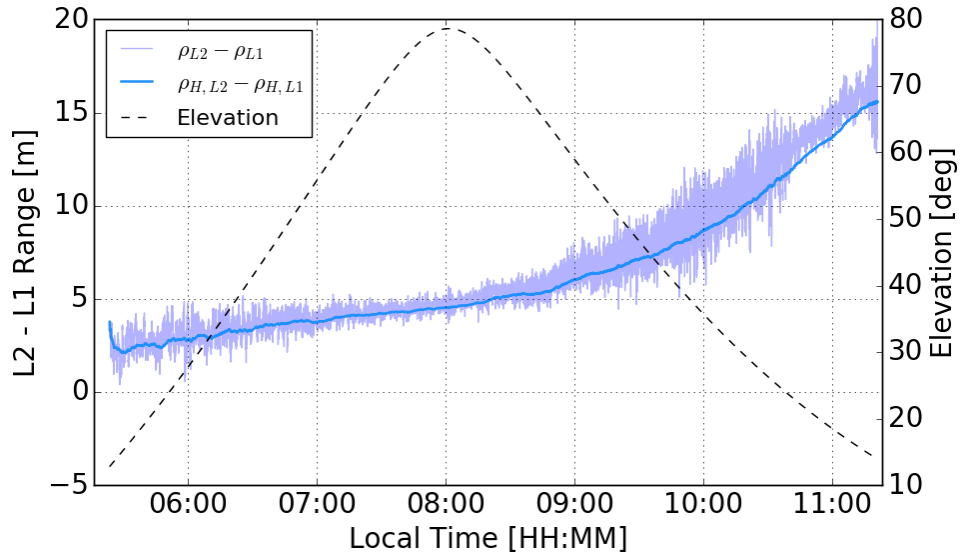


Figure 3.6: Hatch filter carrier-smoothing. A 300 s window size was used on PRN 30, 11/26/2014 at Jicamarca, Peru. Unsmoothed pseudoranges are shown in light blue, and the Hatch filter carrier-smoothed pseudoranges are shown in darker blue. The raw ADR measurements are shown in green, and the elevation angle is shown in dashed black.

Figure 3.6 shows the difference of the computed ρ_H at the L1 and L2 frequencies as the darker blue line. It is often easier to see small details of the carrier-smoothing when looking at the difference of these two frequencies. The light blue in the background displays the ρ measurements, and the green line shows the ADR measurements. Ideally, we want the dark blue line to perfectly filter out the noisier light blue line, which would indicate a reduction in noise of the ranges. This is the case at the beginning of the satellite pass, where the ρ_H calculations appear to be a smoothed version of the ρ measurements, with some small fluctuations. However, the ρ_H calculations tend to drift apart from the ρ measurements after about 9:00 LT. This is due to a delay effect known as code-carrier divergence. This is where the pseudorange and ADR measurements drift apart from each other because of the ionospheric effects on the different frequencies of each component. This could indicate a slight reduction in the accuracy of the range measurements as a result of the Hatch filtering. Other carrier-smoothing algorithms have been developed in an attempt to solve the issues with the Hatch filter, such as the one in the next subsection.

3.3.2 Code-Noise Multipath Bias Estimation for Carrier-Smoothing

Unlike the Hatch filter from the previous section, the Code Noise and Multipath (CNMP) carrier-smoothing algorithm is based on a direct estimation of the range bias between the pseudorange and the ADR [35]. The comparison of these measurements can be computed through the code-minus-carrier (*CMC*) observable. Due to the somewhat large noise and multipath impact on the pseudorange, we want to substitute these quantities for the negligible noise and multipath on the ADR measurements [5]. In order to accomplish this, the bias on the ADR must be estimated after the removal of ionosphere effects. Neglecting the satellite and receiver hardware biases in the measurement models from chapter 1, the CNMP algorithm is described here for the L1 frequency. Define the constant α , which will be used to perform a dual-frequency ionosphere correction using the L1 and L2 frequencies.

$$\alpha = \frac{2f_{L2}^2}{f_{L2}^2 - f_{L1}^2} \quad (3.9)$$

Since the multipath and unmodelled errors on the ADR from equation 1.2 are small enough to be neglected, the *CMC* observable is simplified to

$$\begin{aligned} cmc_{L1} &= \rho_{L1} - adr_{L1} \\ &= 2I_{L1} + M_{\rho,L1} - \lambda_{L1}N_{L1} + \epsilon_{\rho,L1} \end{aligned} \quad (3.10)$$

This *CMC* observable contains twice the amount of ionospheric error. We account for this by calculating an ionosphere corrected *CMC* observable by using the coefficient α and the dual frequency ADR measurements in equation 3.11.

$$\begin{aligned} cmc_{L1,corr} &= cmc_{L1} - \alpha(adr_{L1} - adr_{L2}) \\ &= M_{\rho,L1} - \lambda_{L1}N_{L1} + \epsilon_{\rho,L1} - \alpha(\lambda_{L1}N_{L1} - \lambda_{L2}N_{L2}) \\ &= M_{\rho,L1} + \epsilon_{\rho,L1} + B_{L1} \end{aligned} \quad (3.11)$$

where the constant bias is defined by:

$$B_{L1} = -\lambda_{L1}N_{L1} - \alpha(\lambda_{L1}N_{L1} - \lambda_{L2}N_{L2}) \quad (3.12)$$

The goal is to determine the best estimate for the bias B_{L1} . The best approach to this is to apply a simple windowed average on CMC_{corr} to filter out high frequency noise and multipath components [35,36]. The window size used is 1000 seconds based on previous studies. Next, error bounds on the filtered CMC_{corr} are calculated using the maximum and minimum value in each 1000 s window. The smallest error bound corresponds with the segment of data with the smallest multipath contribution, which typically occurs near the satellite's highest elevation [37]. The value of B_{L1} is obtained from the filtered CMC at the time index of the smallest error bound. The CNMP corrected pseudorange $\rho_{B,L1}$ is then calculated using this bias estimate in equation 3.13.

$$\rho_{B,L1} = \rho_{L1} - CMC_{L1} + B_{L1} \quad (3.13)$$

Equation 3.13 simplifies to the L1 ADR adjusted by this constant bias [37].

$$\rho_{B,L1} = adr_{L1} + B_{L1} \quad (3.14)$$

Figure 3.7 shows the error bounds around the filtered CMC for a satellite pass. Between 5:15 and 5:30 UTC, the error bounds are the smallest, so the bias estimate is formed at this point. The bottom subplot shows the L2 - L1 raw pseudorange difference in blue, and the CNMP corrected pseudoranges in red after applying this bias estimate to the ADR. This algorithm uses a windowed approach to estimate the bias, so cycle slips are a large problem for this particular algorithm. One option is to repair cycle slips before applying this algorithm. A more common approach is to simply discard the data that is affected by cycle slips.

Typically, this algorithm is applied in post processing in order to find the best estimate for the bias during an entire satellite pass. In real time, this algorithm works by waiting until enough data has passed to form a bias estimate with a window of 1000 seconds. The error bounds are continuously calculated with the incoming measurements, and the bias estimate is updated if we find a point with smaller error bounds. Using the same satellite pass from figure 3.6, the real time CNMP method is plotted in figure 3.8.

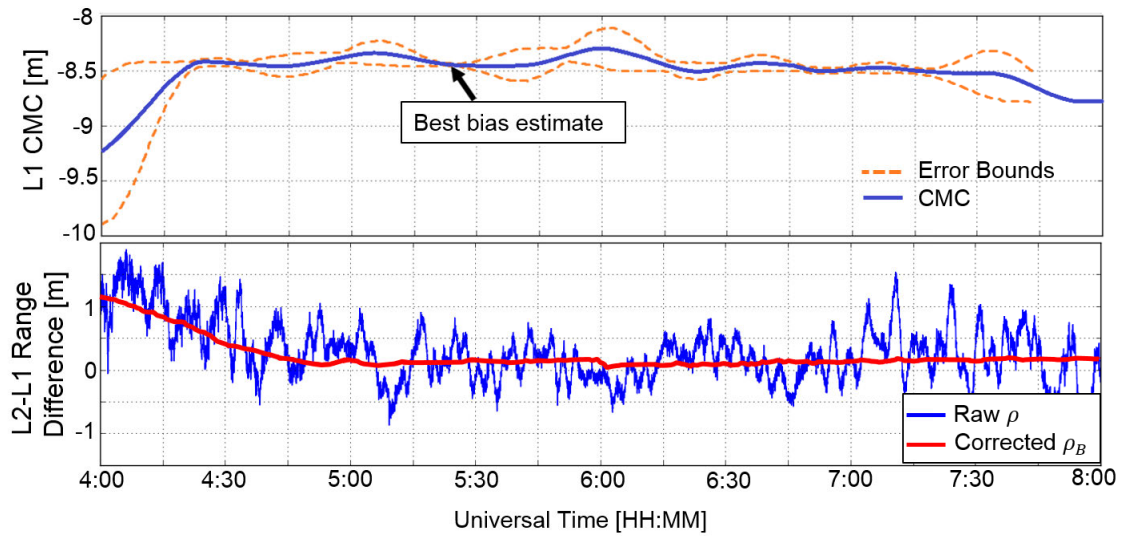


Figure 3.7: CNMP error bounds. Top: Filtered *CMC* (blue) and error bounds (dashed orange). Bottom: L2 - L1 pseudorange (blue) and CNMP corrected pseudorange after bias estimation (red)

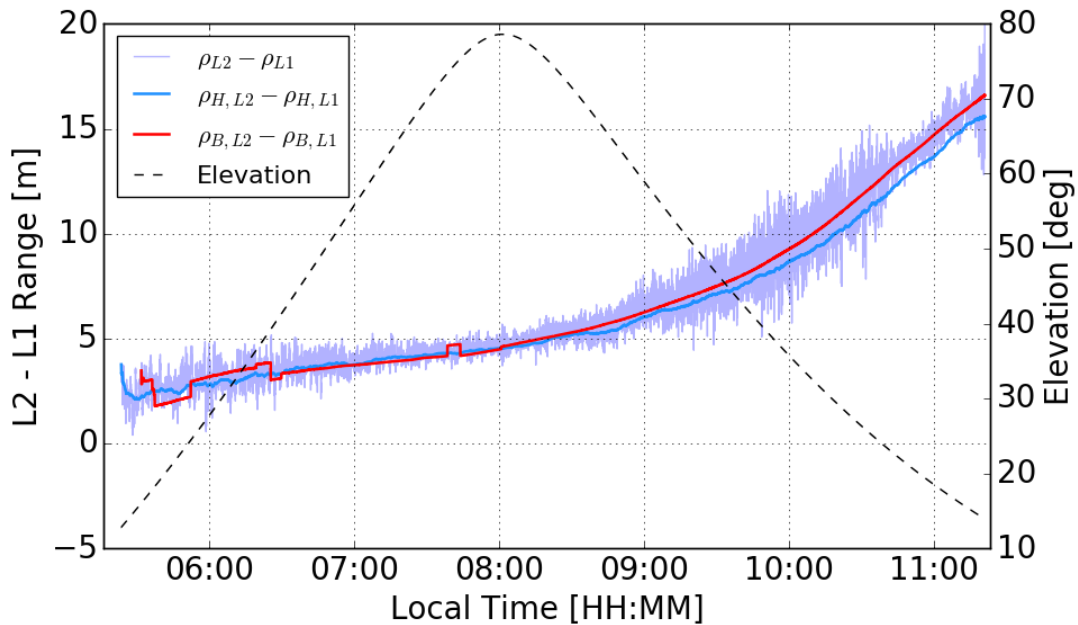


Figure 3.8: CNMP bias estimation. CNMP carrier-smoothing (red) with a 1000 second window size on PRN 30, 11/26/2014 at Jicamarca, Peru. This is overlaid on the unsmoothed pseudorange (light blue), and the Hatch filter carrier-smoothing (dark blue). The elevation angle is shown with the dashed black line.

The real time application of the CNMP method has several helpful and harmful features. First, a bias estimate could not be formed until 1000 seconds into this satellite pass because of the fixed windowed approach typically used with this algorithm. After accumulating 1000 seconds of data, a fairly poor bias estimate was formed. Throughout the first half of the satellite pass, the bias estimate is adjusted when a smaller error bound is calculated. Each vertical jump represents a new bias estimate. The best overall bias estimate happens near the peak elevation of the satellite pass, and this estimate is not adjusted for the rest of the satellite pass. Despite these issues, this method produces more accurate carrier-smoothing overall during the last half of the satellite pass than the Hatch filter. There is also less noise in these measurements because this technique directly uses the ADR measurements instead of incorporating a linear combination of the ADR and pseudorange measurements. This method has discontinuities in the first half of the satellite pass, but no delay effect towards the end of the satellite pass. The Hatch filter sees no discontinuities, but there is a delay effect. The complimentary performance of these methods helped to come up with a new technique in the following section.

3.3.3 Hybrid Hatch Filter/CNMP for Carrier-Smoothing

Due to the shortcomings of the Hatch filter and CNMP techniques, this subsection provides a new hybrid technique that uses the advantageous features of the previous algorithms. We saw the Hatch filter lost some accuracy towards the end of the satellite pass, and the real time CNMP method didn't produce consistent accuracy until the last half of the satellite pass. The goal for this new technique is to maintain carrier-smoothing accuracy as long as the satellite is visible.

This hybrid technique solves these issues by initializing carrier-smoothing with a Hatch filter. We then take advantage of the known elevation angle of the satellite. As soon as the satellite reaches its highest elevation, a window is formed and a bias estimate is made using the CNMP algorithm. A forced bias estimate at the top of a satellite pass almost always

results in better accuracy since this point typically has the smallest contributions of noise and multipath. If a cycle slip is detected using this algorithm, we can try to form another bias estimate as long as the satellite is still within 2 degrees of its peak elevation. (2 degrees was heuristically selected in this study, but different thresholds could be experimented with). Otherwise, the Hatch filter will be initialized again for the remainder of the satellite pass. The corrected measurements will be expressed as ρ_{HB} . A flowchart of this process is summarized in figure 3.9. This algorithm can be directly compared with its building blocks by

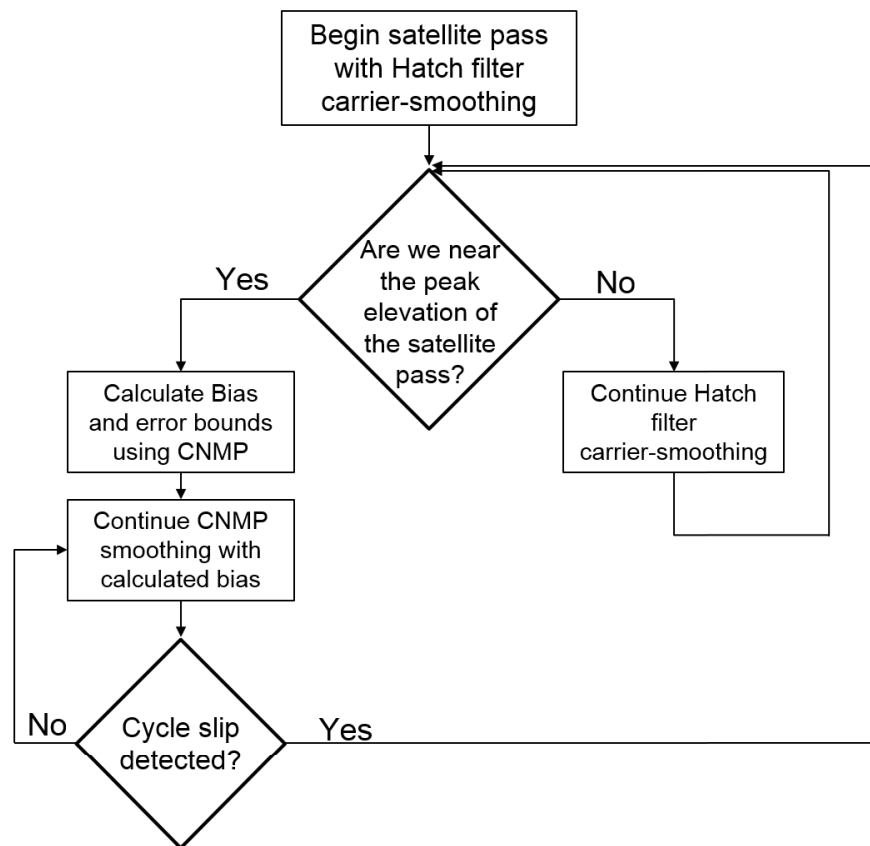


Figure 3.9: Hatch filter/CNMP hybrid flowchart.

viewing figure 3.10, which shows the result of this technique on the same satellite pass used in the previous two subsections. The hybrid carrier-smoothing in this figure in the black dashed line accurately filters the raw pseudorange measurements after combining the first two techniques. This technique resembles the Hatch filter for the first half of this satellite

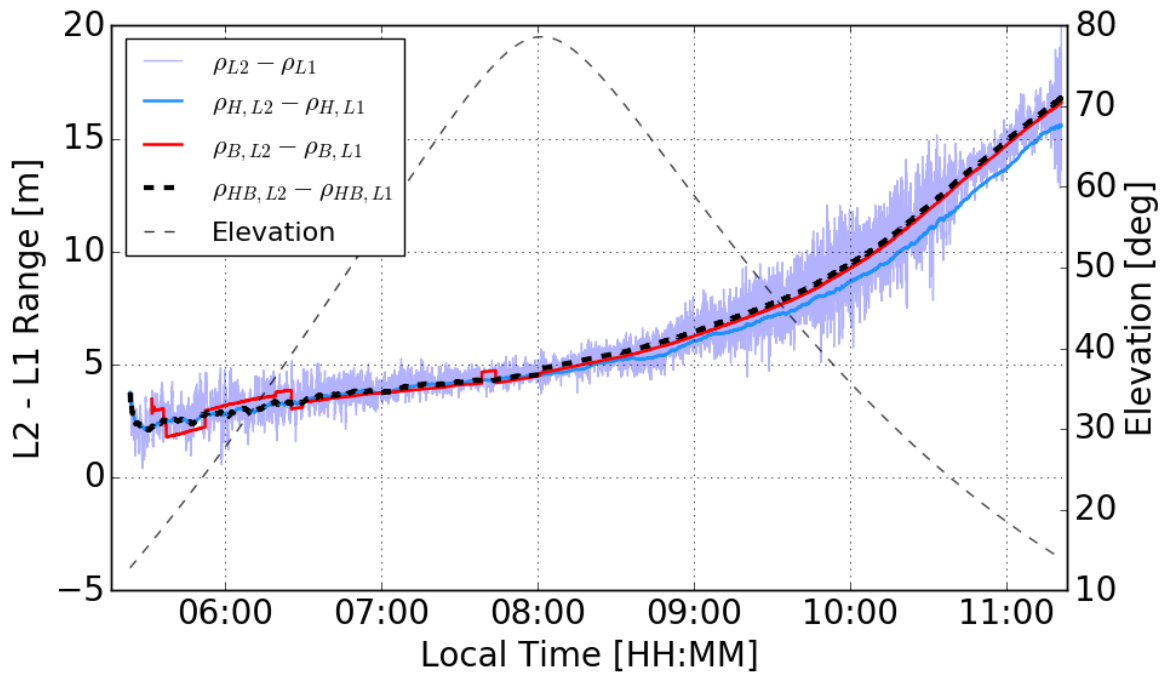


Figure 3.10: Hatch filter/CNMP hybrid carrier-smoothing. Hybrid technique (bold black dashed line) with a 300 second window size for Hatch filtering, and a 1000 second window size for CNMP bias estimation on PRN 30, 11/26/2014 at Jicamarca, Peru. Overlaid on the unsmoothed pseudorange (light blue), the Hatch filter (dark blue), and the CNMP method (red). The elevation angle is shown with the lighter dashed black line.

pass. Then, the CNMP bias estimation happens at the peak of the satellite pass (specified in the figure). When the bias estimate happens, the carrier-smoothing resembles the CNMP method, and accuracy is maintained as the satellite descends. The following chapter will compare positioning solutions that use only the hybrid carrier-smoothed pseudoranges against a positioning solution that uses only the Hatch filter carrier-smoothed pseudoranges.

One more note is that this algorithm does not always work flawlessly. If the satellite's peak elevation is not very high, sometimes a poor CNMP bias estimate occurs. As an example, figure 3.11 shows the hybrid carrier-smoothed pseudoranges in red, and the unsmoothed pseudoranges in light blue. The peak elevation angle of this satellite is only 33 degrees. When a CNMP bias estimate is forced at this peak elevation, we see a clear discontinuity at 12:15 LT. This estimated bias is fairly poor for the remainder of the satellite pass.

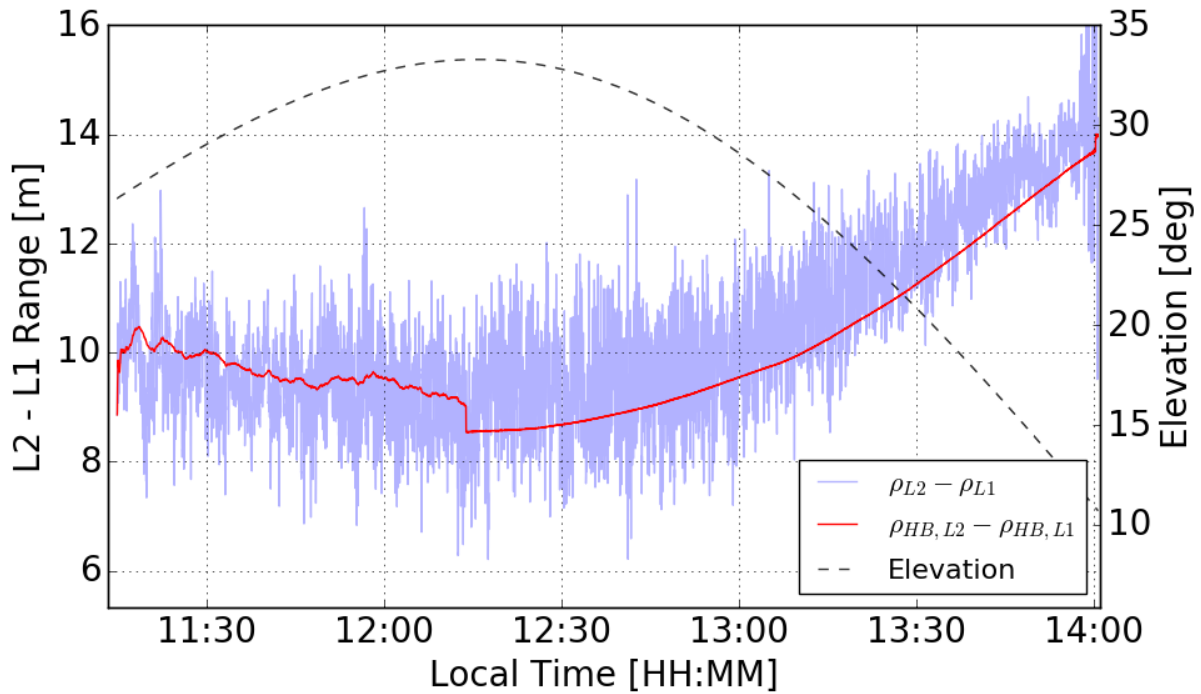


Figure 3.11: Poor bias estimate from hybrid Hatch filter/CNMP carrier-smoothing. Hybrid technique carrier-smoothing (red) with a 300 second window size for the Hatch filtering, and a 1000 second window size for the CNMP bias estimation on PRN 17, 11/26/2014 at Jicamarca, Peru. This is overlaid on the unsmoothed pseudorange (light blue), and the elevation angle is shown with the lighter dashed black line.

Although it was not implemented for the results in this thesis, this algorithm could be improved by applying an elevation mask. After going through some of the data, it was determined that these poor bias estimates typically only happen when both the elevation is below 40 degrees, and the pseudorange measurements are generally noisier than usual, which could be due to multipath effects. Therefore, we could continue to use the Hatch filter if the peak elevation of this satellite is below a 40 degree threshold, or if there is an increase in the standard deviation of the pseudorange measurements towards the peak. This would help to avoid discontinuous bias estimates. In this thesis, all carrier-smoothing was manually examined to ensure poor bias estimates from this algorithm did not impact the results.

3.4 Pseudorange Substitution During Carrier-Phase Discontinuity

This section will explore the benefits of substituting the unsmoothed pseudorange for the carrier-smoothed pseudorange during some of the problems that are associated with scintillation. Refer back to figures 2.11 and 2.15, which show the impact that cycle slips and dropped ADR measurements have on the navigation solution. This section briefly summarizes the analysis in [37], where we show that errors caused by carrier phase discontinuities can be resolved by substituting the unsmoothed pseudorange measurements. This method can be thought of as an alternative technique to repairing cycle slips, which is often a challenge, especially on highly dynamic platforms.

Several data sets that include cycle slips and dropped measurements were selected to directly compare the differences between a position solution that uses only carrier-smoothed pseudoranges (ρ_B) versus a position solution that uses only unsmoothed pseudoranges (ρ_c). A direct comparison of the 3D position errors from using these two methods is shown in figure 3.12. One thing to notice is that there is a pattern of horizontal fluctuation. This is

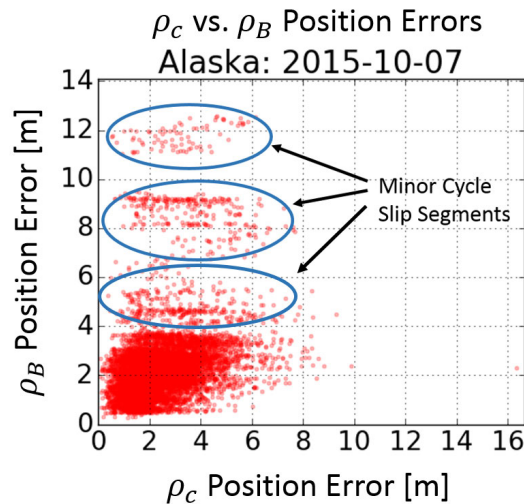


Figure 3.12: Poker Flat, Alaska ρ_c vs. ρ_B positioning. Positioning using unsmoothed pseudoranges (ρ_c) versus using carrier-smoothed pseudoranges (ρ_B).

due to the noise on the ρ_c measurements. The noise in these measurements causes the ρ_c positioning errors to fluctuate from 0-8 meters while the errors from the ρ_B stay consistently

under 4 meters. Circled in blue are ρ_B position errors ranging from about 5-13 meters from three of the data segments affected by cycle slips. (Cycle slips have not been repaired in this comparison). Using ρ_c during these cycle slips reduces the 3D error to the range of 1-8 meters at the cost of a position solution that has an increased standard deviation.

Similarly, we can plot the relationship between these two positioning methods for the problematic data segments that were previously shown on the Peru data sets in section 2.3. The large cycle slip from figure 2.11 caused 3D position errors of over 80 meters, while the ρ_c measurements were able to limit the error to less than 5 meters as seen in the left subplot of figure 3.13. The subplot on the right circles the position solutions during a smaller cycle slip, just like in the previous example.

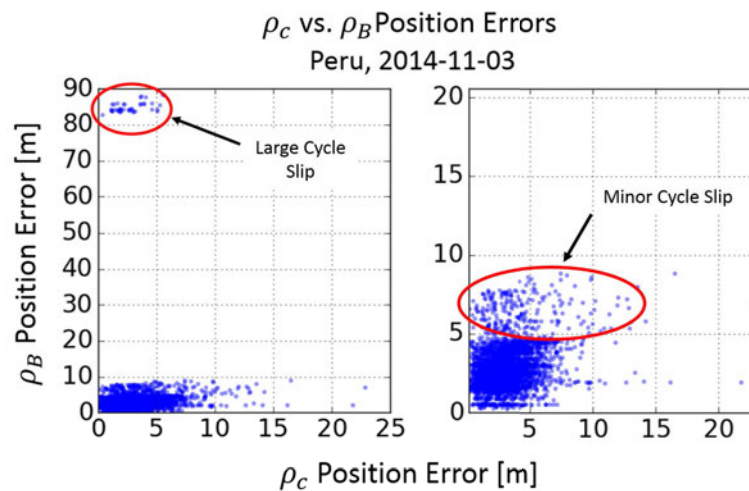


Figure 3.13: Jicamarca, Peru 11/3/2014 ρ_c vs. ρ_B positioning. Positioning errors using unsmoothed pseudoranges (ρ_c) versus using carrier-smoothed pseudoranges (ρ_B). The subplot on the right displays a zoomed in view of the left subplot.

The change in GDOP from the dropped ADR measurements in figure 2.15 is also distinctly seen when comparing the errors using the two different measurements for positioning. In addition to a large and small cycle slip, figure 3.14 circles the points where the ρ_B position solution has slightly larger errors due to the change in GDOP from the dropped ADR measurements. The ρ_c position solution has a better GDOP because the pseudorange measurements were not dropped. This results in smaller position errors for ρ_c .

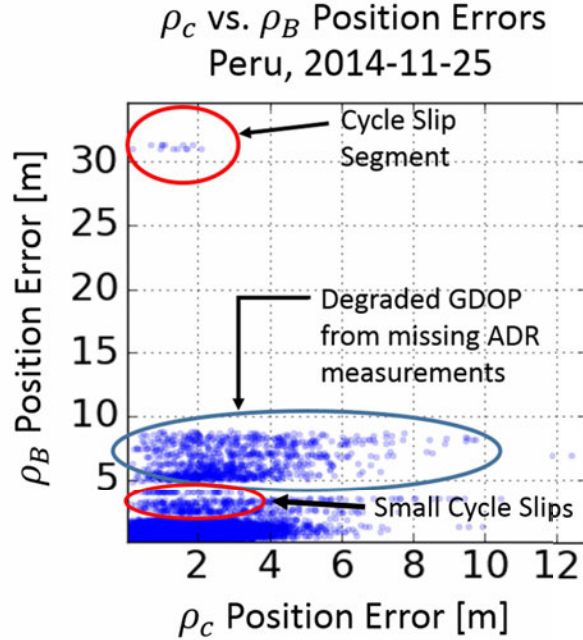


Figure 3.14: Jicamarca, Peru 11/25/2014 ρ_c vs. ρ_B positioning. Positioning errors using unsmoothed pseudoranges (ρ_c) versus using carrier-smoothed pseudoranges (ρ_B).

During these examples of carrier phase discontinuities, the reduction in positioning error from using ρ_c rather than ρ_B is summarized in table 3.1 for the three data sets. Since we are able to get over a 60% error reduction during carrier phase discontinuity by using the unsmoothed pseudorange measurements for positioning rather than the carrier-smoothed pseudoranges, this idea has been implemented into one of the adaptive algorithms that will be described later in this chapter.

Table 3.1: Error reduction during cycle slips. Reduction in mean 3D error by using ρ_c instead of ρ_B during all segments affected by carrier phase discontinuity

Data Set	Mean ρ_B Error [m]	Mean ρ_c Error [m]	Error Reduction [%]
Alaska: 10/7/2015	9.13	3.45	62.21 %
Peru: 11/3/2014	16.97	3.97	77.48 %
Peru: 11/25/2014	6.23	2.21	64.52 %

3.5 Removing Measurements Impacted by Scintillation

This section contains an example that explores the approach of removing a scintillating satellite from the navigation processing. This example uses data from Jicamarca, Peru. Figure 3.15 shows a skyplot of the visible GPS satellites and their σ_ϕ values. PRN 16 and PRN 27 are both scintillating during this time frame.

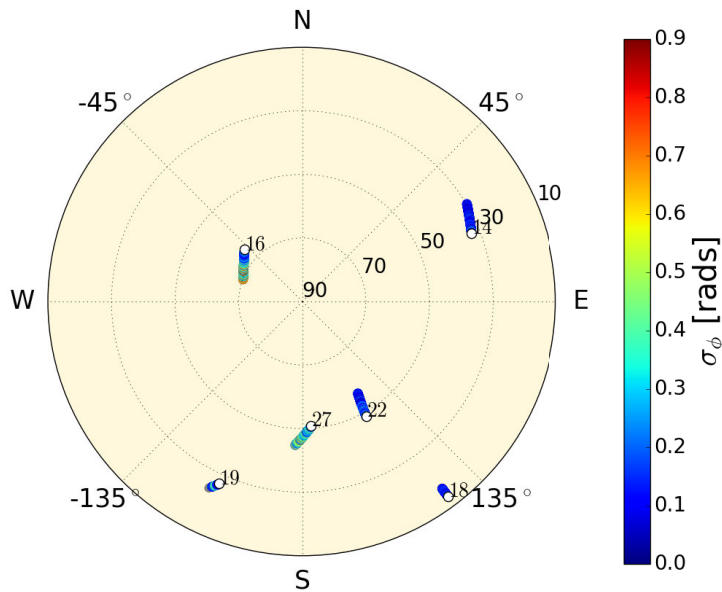


Figure 3.15: Jicamarca, Peru skyplot. Skyplot colored by the σ_ϕ values at Jicamarca, Peru at 23:18-23:35 LT on 11/3/2014. PRN 16 and PRN 27 are scintillating.

The top two subplots of figure 3.16 show the GDOP and 3D position errors for three different scenarios. The first is if all of the satellites are included, shown by the green line. The second is after removing only PRN 16 from the processing, shown in red. The third is after removing only PRN 27, shown in blue. The bottom subplot shows the scintillation index for all visible satellites, clearly showing the two that are scintillating. We can see that the removal of PRN 16 has a large impact on the GDOP, increasing it from 5 to 9 by the end of this time frame. This increase in GDOP results in a large increase in position errors. The skyplot shows that PRN 16 is the only satellite coming from the northwest direction, which means it has a significant contribution to the GDOP. On the other hand,

PRN 27 is surrounded by three other satellites, so its contribution to the GDOP is not nearly as significant. The top subplot shows that the GDOP barely changes after removing this satellite. The 3D position errors decrease a small amount as a result of removing this scintillating satellite from the processing. In this case, the benefits of removing this satellite's measurements outweighs the impact from the degradation in GDOP. This result will be utilized in one of the adaptive algorithms.

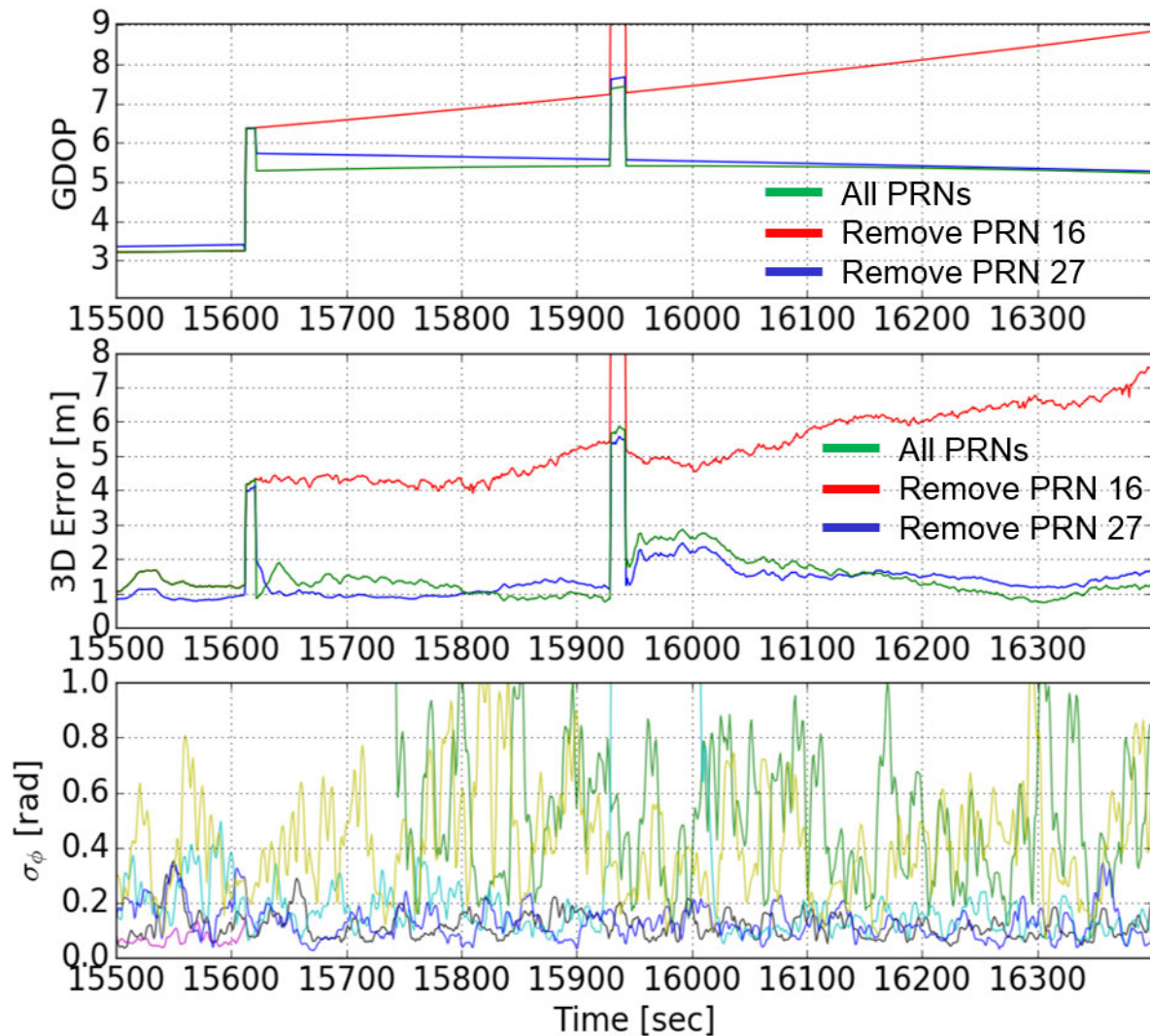


Figure 3.16: Jicamarca, Peru position errors after removing satellites. 23:18-23:35 LT on 11/3/2014. Subplot 1: GDOP for all satellites (green), after removing PRN 16 (red), after removing PRN 27 (blue). Subplot 2: 3D position errors for all satellites (green), after removing PRN 16 (red), after removing PRN 27 (blue). Subplot 3: σ_ϕ for all satellites. Different colors represent different satellites.

Another note is that this example only has 6 satellites that are used in the position solution because we are using GPS satellites only. If multi-GNSS was incorporated, there would be many more visible satellites, which would improve the GDOP. If this were the case, we could possibly remove more scintillating satellites with less impact to the GDOP. For example, it is possible that PRN 16 and PRN 27 could be removed if there were other non-scintillating satellites from other constellations contributing to the GDOP.

3.6 Weighting Measurements Impacted by Scintillation

Here, we explore how weighting a scintillating satellite's measurements impacts the position solution. This is done by incorporating a weight matrix W into the LSE formula from equation 1.13. The diagonal matrix W (size $K \times K$) puts a weight on each satellite's measurements to adjust the influence it has on the position estimation. We want to place a smaller weight on a satellite that is scintillating. The adjustment to equation 1.13 with the weight matrix W is shown below. In this W matrix, the diagonal element associated with each satellite is normally set to 1, indicating no weights for any satellite.

$$\begin{bmatrix} \delta \vec{x} \\ \delta b \end{bmatrix} = (\mathbf{G}^T \mathbf{W} \mathbf{G})^{-1} \mathbf{G}^T \mathbf{W} \delta \vec{\rho} \quad (3.15)$$

Using the same data segment from Peru as the previous section, various weights are applied to PRN 16. The GDOP and 3D position errors are shown in figure 3.17. We see the same result as the last section when we completely remove this satellite, shown in the line in blue. Each weight ranging from 0.1 to 0.6 results in position errors that are in between the extremes of leaving the satellite in the processing with no weight, and completely removing it. A similar result is shown in figure 3.18 for PRN 27. Note that a weight of zero is the same as completely removing the satellite.

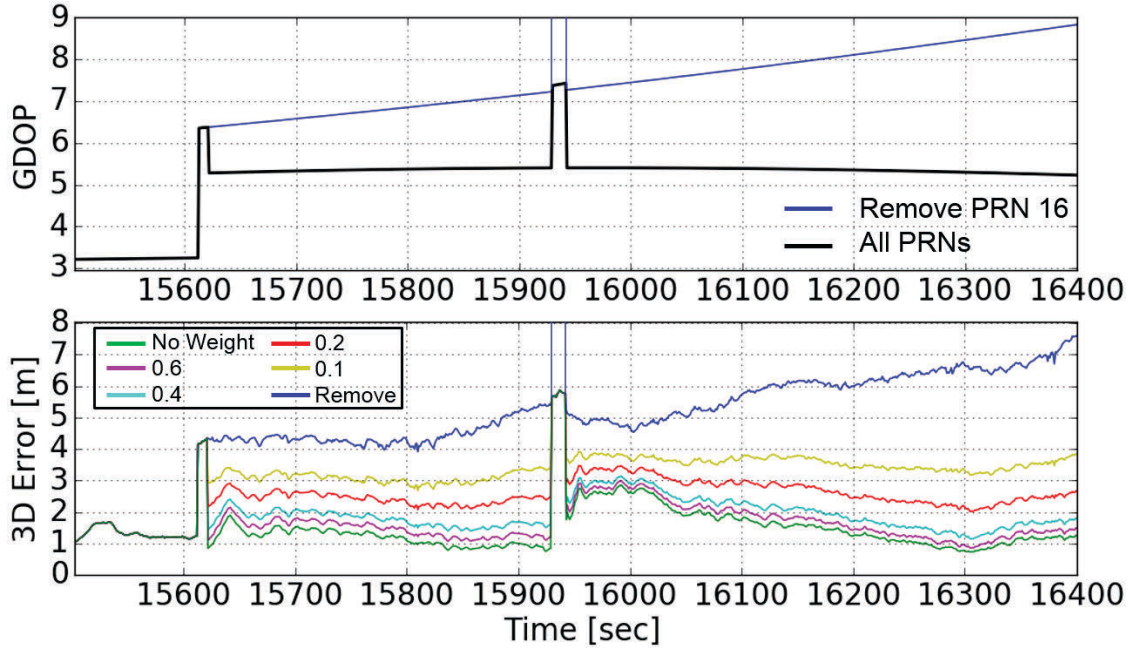


Figure 3.17: Jicamarca, Peru position errors after weighting PRN 16. 23:18-23:35 LT on 11/3/2014. Top: GDOP for all satellites (black), after removing PRN 16 (blue). Bottom: 3D errors using all satellites (green), and using weights on PRN 16 of 0.6 (magenta), 0.4 (cyan), 0.2 (red), 0.1 (yellow), and 0.0 (blue).

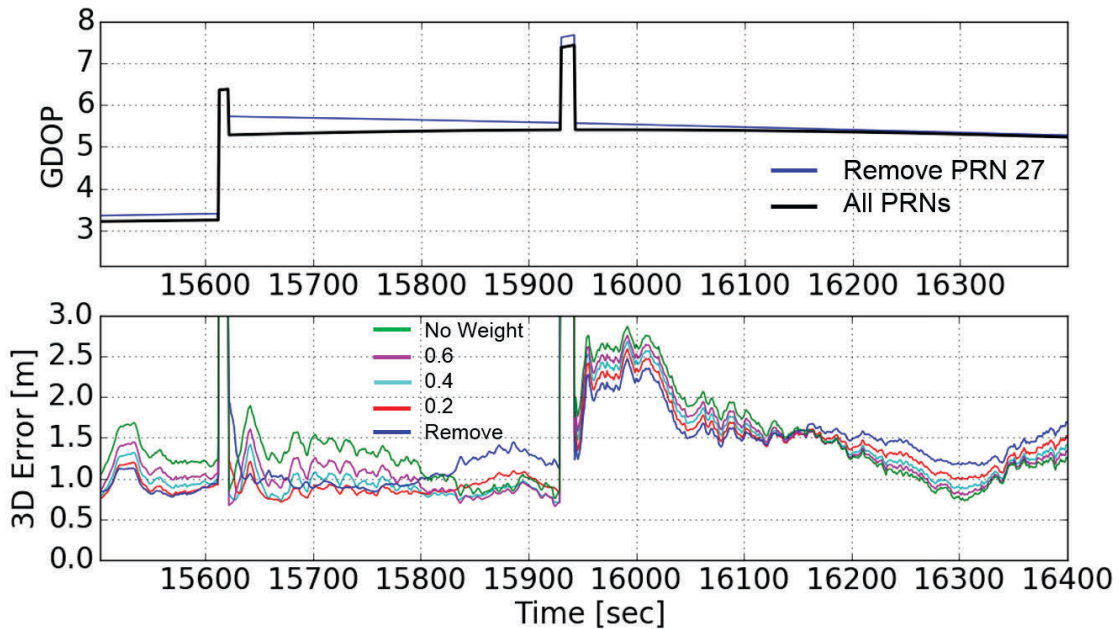


Figure 3.18: Jicamarca, Peru position errors after weighting PRN 27. 23:18-23:35 LT on 11/3/2014. Top: GDOP for all satellites (black), after removing PRN 27 (blue). Bottom: 3D errors using all satellites (green), and using weights on PRN 27 of 0.6 (magenta), 0.4 (cyan), 0.2 (red), and 0.0 (blue).

These examples make it clear on what happens when a satellite is weighted rather than removed from the navigation processing. Depending on the value of the weight, the position solution will be somewhere in between using no weight on the satellite (weight equal to 1), and completely removing the satellite (weight equal to 0). The adaptive algorithms in the following section will take into account this approach of weighting scintillating satellites.

3.7 Adaptive Positioning Algorithms

So far in this chapter, we have gone through some approaches that can be used to mitigate the three main scintillation effects on GNSS measurements. This section goes through two adaptive positioning techniques that use some of these approaches in the presence of ionospheric scintillation. Each algorithm is placed into a subsection, but features that are common to both of these algorithms are highlighted below.

Each positioning algorithm uses the classic least squares estimation technique, along with the same dual frequency ionosphere corrections and Hopfield model troposphere corrections that were explained in chapter 1. Satellite and receiver hardware bias corrections are also applied. At every epoch, satellites are selected to be used in the position calculation. Ideally, we want to use every satellite in view of the receiver. This is not always possible because of low quality measurements that often appear near the beginning or end of a satellite pass. These measurements are filtered out to avoid any trivial errors. Each positioning algorithm only selects satellites if their measurements satisfy all of the following conditions:

- "Healthy" status is broadcast from the ephemeris
- C/N_0 exceeds a 25 dB-Hz threshold
- Elevation angle exceeds a threshold of 15 degrees
- Contains a range measurement on both the L1 and L2 frequencies. L2C is used if available. Otherwise L2P is used.
- Range measurements must be within a conservative scope for a typical GPS orbit (19,000 - 27,000 km) to avoid any extraneous values.

Generally, these restrictions are set to exclude problematic satellites that have signals with low power, inaccurate range measurements, inability to perform ionospheric corrections, and any other general malfunctions. Each of the following algorithms focuses on problems associated with scintillation.

3.7.1 Adaptive Positioning based on Phase Scintillation Detection ($A\text{-}\sigma_\phi$)

This algorithm applies adaptive positioning based on phase scintillation detection ($A\text{-}\sigma_\phi$). It primarily uses the hybrid Hatch filter/CNMP carrier-smoothed pseudoranges to find the receiver's position. The defining feature of this algorithm is that the σ_ϕ value from each satellite is continuously monitored. If σ_ϕ exceeds a threshold of 0.7 radians, then the carrier-smoothed pseudorange measurements will be abandoned on this particular satellite, and the unsmoothed pseudorange measurements will be substituted in the navigation processing. As soon as σ_ϕ returns to a value below the threshold, we resume using the carrier-smoothed pseudoranges. In addition, if we have unsmoothed pseudorange measurements when there are dropped ADR measurements, the unsmoothed pseudoranges will be used. A visual of this algorithm is shown in figure 3.19.

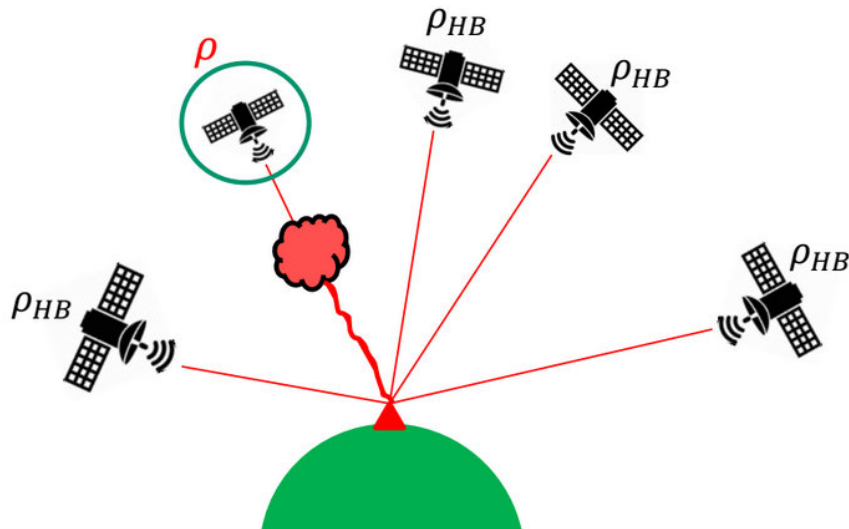


Figure 3.19: Visual of $A\text{-}\sigma_\phi$ algorithm. The satellite experiencing scintillation uses unsmoothed pseudoranges (ρ), while the other satellites use carrier-smoothed pseudoranges (ρ_{HB}).

A variant of this algorithm is that the satellite that is using the unsmoothed pseudoranges could be weighted. Normally in the W matrix from equation 3.15, the diagonal element associated with each satellite is set to 1, indicating no weights for any satellite. This variant sets this diagonal element to a value of 0.2, which was heuristically decided upon. A block diagram for the $A\text{-}\sigma_\phi$ algorithm is shown in figure 3.20.

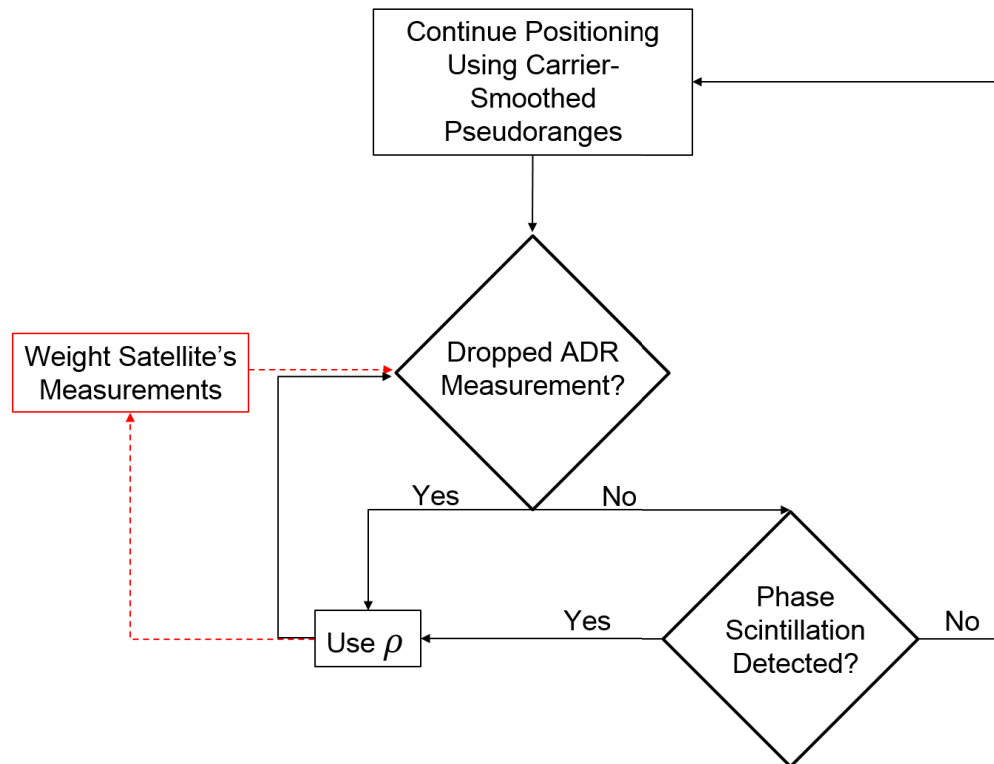


Figure 3.20: Block diagram of $A\text{-}\sigma_\phi$ algorithm. The red path indicates the variant of this algorithm that includes weighting the satellite using the unsmoothed pseudorange measurements.

3.7.2 Adaptive Positioning based on GDOP Analysis ($A\text{-GDOP}$)

The second algorithm completely excludes satellites from the navigation processing if they are experiencing scintillation. Normally, we can get improved operation from a GPS receiver by using all of the visible satellites. More visible satellites means a smaller value of GDOP, which likely yields more accurate positioning results. However, in certain scenarios it is possible to omit satellites without severely impairing the GDOP as we saw in section 3.5. If a satellite has scintillation, the low quality of the measurements will degrade the position

solution more than the positive impact it has on the GDOP. This is similar to other studies such as [38], which shows that it is not always best to use every available satellite because of influence of other error sources such as multipath and a low C/N_0 .

The adaptive positioning based on GDOP analysis (*A-GDOP*) computes the GDOP using equations 3.16 and 3.17, which is derived from the previously defined \mathbf{G} matrix.

$$\mathbf{H} = (\mathbf{G}^T \mathbf{G})^{-1} \quad (3.16)$$

The 4×4 \mathbf{H} matrix is proportional to the covariance of the estimated position errors calculated in equation 1.13. GDOP is calculated using the diagonal elements of \mathbf{H} .

$$GDOP = \sqrt{H_{1,1} + H_{2,2} + H_{3,3} + H_{4,4}} \quad (3.17)$$

A-GDOP performs this calculation both before and after the exclusion of a scintillating satellite from the \mathbf{G} matrix. If the GDOP increases by a margin larger than 2, the satellite will not be removed from the navigation processing. If the change in GDOP is less than 2, this algorithm will exclude this satellite's measurements. Figure 3.21 gives a visual of this algorithm. If the scintillating satellite in the left plot is removed, the change in the GDOP would be small because of the surrounding satellites. In this case, this satellite would be removed from the navigation processing. However, if the scintillating satellite in the right plot is removed, the GDOP would likely increase significantly because the remaining satellite signals are coming from a similar direction. In this case, this satellite would not be removed from the navigation processing.

Another note is that this algorithm could also apply weights to the scintillating satellites rather than completely remove them. This option is shown in red in the block diagram of the *A-GDOP* algorithm shown in figure 3.22. Since we already know that applying a weight will give a solution that is in between completely removing a satellite and keeping its measurements, this weighted approach is not explored in the following chapter.

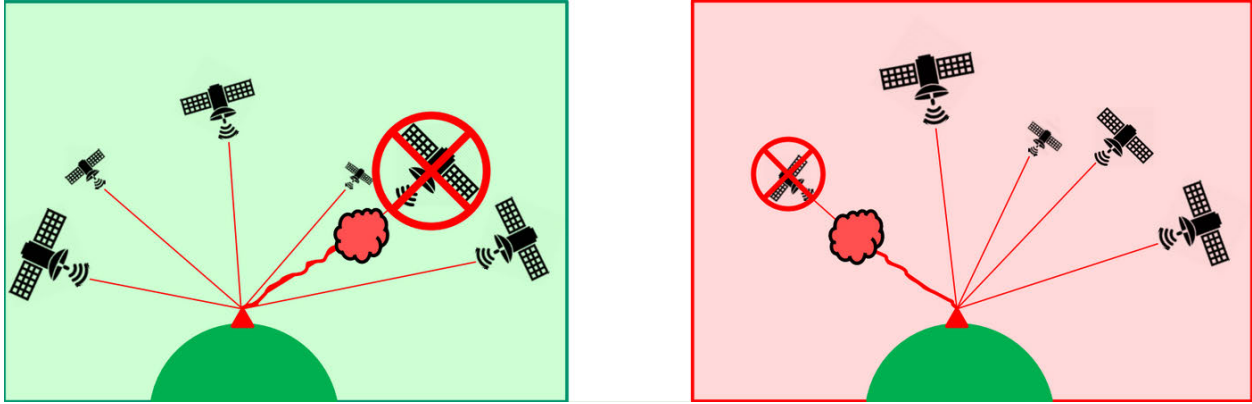


Figure 3.21: Visual of *A-GDOP* algorithm. The left shows the removal of a scintillating satellite without a large impact to the GDOP. The right shows the removal of a satellite that would have a large impact to the GDOP.

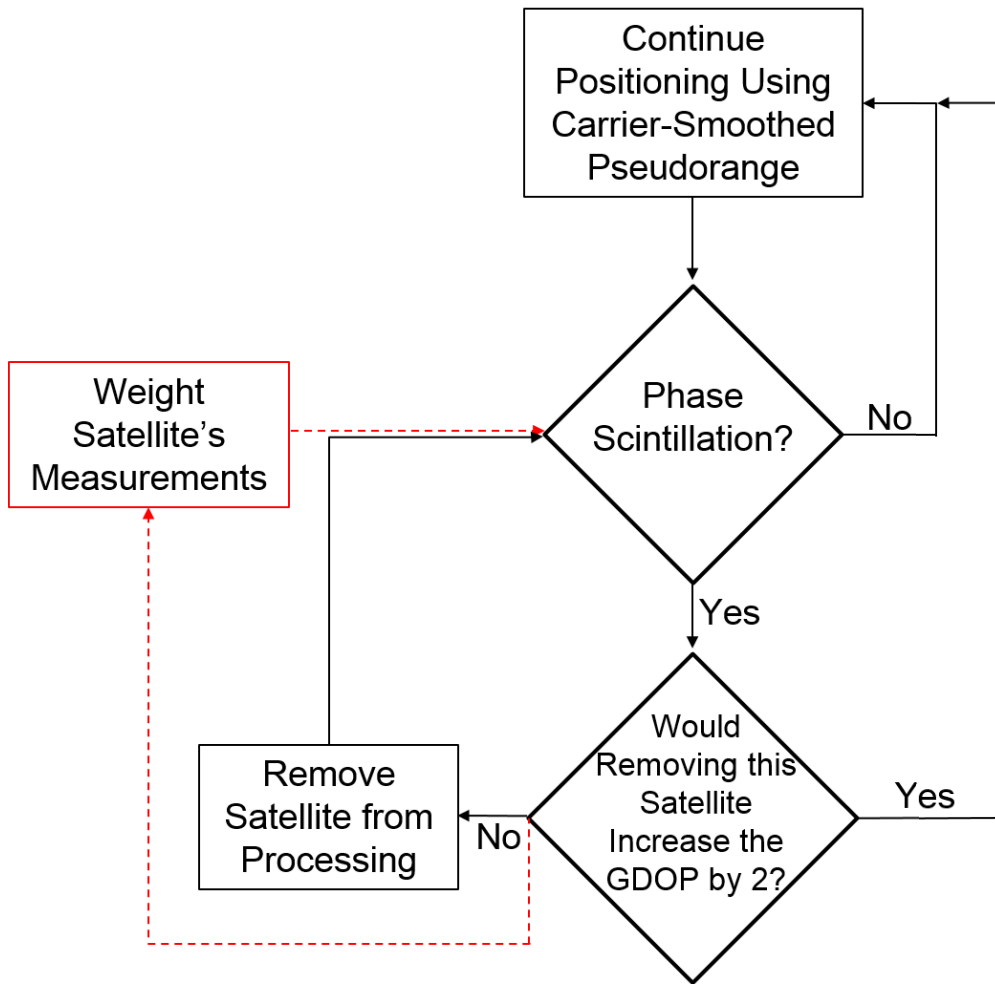


Figure 3.22: Block diagram of *A-GDOP* algorithm. The red path indicates a variant of this algorithm that includes weighting the satellite using the unsmoothed pseudorange measurements.

When there is only 1 or 2 satellites with scintillation, this algorithm is simple to execute. However, when there are multiple satellites with scintillation, optimizing the selection of satellites becomes somewhat challenging and computationally expensive. In this thesis, these situations are handled with manual intervention to ensure a good choice when excluding satellites. In the future, additional algorithms such as the ones presented in [39] could be utilized to enhance the satellite selection process during a scintillation event that affects several satellites. Another feature that could improve this algorithm in the future would be multi-GNSS capability. More satellites from other constellations would give better GDOP values, and allow for the removal of more (or possibly all) of the scintillating satellites with less of an impact to the GDOP.

3.7.3 Summary of Positioning Algorithms

There are many available techniques that could be included in each positioning algorithm. New algorithms could be created by selecting different combinations of the type of carrier-smoothing, weighting, and cycle slip detection and repair. Also, the thresholds that are used in these algorithms could all be adjusted. For a more general comparison, seven positioning algorithms have been selected and analyzed in chapter 4. The different features included in each algorithm are summarized in table 3.2. The following list clarifies the notation of the unsmoothed pseudoranges that are used in these algorithms.

- ρ_c - unsmoothed pseudorange (used in algorithm 1)
- ρ_B - carrier-smoothed pseudorange using bias estimates from the post-processed CNMP method. Carrier phase measurements that were affected by cycle slips are discarded rather than repaired. (Used in algorithm 2)
- ρ_H - carrier-smoothed pseudorange using a Hatch filter (used in algorithm 3)
- ρ_{HB} - carrier-smoothed pseudorange using the new hybrid Hatch filter/CNMP technique (used in algorithm 4, and all of the adaptive algorithms)

Table 3.2: Summary of positioning algorithms.

Algorithm	1	2	3	4	$A\text{-}\sigma_\phi$	Weighted $A\text{-}\sigma_\phi$	A-GDOP
Carrier-Smoothed Pseudorange	ρ_c	ρ_B	ρ_H	ρ_{BH}	ρ_{BH}	ρ_{BH}	ρ_{BH}
Real Time	✓	✗	✓	✓	✓	✓	✓
Cycle Slip Detection & Repair	✗	✗	✓	✓	✓	✓	✓
Weights Applied to Satellites	✗	✗	✗	✗	✗	✓	✗
Allow Changes in GDOP	✗	✓	✗	✗	✗	✗	✓

CHAPTER 4

RESULTS

4.1 Comparison of Positioning Algorithms During Scintillation

In this section, we will examine the positioning algorithms listed in table 3.2. As summarized in the table, the following results and algorithms were produced after repairing all cycle slips. Each data set selected in this section generally contain 20-60 minutes of strong scintillation. Since cycle slips were repaired, errors in this section are mostly due to scintillation induced phase fluctuations and changes in GDOP. One of the goals for this section is to test the established algorithms to see if they can out-perform conventional approaches during scintillation. The three conventional algorithms to compare against are in the first three columns of table 3.2. Algorithm 1 (which uses ρ_c measurements) is the most basic technique, identical to the derivations in section 1.3. Algorithm 2 discards all data that contains cycle slips rather than repairing them, which is common to do in post processing. After this data is discarded, the CNMP method is used for carrier-smoothing. This algorithm was included to see the what happens when data is discarded, and should not be heavily compared to the real time techniques. The third conventional technique is algorithm 3 (which uses ρ_H measurements from the Hatch filter), which is utilized in the real time operation of many receivers. The remaining four techniques consist of the adaptive algorithms discussed in this thesis, and have unique features with the potential to improve upon the customary algorithms. Our results show that the performance of these algorithms is dependant on the number of satellites scintillating. Therefore, the results will be split into three subsections with one satellite scintillating, two satellites scintillating, and three or more satellites scintillating in order to provide a fair comparison in each subsection.

4.1.1 Positioning Results: 1 Satellite Scintillating

An example will be presented that explains how these algorithms perform when there is only one satellite scintillating at a time. Refer to figure 4.1, which shows a skyplot in Ascension Island where PRN 31 experiences strong scintillation. PRN 30 enters the frame with strong σ_ϕ values once PRN 31 stops scintillating. Since PRN 30 is at a very low elevation angle, these σ_ϕ values are most likely not due to scintillation, but could be due to multipath or a weak signal from the low elevation. This satellite demonstrates when it is not always easy to distinguish between scintillation and other interference effects.

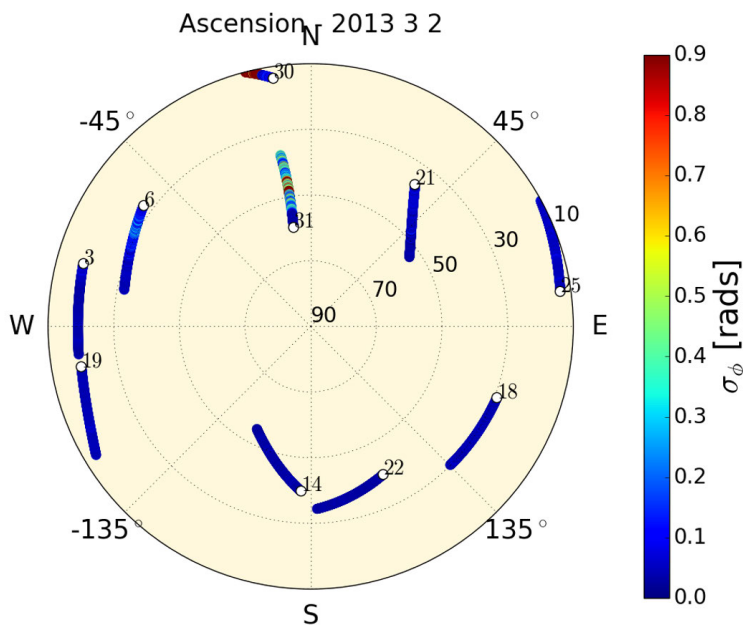


Figure 4.1: Ascension Island skyplot. 3/2/2013, 00:03-00:50 LT. Satellite tracks are colored by the σ_ϕ value in radians.

First, the statistical results of all of the algorithms for this data set are shown in figure 4.2 for this time frame in the left subplot. For a comparison, the right plot shows a similar time frame for the following day where there was no scintillation (referred to as a quiet day). Since the satellites are roughly on a 12 hour orbit, we will see the same satellites in approximately the same locations as the day before. In these statistics, the large bar indicates the mean 3D error, the thick error bar shows the standard deviation, and the thin error bar shows the maximum 3D error. Focusing on algorithms 3 and 4 (Hatch filter and hybrid technique), we

see similar performance in this data set. Introducing the unsmoothed pseudorange for the scintillating satellite in the $A\text{-}\sigma_\phi$ algorithm slightly increases the maximum and mean error from algorithm 4. The weighted version of this algorithm avoids this increase in maximum error. After removal of the scintillating satellite in the $A\text{-GDOP}$ algorithm, all errors are significantly reduced. In fact, the errors are comparable to what is seen on the quiet day in the right subplot. Notice that on the quiet day, the adaptive algorithms have the same results because there is no scintillation activity to adapt to.

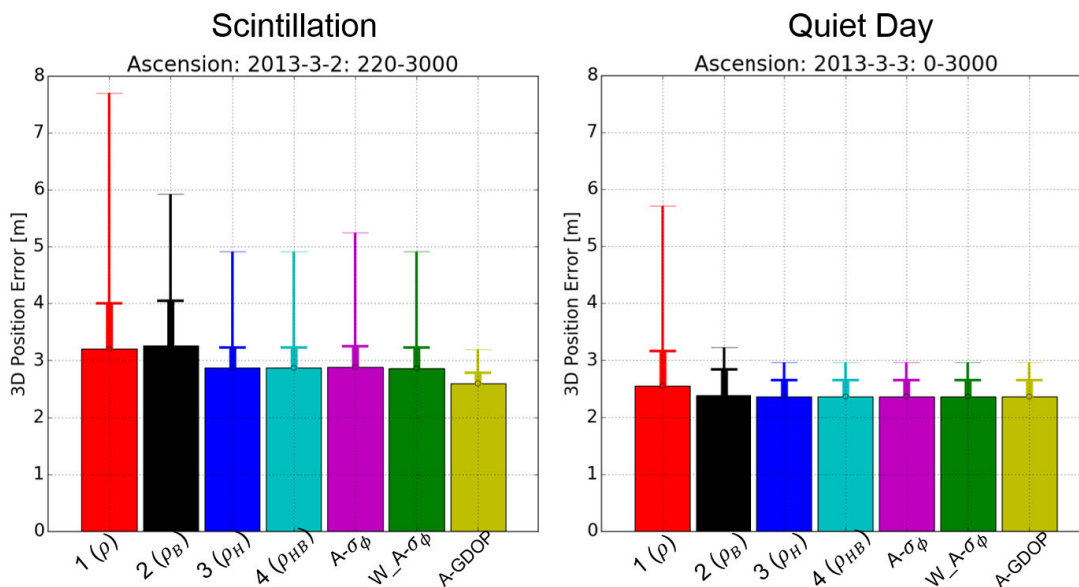


Figure 4.2: Ascension Island positioning error statistics. 3/2/2013(left) and 3/3/2013(right) 00:00-00:50 LT. Statistical comparison of 3D positioning errors. The large bar indicates the mean error, the thick error bar represents the standard deviation, and the thin error bar shows the maximum error. The left plot is a day with scintillation, and the right plot is a day without scintillation.

Figure 4.3 shows the GDOP, 3D position errors, and σ_ϕ values for algorithm 4, and the $A\text{-GDOP}$ algorithm. Other algorithms are not shown on this plot for an easier comparison and to avoid clutter. Although the GDOP of the $A\text{-GDOP}$ algorithm is increased by about 1, this algorithm shown in red avoids the large jumps and fluctuations in position errors brought on by each scintillating satellite that is included in algorithm 4 in blue.

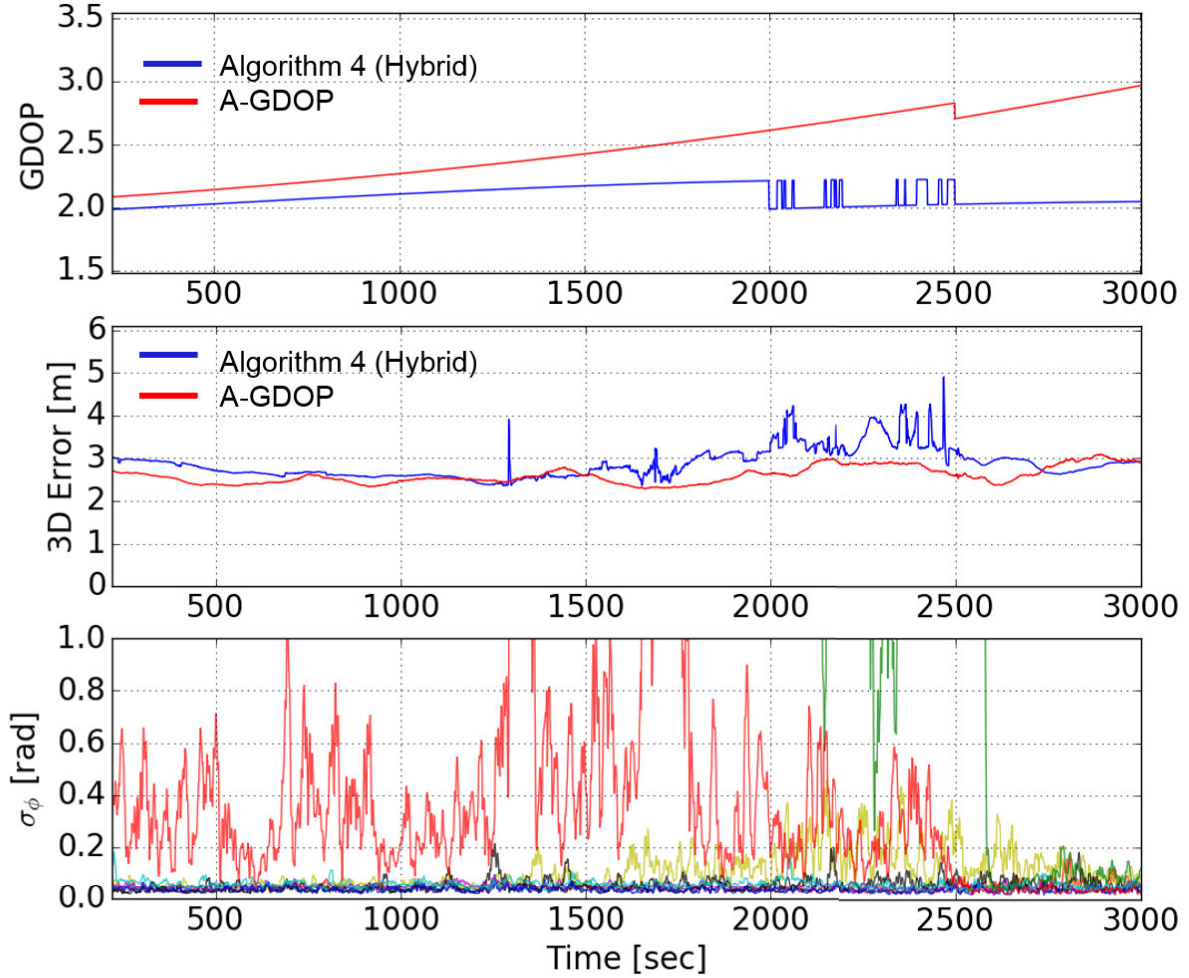


Figure 4.3: Ascension Island positioning algorithms. 3/2/2013 00:03-00:50 LT. Subplot 1: GDOP for algorithm 4 (hybrid technique) in blue and *A-GDOP* algorithm in red. Subplot 2: 3D error of algorithm 4 (blue) and *A-GDOP* (red). Subplot 3: σ_ϕ [radians] for all visible satellites.

Similar to the previous plots, figure 4.4 shows the error statistics for additional data sets where there is only one satellite with strong scintillation. In all of these cases, it appears that the mean error, and maximum error remain the same or decrease by using algorithm 4 instead of algorithm 3. This indicates the new hybrid carrier-smoothing has a better performance than the commonly used Hatch filter. In almost all cases, the maximum error of $A\text{-}\sigma_\phi$ is larger than algorithms 3 and 4 because of the addition of the unsmoothed pseudorange measurements on the single scintillating satellite. Although maximum errors are

still high, the weighted $A\text{-}\sigma_\phi$ algorithm reduces the influence of the variations in the satellite's unsmoothed pseudorange measurements, which results in a smaller maximum error in each data set relative to the standard $A\text{-}\sigma_\phi$ algorithm. Last, $A\text{-GDOP}$ reduces the maximum error relative to algorithm 3 in every data set, through the simple removal of the scintillating satellite's measurements. However, this also raises the mean error in a few data sets as a result of the increase in GDOP. In addition, skyplots are provided in figure 4.5 to give an idea of which satellite is scintillating, and how many other satellites are contributing to the position solution. Notice that the top left and middle left skyplots have more satellites than the other data sets. The corresponding mean errors in figure 4.4 are much smaller than the other data sets. This shows how using more satellites (thus improving the GDOP) improves the position solution. Numerical statistics of these data sets are provided in table 4.1.

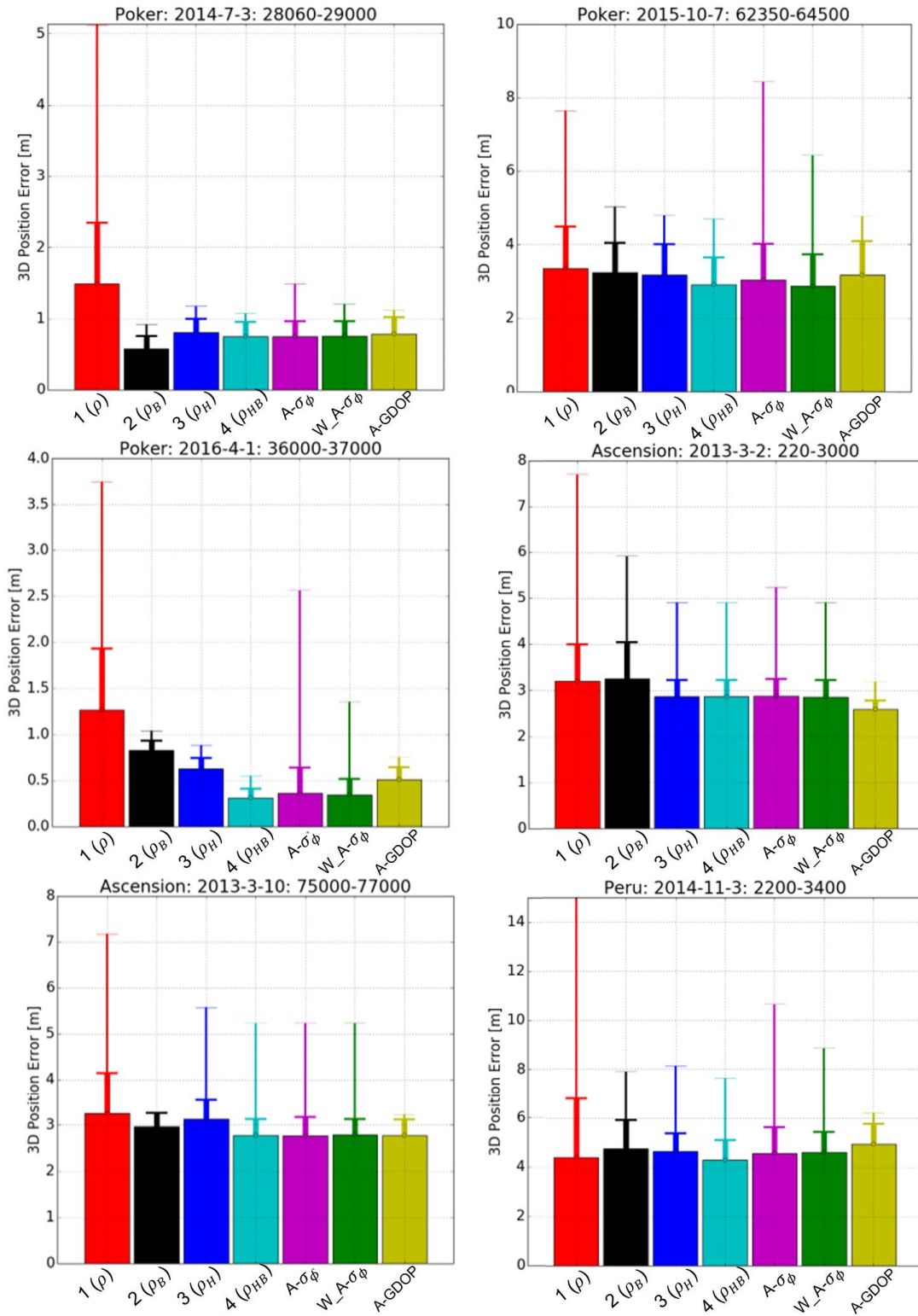


Figure 4.4: Positioning error statistics: one satellite scintillating. Large bar - mean, thick error bar - standard deviation, thin error bar - maximum.

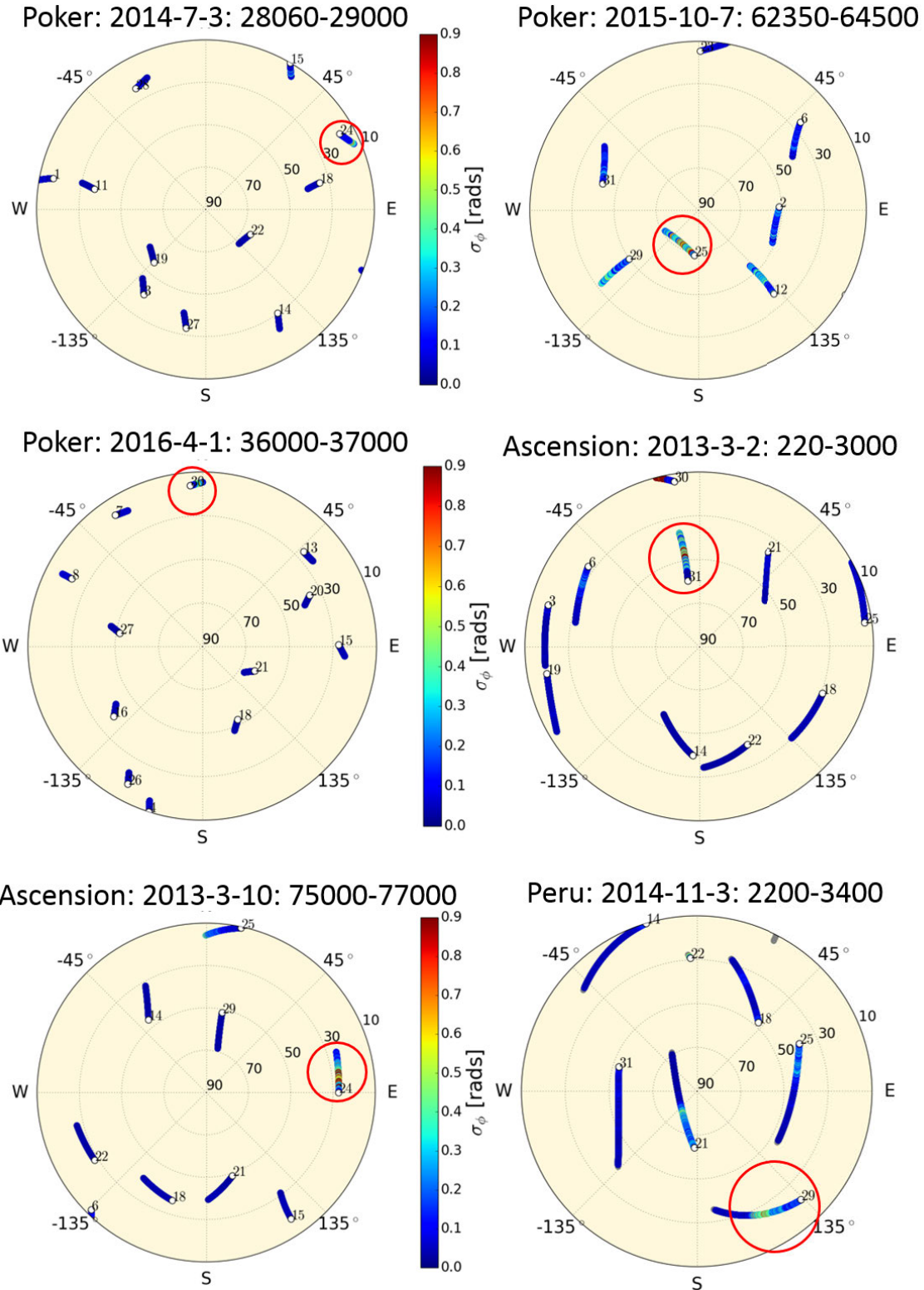


Figure 4.5: Skyplots: days with one satellite scintillating. Corresponds with figure 4.4. Satellite tracks are colored by their value of σ_ϕ in radians. The scintillating satellite is circled in red in each skyplot.

In this table, we present the error reduction as percentages for algorithm 4, A -GDOP, A - σ_ϕ , and the weighted A - σ_ϕ algorithm. We need a baseline value to calculate an error reduction, so all of these statistics were compared directly to algorithm 3. Negative values in the table indicate worse performance in that category.

For algorithm 4, we see improvement in maximum error ranging from 0-37%, and 0-50% in the mean error. In one of the data sets, the standard deviation grows by 8%, but it is reduced in the remaining data sets by up to 18%. The A -GDOP algorithm tends to have better maximum error reduction, with improvement from 0-42%. However, the mean error reduction only reaches a value of 20%, and actually increases the mean in two data sets. In almost all of these cases, the two A - σ_ϕ algorithms increase the errors compared to standard techniques because of the inclusion of the noisier unsmoothed pseudorange measurements. However, the weighted A - σ_ϕ algorithm generally has a better performance than the regular A - σ_ϕ .

Table 4.1: Adaptive positioning algorithm performance - 1 satellite scintillating. Reduction in 3D error of algorithm 4 (ρ_{HB}), A -GDOP, and A - σ_ϕ algorithms with one satellite experiencing scintillation as compared to algorithm 3 (ρ_H)

Error Reduction of Algorithms \rightarrow	Algorithm 4	A -GDOP	A - σ_ϕ	Weighted A - σ_ϕ
Data Set \downarrow	Maximum Mean Std	Maximum Mean Std	Maximum Mean Std	Maximum Mean Std
Alaska: 7/3/2014 23:47 - 00:03 LT	9.09 % 8.64 % 4.74 %	5.69 % 3.71 % -11.51 %	-26.21 % 6.95 % -9.13 %	-2.37 % 6.81 % -9.12 %
Alaska: 10/7/2015 17:19 - 17:55 LT	1.90 % 8.66 % 12.05 %	0.44 % -0.06 % -9.63 %	-75.84 % 4.34 % -19.11 %	-34.10 % 9.57 % -3.50 %
Alaska: 4/1/2016 02:00 - 02:17 LT	37.64 % 50.48 % 18.34 %	14.97 % 20.63 % -8.33 %	-190.75 % 42.49 % -133.56 %	-53.02 % 45.34 % -47.05 %
Ascension Island: 3/2/2013 00:03 - 00:50 LT	0.00 % 0.00 % 0.00 %	34.02 % 7.96 % 49.88 %	-6.70 % -0.31 % -2.50 %	0.00 % 0.82 % -0.40 %
Ascension Island: 3/10/2013 20:50 - 21:22 LT	6.43 % 11.18 % 15.35 %	42.28 % 11.15 % 17.46 %	6.29 % 11.72 % 1.39 %	6.29 % 11.24 % 16.26 %
Peru: 11/3/2014 19:36 - 19:57 LT	7.45 % 7.39 % -8.26 %	24.16 % -9.36 % -13.19 %	-31.45 % 2.12 % -46.78 %	-8.92 % 1.43 % -9.13 %

4.1.2 Positioning Results: 2 Satellites Scintillating

Next, an example will be shown followed by statistical results of data sets that have up to two satellites scintillating at once. For this example, refer to the skyplot in figure 4.6 which shows PRN 31 and PRN 19 experiencing scintillation simultaneously in Ascension Island.

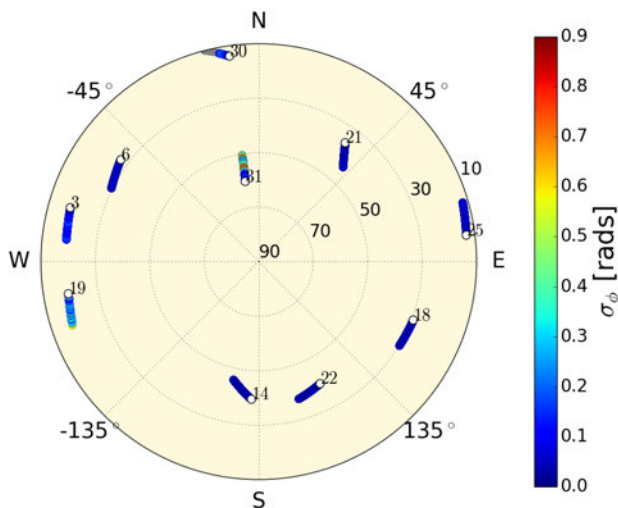


Figure 4.6: Ascension Island skyplot. 3/9/2013, 00:02-00:20 LT. Satellite tracks are colored by the σ_ϕ value in radians.

Statistical results for this day are shown in the left subplot of figure 4.7. In this scenario, algorithms 3, 4, $A\text{-}\sigma_\phi$, and weighted $A\text{-}\sigma_\phi$ appear to have a similar performance, due to the fact that the maximum errors occur at a time when the σ_ϕ value is below the threshold of 0.7 radians. However, the $A\text{-}GDOP$ algorithm reduces the maximum and mean errors by removing the scintillating satellites. As a nominal comparison of these errors, the subplot on the right shows the errors from the day before, where there was only very mild scintillation recorded on one satellite.

Figure 4.8 compares GDOP and position error for algorithm 4 in blue with the $A\text{-}GDOP$ algorithm in red. After removing the scintillating satellites in the $A\text{-}GDOP$ algorithm, the GDOP only increases by about 0.4, and this algorithm avoids jumps in the position solution induced by the scintillating satellites.

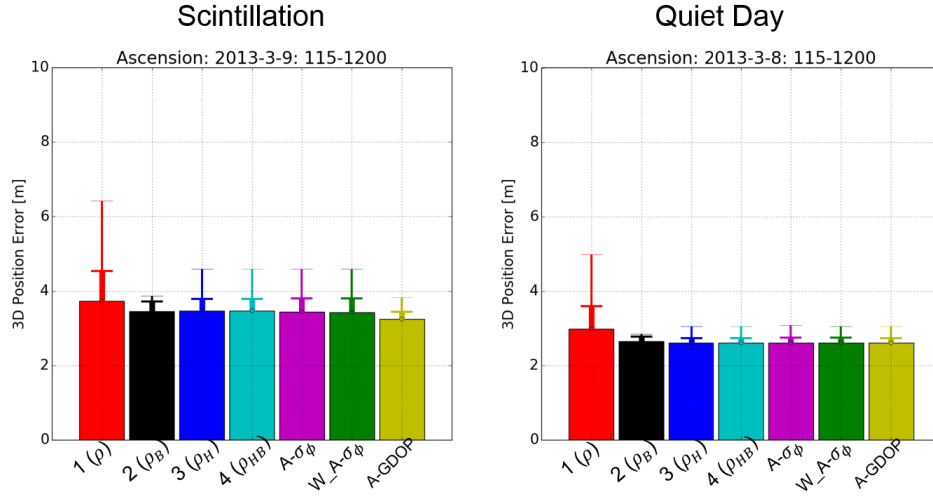


Figure 4.7: Ascension Island positioning error statistics. 3/9/2013(left) and 3/8/2013(right) 02:00-00:20 LT. Statistical comparison of 3D positioning errors. The large bar indicates the mean, the thick error bar represents the standard deviation, and the thin error bar shows the maximum. The left plot is a day with scintillation, and the right plot is a day with only moderate scintillation.

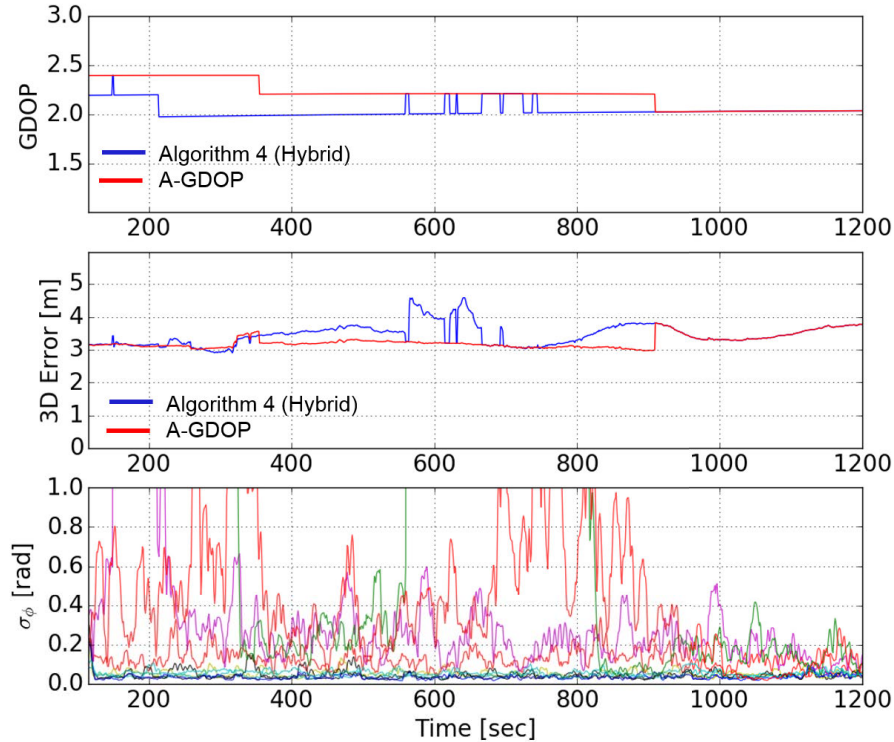


Figure 4.8: Ascension Island positioning algorithms. 3/2/2013 00:02-00:20 LT. Subplot 1: GDOP for algorithm 4 (hybrid technique) in blue and *A-GDOP* algorithm in red. Subplot 2: 3D error of algorithm 4 (blue) and *A-GDOP* (red). Subplot 3: σ_ϕ [radians] for all visible satellites.

The following data sets each contain up to two satellites simultaneously scintillating. Upon a quick inspection of figure 4.9, algorithm 4 still has smaller mean and maximum errors than algorithm 3, just like the previous section. The $A\text{-}\sigma_\phi$ very slightly increases mean errors when compared to algorithm 4. However, the weighted $A\text{-}\sigma_\phi$ seems to slightly improve mean errors in these data sets. The $A\text{-GDOP}$ algorithm reduces maximum and mean errors in most cases. Table 4.2 more clearly quantifies the improvement.

In all but one case, algorithm 4 reduces maximum errors up to 10%, and reduces mean errors in every data set by up to 17% when comparing to algorithm 3. The standard deviation also decreases by up to 25%. $A\text{-GDOP}$ reduces errors by up to 29%, 29%, and 42% for the maximum, mean, and standard deviation, respectively. This algorithm also results in very small error increases of 0-2% in a few of the categories. $A\text{-GDOP}$ performs well when there are two satellites scintillating because the algorithm now has the option of selecting either one or both of the satellites to remove from processing based on the impact to the GDOP. In every data set, removing at least one of the scintillating satellites actually reduced the mean error instead of increasing it like we saw in the previous section. The weighted $A\text{-}\sigma_\phi$ algorithm does slightly better than the regular $A\text{-}\sigma_\phi$, but the change is not as drastic as the last section in terms of maximum errors. These $A\text{-}\sigma_\phi$ algorithms rarely have an error reduction that is better than algorithm 4.

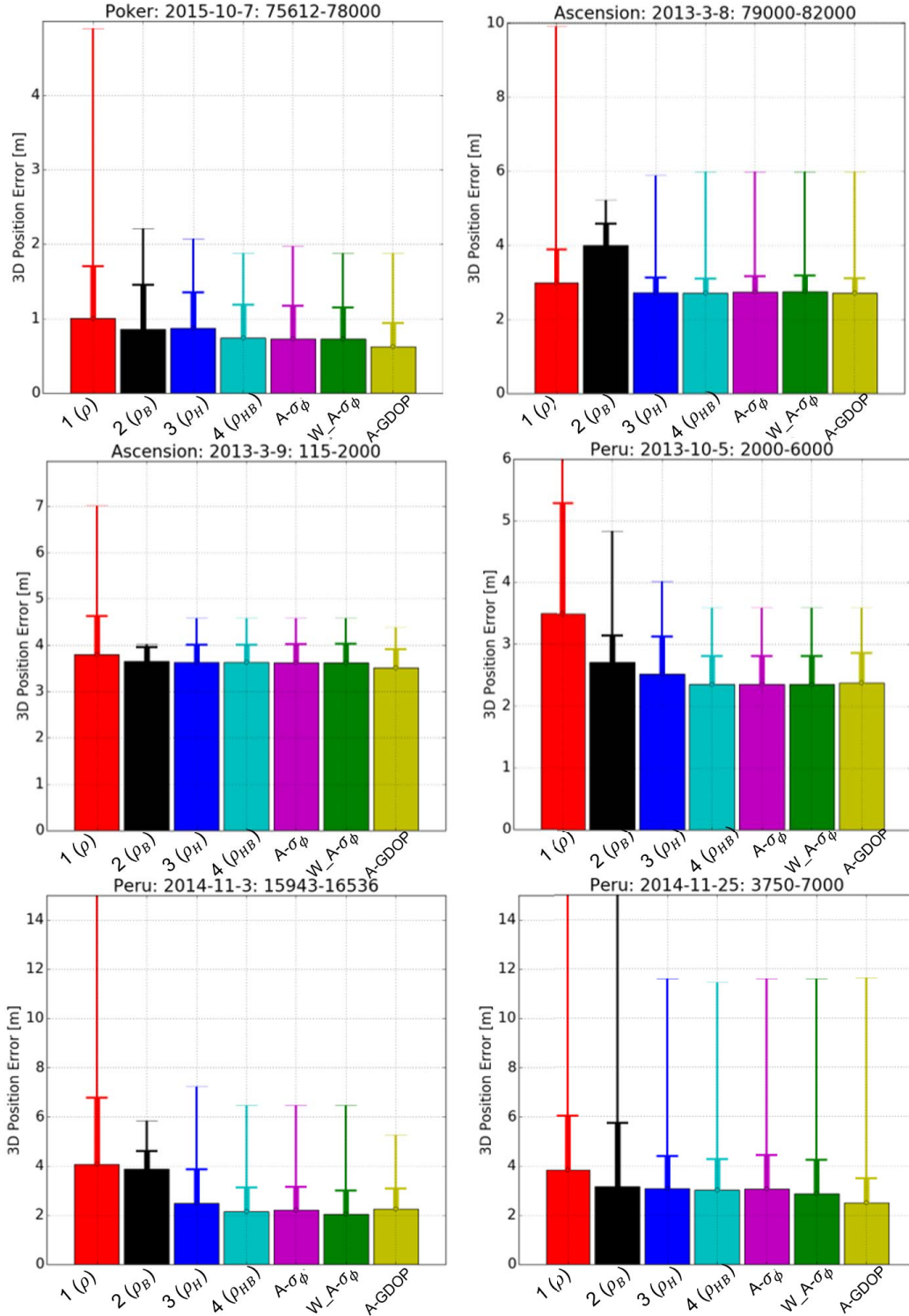


Figure 4.9: Positioning error statistics: two satellites scintillating. Large bar - mean, thick error bar - standard deviation, thin error bar - maximum .

Table 4.2: Adaptive positioning algorithm performance - 2 satellites scintillating. Reduction in 3D error of algorithm 4 (ρ_{HB}), A -GDOP, and A - σ_ϕ algorithms with two satellites experiencing scintillation as compared to algorithm 3 (ρ_H)

Error Reduction of Algorithms \rightarrow	Algorithm 4	A -GDOP	A - σ_ϕ	Weighted A - σ_ϕ
Data Set \downarrow	Maximum Mean Std	Maximum Mean Std	Maximum Mean Std	Maximum Mean Std
Alaska: 10/7/2015	10.57 %	10.57 %	4.90 %	10.57 %
13:00 - 13:40 LT	17.71 % 8.09 %	29.60 % 24.23 %	18.26 % 8.77 %	18.46 % 9.24 %
Ascension Island: 3/8/2013	-1.45%	-1.45 %	-1.56 %	-1.56 %
21:56 - 22:47 LT	0.55 % 1.53 %	0.58 % 0.76 %	-0.29 % -8.17 %	-0.95 % -8.25 %
Ascension Island: 3/9/2013	0.00 %	4.47 %	0.00 %	0.00 %
00:01 - 00:34 LT	0.00 % 0.00 %	3.31 % -1.32 %	0.43 % -7.76 %	0.46 % -8.29 %
Peru: 10/5/2013	10.74 %	10.74 %	10.74 %	10.74 %
19:33 - 20:40 LT	6.74 % 25.24 %	5.55 % 21.31 %	6.54 % 24.51 %	6.72 % 24.74 %
Peru: 11/3/2014	10.35 %	29.02 %	10.35 %	10.35 %
23:25 - 23:36 LT	13.60 % 19.17 %	4.37 % 42.06 %	10.10 % 15.02 %	17.38 % 12.11 %
Peru: 11/25/2014	1.99%	-0.03 %	0.00 %	0.00 %
20:02 - 20:57 LT	2.91 % 9.82 %	21.54 % 24.06 %	0.96 % -4.02 %	6.33 % -3.96 %

4.1.3 Positioning Results: 3 or More Satellites Scintillating

In this last example from Poker Flat, Alaska on 10/7/2015, there are multiple satellites experiencing scintillation simultaneously. The skyplot in figure 4.10 displays strong phase scintillation on the majority of these satellites. Since there are many satellites scintillating, there are many options of satellites that could be removed in *A-GDOP* to potentially increase the solution accuracy. In this example, PRN 9 and PRN 16 were removed, as they appeared to have the strongest scintillation. Upon first inspection of the performance of the adaptive algorithms in figure 4.11, algorithm 4 reduces the errors from algorithm 3, just like the previous sections. Unlike the other sections, there are larger errors on the weighted $A\text{-}\sigma_\phi$ algorithm as compared to the standard $A\text{-}\sigma_\phi$ algorithm. However, both of these increase the error as compared to algorithm 4. The *A-GDOP* algorithm has a slightly smaller mean error, and a reduction of the maximum error as a result of removing troublesome satellite measurements from PRN 9 and PRN 16. The data set from the day before showed no scintillation, so the right subplot shows nominal position errors during a quiet time at this location as a comparison.

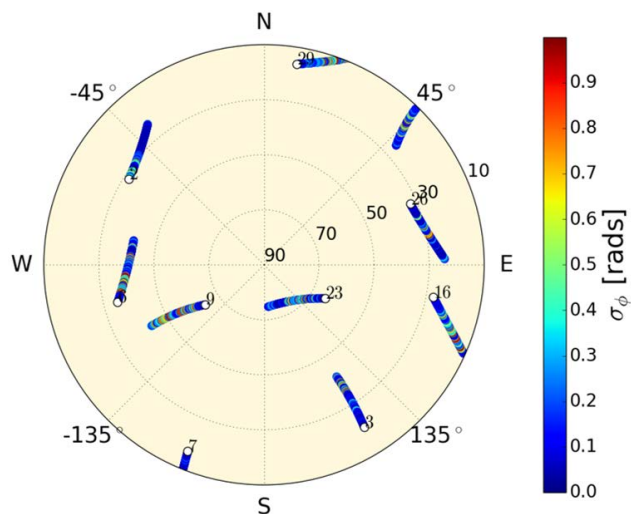


Figure 4.10: Poker Flat, Alaska skyplot. 10/7/2015 22:02 - 22:49 LT. Satellite tracks are colored by the σ_ϕ value in radians.

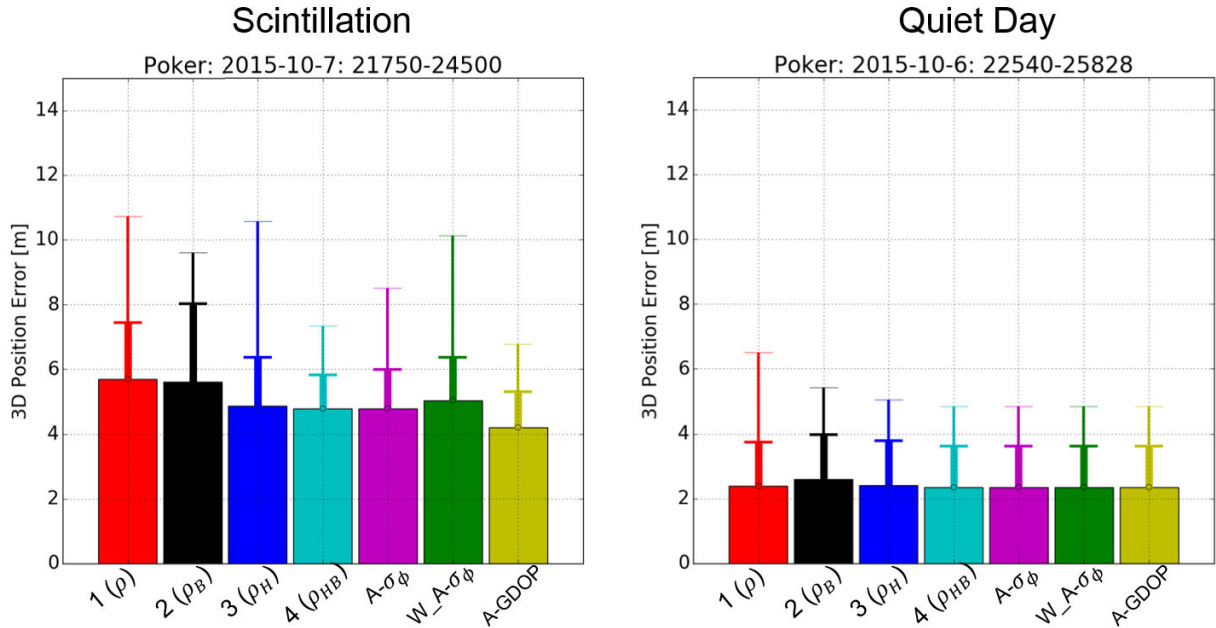


Figure 4.11: Poker Flat, Alaska positioning error statistics. 10/7/2015(left) and 10/6/2015(right) 22:02 - 22:49 LT. Statistical comparison of 3D positioning errors. The large bar indicates the mean error, the thick error bar represents the standard deviation, and the thin error bar shows the maximum error. The left plot is a day with scintillation, and the right plot is a day with no scintillation.

Algorithms 3, 4, and $A-GDOP$ are compared in figure 4.12, which shows the GDOP to be the same for algorithms 3 and 4 (blue and red lines), and a small increase for the $A-GDOP$ algorithm (green line) after removing PRN 9 and PRN 16. The second subplot shows the overlay of the positioning algorithms during this time. Here, we can see the small improvements of algorithm 4 (hybrid) over algorithm 3 (Hatch), as well as the reduction of larger errors in the $A-GDOP$ algorithm.

More data sets with three or more satellites scintillating are shown in figure 4.13. One thing to point out is that position errors have also increased in algorithm 2 as compared to the other scenarios. Since there are multiple satellites scintillating, more cycle slips happen. Throwing out this data severely hurts this post-processed solution in a few of these plots. In the bottom right subplot, the black star above the error bar for algorithm 2 is an indicator

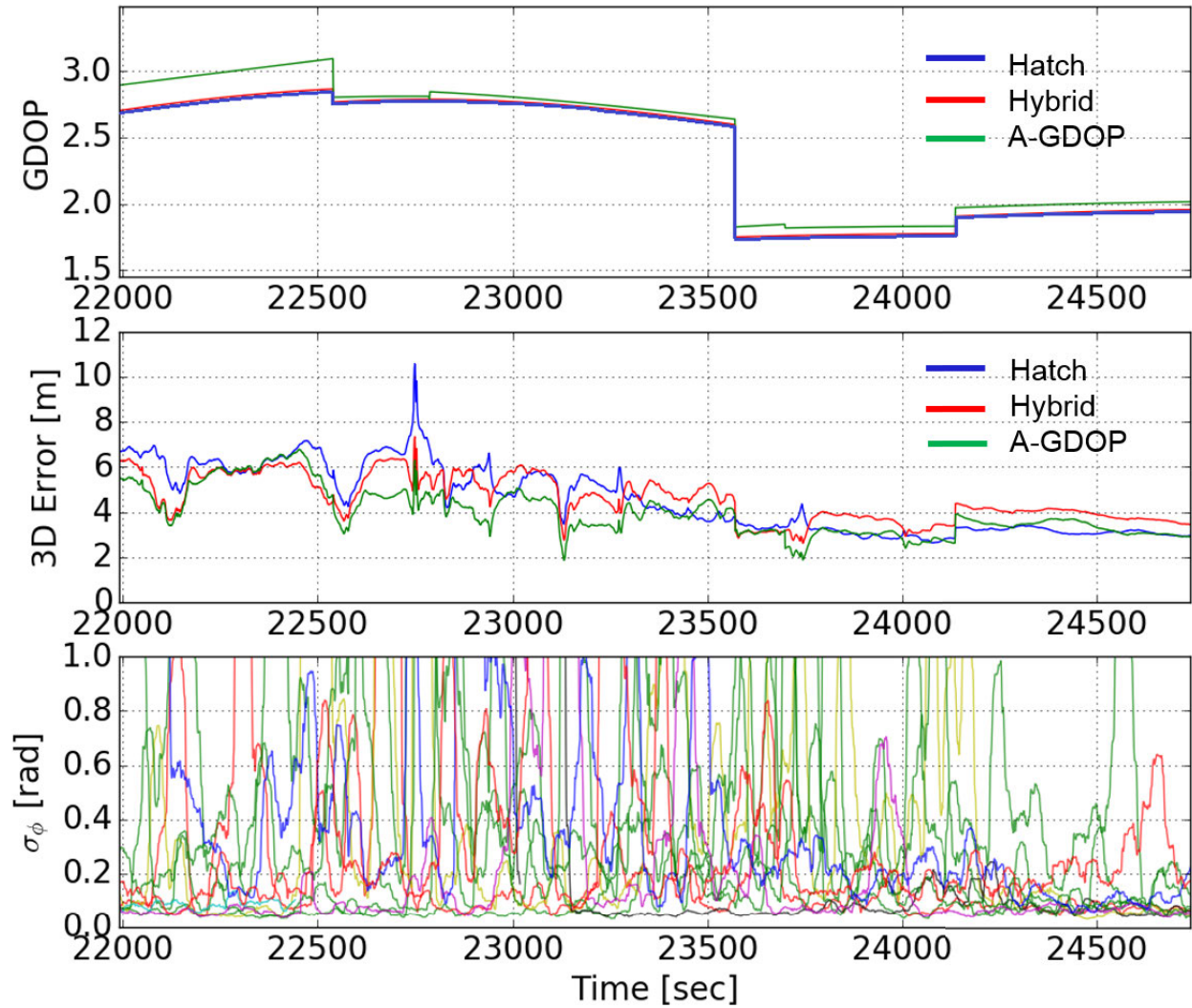


Figure 4.12: Poker Flat, Alaska positioning algorithms. 10/7/2015 22:02 - 22:49 LT. Subplot 1: GDOP for algorithm 3 (Hatch filter) in blue, algorithm 4 (hybrid technique) in red, and the *A-GDOP* algorithm in green. Subplot 2: 3D error of algorithm 3 (blue), algorithm 4 (red), and *A-GDOP* (green). Subplot 3: σ_ϕ [radians] for all visible satellites.

that position solutions could not even be produced during the entire time frame because too much data was discarded, leaving only three usable satellites. Similar to the other sections, we see maximum and mean improvement in algorithm 4 as compared to algorithm 3. Unlike the first section, the weighted *A*- σ_ϕ errors visibly have a larger maximum, mean, and standard deviation than the standard *A*- σ_ϕ . Since multiple satellites are given smaller weights in the processing, the position estimate relies more on the remaining satellites. If

only a few satellites are left without a weight applied to their measurements, accuracy will degrade as we see in the figure. In this scenario, the *A-GDOP* algorithm has even more options of satellites to remove from the processing without hurting the GDOP. As a result of removing stronger scintillating satellites, the mean error is reduced in all data sets, and the maximum error is reduced in the majority.

Numerical analysis of algorithm 4 in table 4.3 reveals a maximum error reduction up to 31%, and a mean error reduction up to 7% when comparing against algorithm 3. In one case, the standard deviation was increased by nearly 50%, but in another, it was reduced by up to 34%. With multiple satellites scintillating, *A-GDOP* also increases the standard deviation in half of the data sets by up to 57%. However, standard deviation, mean, and maximum error reductions were able to reach 36%, 13%, and 30%, respectively. In this scenario, the *A- σ_ϕ* algorithms more than double the standard deviation of the position solutions, and the weighted *A- σ_ϕ* algorithm does worse with more satellites scintillating. As mentioned previously, it would be possible to get even more improvement out of the *A-GDOP* algorithm through the incorporation of multi-GNSS. With three or more satellites scintillating, they could potentially all be removed from the navigation processing if there were additional satellites from other constellations that were not experiencing scintillation. General conclusions from the statistics of the algorithms in these three scenarios are summarized in the following chapter.

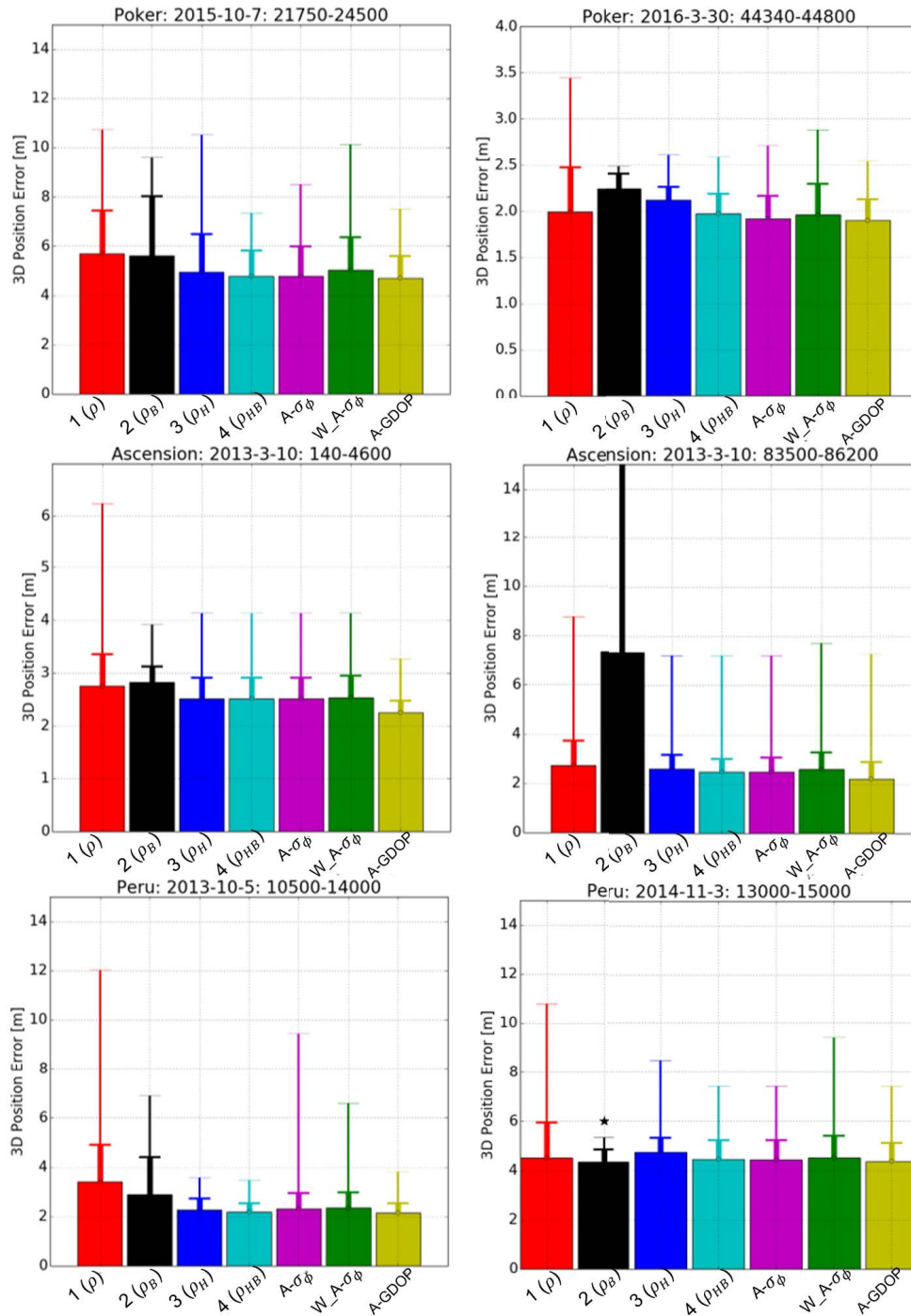


Figure 4.13: Scenario 3 positioning error statistics. Statistical comparison of 3D positioning errors on data sets with 3+ satellites scintillating. The large bar indicates the mean error, the thick error bar represents the standard deviation, and the thin error bar shows the maximum error. The black star in the bottom right subplot indicates that this algorithm was not able to produce a position estimate for the entire time range, so the result may be skewed.

Table 4.3: Adaptive positioning algorithm performance - scenario 3. Reduction in 3D error of algorithm 4 (ρ_{HB}), A -GDOP, and A - σ_ϕ algorithms with three or more satellites experiencing scintillation as compared to algorithm 3 (ρ_H)

Error Reduction of Algorithms \rightarrow	Algorithm 4	A -GDOP	A - σ_ϕ	Weighted A - σ_ϕ
Data Set \downarrow	Maximum Mean Std	Maximum Mean Std	Maximum Mean Std	Maximum Mean Std
Alaska: 10/7/2015 22:02 - 22:49 LT	31.44 % 3.77 % 34.25 %	30.02 % 3.99 % 36.36 %	21.32 % 3.53 % 21.6 %	2.94 % -1.96 % 14.86 %
Alaska: 3/30/2016 04:17 - 04:28 LT	0.96 % 7.17 % -49.99 %	2.64 % 10.51 % -57.14 %	-3.69 % 9.63 % -77.18 %	-10.25 % 7.36 % -135.29 %
Ascension Island: 3/10/2013 23:11 - 23:56 LT	0.00 % 4.65 % 5.40 %	-0.86 % 13.57 % -19.66 %	0.00 % 4.62 % -3.70 %	-5.71 % 0.09 % -22.21 %
Ascension Island: 3/10/2013 00:02 - 01:17 LT	0.00 % 0.00 % 0.00 %	22.42 % 10.39 % 28.20 %	0.00 % -0.03 % -1.24 %	0.00 % -1.07 % -3.09 %
Peru: 10/5/2013 21:55 - 22:54 LT	11.75 % 5.98 % -18.18 %	11.75 % 6.69 % -19.01 %	-163.37 % -2.04 % -40.10 %	-83.71 % -4.12 % -38.16 %
Peru: 11/3/2014 22:36 - 23:10 LT	3.41 % 3.81 % -22.08 %	-6.36 % 5.19 % -16.66 %	3.41 % 4.16 % -32.71 %	-10.75 % 3.01 % -50.01 %

CHAPTER 5

CONCLUSIONS AND FUTURE WORK

Ionospheric scintillation remains a significant problem for GNSS applications that operate in low or high latitudes. The presence of phase and amplitude scintillation often results in cycle slips, dropped measurements, and phase fluctuations in the carrier phase measurements. It is clear that these problematic measurements can cause position errors in standard positioning techniques. Three approaches to mitigate each of these problems were discussed: substituting the unsmoothed pseudorange, weighting satellites in the navigation processing, or completely excluding satellites from the navigation processing. Based on these approaches, the first adaptive algorithm that was developed substitutes the unsmoothed pseudorange for the carrier-smoothed pseudorange when phase scintillation is detected ($A\text{-}\sigma_\phi$). The second adaptive algorithm uses the GDOP to determine if a scintillating satellite can be removed from the processing ($A\text{-GDOP}$).

These algorithms were compared using real data from Poker Flat, Alaska, Ascension Island, and Jicamarca, Peru. For this in-depth analysis, performance comparisons were made against a positioning algorithm that uses a common technique for carrier-smoothing: the Hatch filter. Since it was shown that the $A\text{-}\sigma_\phi$ algorithm has an overall worse performance than the Hatch filter, we can conclude that using a satellite's unsmoothed pseudorange measurements increases position error. More specifically, even during large phase fluctuations, the error on the carrier-smoothed pseudorange is not enough to exceed the error on the unsmoothed pseudorange. As long as there are no carrier phase discontinuities (or they have been repaired), these results indicate that more precision and accuracy can be obtained by using carrier-smoothed pseudoranges instead of the unsmoothed pseudorange. Therefore, $A\text{-}\sigma_\phi$ should only be used in circumstances where cycle slip repair is a challenge (such as

on a highly dynamic platform). On average, the $A\text{-}\sigma_\phi$ algorithm increased the maximum error by 24.5%. The weighted version of this algorithm increased maximum errors by 8.3%. In general, weights on $A\text{-}\sigma_\phi$ should only be used when there is only one or two satellites scintillating. Weighting the solution when there are three or more satellites will likely cause errors by putting a heavy reliance on the remaining satellites.

Analyzing the GDOP is important for positioning algorithms such as $A\text{-GDOP}$. In many data sets, it was found that the manual removal of scintillating satellites from navigation processing can often improve positioning results as long as the impact to the GDOP is not substantial. $A\text{-GDOP}$ was found to reduce maximum errors on average by 13.0%, and up to 42.2%. Mean errors were reduced by up to 29.6%, and by 8.3% on average over all of the data sets.

The hybrid carrier-smoothing technique developed in this thesis generally improves positioning performance over the Hatch filter as long as there are not many dropped measurements. Otherwise, the two techniques have almost identical performance. The hybrid technique was able to reduce maximum positioning errors by up to 37.6%, and by 7.9% on average out of all of the scintillation data that was used. Mean positioning errors could be reduced by up to 50.4% and by 8.5% on average simply by applying this new carrier-smoothing technique.

Position errors using the algorithms in this thesis were dependent upon the number of satellites scintillating. For example, error reduction proved to be better when using the $A\text{-GDOP}$ algorithm as compared to the standard techniques when there were multiple satellites experiencing scintillation as opposed to just one. Current receivers or ground systems must consider GDOP when trying to optimize position solutions through the selection of high quality satellite measurements. Overall, the average improvements of these techniques ranges from 7-13%, which is not exactly a drastic change. Further improvements could be made with advancements in tracking during scintillation. Continuously tracking through low signal power or phase fluctuations without losing lock would be valuable to obtaining

higher quality range measurements, leading to improved integrity and performance of the navigation processing.

There is still more research to be done on this topic. First, these algorithms could be expanded to incorporate other satellite constellations. If there are more satellites to be used in the positioning solution, the GDOP would be improved, which would allow for a better performance out of the *A-GDOP* algorithm. This algorithm could also be improved by a more in-depth analysis of the GDOP. Based on the application, it could be altered to look at other geometric measures such as the vertical dilution of precision (VDOP), or horizontal dilution of precision (HDOP). For example, VDOP would be more crucial during a plane landing, but HDOP would be more important for movements on the ground.

Next, the majority of this analysis was based on the phase fluctuation indicator σ_ϕ . It is possible that different conclusions could be derived by simultaneously focusing on the amplitude fluctuation indicator S_4 . Algorithms could also be updated based on the general location of the receiver. For example, we saw that high latitudes have much more phase scintillation than amplitude scintillation. At these locations, we could base the adaptive algorithms on σ_ϕ . However, we saw that equatorial regions experience strong amplitude and phase scintillation, so it may be helpful for algorithms to adapt to both σ_ϕ and S_4 .

Improvements to the hybrid Hatch filter/CNMP carrier-smoothing method could also be explored. For now, the algorithm forces a bias estimate at the peak of the satellite pass, regardless of the value of its highest elevation. It was shown that poor bias estimates may be formed if the satellite does not reach a high enough elevation (typically less than 40 degrees). This could be solved by applying an elevation mask to the hybrid carrier-smoothing process. For example, if the peak elevation of a satellite pass does not reach a certain threshold, then we will continue to use the Hatch filter technique to carrier-smoothing rather than force a bias estimate using the CNMP method.

Also, improvements could be made regarding dropped measurements. If there is a dropped measurement on the L1 frequency, it is likely that there will be a measurement

on the L2 or L5 frequencies. This information could possibly be used to repair the dropped measurement on the L1 frequency. All of these ideas for future work would need to be explored over massive amounts of scintillation data to get a more confident assessment of the general applicability.

REFERENCES

- [1] National coordination office for space-based positioning, navigation, and timing. (2014) GPS applications. [Online]. Available: <http://www.gps.gov/applications/>
- [2] J. W. Betz, *Engineering satellite-based navigation and timing*. Hoboken, NJ: John Wiley and Sons, Inc., 2016.
- [3] D. Crane, *Dictionary of aeronautical terms*. Aviation Supplies and Academics,, 2012.
- [4] P. Misra and P. Enge, *Global positioning system: signals, measurements and performance second edition*. Lincoln, MA: Ganga-Jamuna Press, 2006.
- [5] H. Bourne, “An algorithm for accurate ionospheric total electron content and receiver bias estimation using GPS measurements,” Master’s thesis, Colorado State University, May 2016.
- [6] C. Kopp, “GPS aided guided munitions,” 2008, accessed 2017-03-03. [Online]. Available: <http://www.ausairpower.net/TE-GPS-Guided-Weps.html>
- [7] J. Klobuchar, “Ionospheric effects on GPS,” *Global Positioning System: Theory and applications.*, vol. 1, pp. 485–515, 1996.
- [8] J. J. Spilker, “Tropospheric effects on GPS,” *Global Positioning System: Theory and applications.*, vol. 1, pp. 517–546, 1996.
- [9] J. Kouba, “A guide to using international GNSS service (IGS) products,” Natural Resources Canada.
- [10] G. ICD. (2013) Global positioning systems directorate system engineering & integration interface specification IS-GPS-200G.

- [11] Navipedia, “Precise point positioning - navipedia,” 2014, [Online; accessed 5-June-2017]. [Online]. Available: http://www.navipedia.net/index.php?title=Precise_Point_Positioning&oldid=13291
- [12] S. Basu, K. Groves, S. Basu, and P. Sultan, “Specification and forecasting of scintillations in communication/navigation links: current status and future plans,” *Journal of Atmospheric and Solar-Terrestrial Physics*, vol. 64, no. 16, pp. 1745–1754, 2002.
- [13] Y. Jiao and Y. T. Morton, “Comparison of the effect of high-latitude and equatorial ionospheric scintillation on GPS signals during the maximum of solar cycle 24,” *Radio Science*, vol. 50, no. 9, pp. 886–903, 2015.
- [14] K. C. Yeh and C.-H. Liu, “Radio wave scintillations in the ionosphere,” *Proceedings of the IEEE*, vol. 70, no. 4, pp. 324–360, 1982.
- [15] F. Niu, “Performances of GPS signal observables detrending methods for ionosphere scintillation studies,” Master’s thesis, Miami University, 2012.
- [16] B. Briggs and I. Parkin, “On the variation of radio star and satellite scintillations with zenith angle,” *Journal of Atmospheric and Terrestrial Physics*, vol. 25, no. 6, pp. 339–366, 1963.
- [17] F. Niu, Y. Morton, J. Wang, and W. Pelgrum, “GPS carrier phase detrending methods and performances for ionosphere scintillation studies,” in *25th International Technical Meeting of the Satellite Division of The Institute of Navigation, ION GNSS*, vol. 2000, 2012, pp. 1462–1467.
- [18] S. B. Bisnath and R. B. Langley, “Efficient, automated cycle-slip correction of dual-frequency kinematic GPS data,” in *proceedings of ION GPS*, 2000, pp. 145–154.
- [19] M. Aquino, J. Monico, A. Dodson, H. Marques, G. De Franceschi, L. Alfonsi, V. Romano, and M. Andreotti, “Improving the GNSS positioning stochastic model in the

- presence of ionospheric scintillation,” *Journal of Geodesy*, vol. 83, no. 10, pp. 953–966, 2009.
- [20] R. S. Conker, M. B. El-Arini, C. J. Hegarty, and T. Hsiao, “Modeling the effects of ionospheric scintillation on GPS/satellite-based augmentation system availability,” *Radio Science*, vol. 38, no. 1, 2003.
- [21] M. Karaim, “Real-time cycle-slip detection and correction for land vehicle navigation using inertial aiding,” 2013.
- [22] D. Xu, “Beidou and GPS dual constellation vector tracking during ionosphere scintillation at equatorial region,” Master’s thesis, Miami University, 2014.
- [23] L. Zhang and Y. Morton, “Tracking GPS signals under ionosphere scintillation conditions,” in *Proceedings of the 22nd International Technical Meeting of the Satellite Division of The Institute of Navigation (ION GNSS 2009)*, 2009, pp. 227–234.
- [24] S. Datta-Barua, P. Doherty, S. Delay, T. Dehel, and J. A. Klobuchar, “Ionospheric scintillation effects on single and dual frequency GPS positioning,” in *Proceedings of the 16th International Technical Meeting of the Satellite Division of The Institute of Navigation (ION GPS/GNSS 2003)*, 2003, pp. 336–346.
- [25] Z. Liu, “A new automated cycle slip detection and repair method for a single dual-frequency GPS receiver,” *Journal of Geodesy*, vol. 85, no. 3, pp. 171–183, 2011.
- [26] S. Taylor, Y. Morton, Y. Jiao, J. Triplett, and W. Pelgrum, “An improved ionosphere scintillation event detection and automatic trigger for GNSS data collection systems,” 2012, pp. 1563–1569.
- [27] K. Yeh, C. Liu, and M. Youakim, “A theoretical study of the ionospheric scintillation behavior caused by multiple scattering,” *Radio Science*, vol. 10, no. 1, pp. 97–106, 1975.

- [28] J. Aarons, “Global morphology of ionospheric scintillations,” *Proceedings of the IEEE*, vol. 70, no. 4, pp. 360–378, 1982.
- [29] R. Thomas, M. Cervera, A. G. Ramli, P. Totarong, K. Groves, and P. Wilkinson, “Seasonal modulation of GPS performance due to equatorial scintillation,” *Geophysical Research Letters*, vol. 31, no. 18, 2004.
- [30] Y. Jiao, J. Hall, and Y. Morton, “GPS carrier phase detrending methods and performances for ionosphere scintillation studies,” in *Proceedings of the 2017 International Technical Meeting of The Institute of Navigation*, 2017, pp. 1160 – 1172.
- [31] J. Aarons, H. E. Whitney, E. MacKenzie, and S. Basu, “Microwave equatorial scintillation intensity during solar maximum,” *Radio Science*, vol. 16, no. 05, pp. 939–945, 1981.
- [32] P. Prikryl, P. Jayachandran, S. Mushini, D. Pokhotelov, J. MacDougall, E. Donovan, E. Spanswick, and J.-P. St-Maurice, “GPS TEC, scintillation and cycle slips observed at high latitudes during solar minimum,” in *Annales Geophysicae*, vol. 28, no. 6. Copernicus GmbH, 2010, pp. 1307–1316.
- [33] Z. Dai, “MATLAB software for GPS cycle-slip processing,” *GPS solutions*, vol. 16, no. 2, pp. 267–272, 2012.
- [34] R. Hatch, “Instantaneous ambiguity resolution,” in *Kinematic Systems in Geodesy, Surveying, and Remote Sensing*. Springer, 1991, pp. 299–308.
- [35] D. C. Bruckner, F. van Grass, and T. A. Skidmore, “Algorithm and flight test results to exchange code noise and multipath for biases in dual frequency differential GPS for precision approach,” *Navigation*, vol. 57, no. 3, pp. 213–228, 2010.

- [36] H. Bourne, Y. Morton, F. van Graas, M. Sulzer, and M. Milla, “Spacial gradient based TEC estimation algorithm with code noise multipath correction evaluation using simultaneous incoherent scatter radar measurements,” in *Proceedings of the 2016 International Technical Meeting of The Institute of Navigation*, 2017, pp. 140 – 150.
- [37] G. Myer, Y. Morton, and B. Schipper, “Ionospheric scintillation effects on GPS pseudorange and carrier phase measurements and an adaptive algorithm to limit position errors during scintillation,” in *Proceedings of the 2017 International Technical Meeting of The Institute of Navigation*, 2017, pp. 971 – 988.
- [38] Y. Yong and M. Lingjuan, “GDOP results in all-in-view positioning and in four optimum satellites positioning with GPS PRN codes ranging,” in *Position Location and Navigation Symposium, 2004. PLANS 2004*. IEEE, 2004, pp. 723–727.
- [39] P. F. Swaszek, R. J. Hartnett, K. C. Seals, and R. M. A. Swaszek, “A temporal algorithm for satellite subset selection in multi-constellation GNSS,” in *Proceedings of the 2017 International Technical Meeting of The Institute of Navigation*, 2017, pp. 1147–1159.

APPENDIX A

ADDITIONAL PLOTS

These additional plots show skyplots and position errors for all of the data sets used in Chapter 4 of this thesis. The color coding for the position error plots is the same as the histograms shown previously, and it is re-iterated below for convenience:

- ρ_c - red
- ρ_B - black
- ρ_H - blue
- ρ_{HB} - cyan
- $A\text{-}\sigma_\phi$ - magenta
- $W\text{-}A\text{-}\sigma_\phi$ - green
- $A\text{-}GDOP$ - yellow

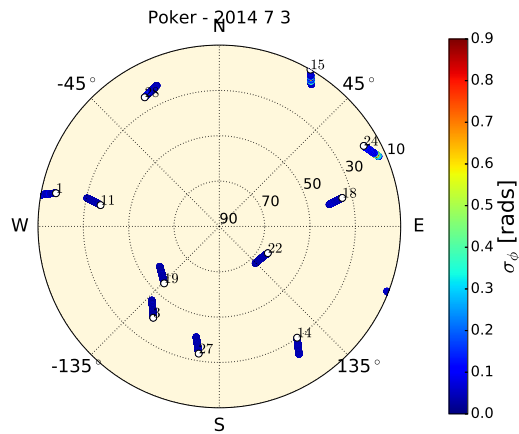


Figure A.1: Poker Flat, Alaska 7/3/2014 skyplot. Satellite tracks are colored by the σ_ϕ value in radians.

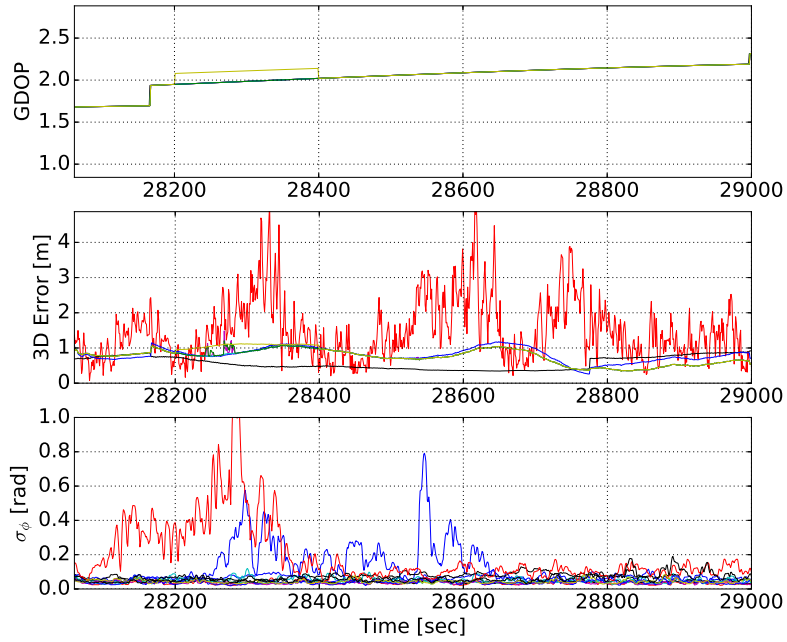


Figure A.2: Poker Flat, Alaska 7/3/2014 positioning algorithms. Subplot 1: GDOP for all positioning algorithms. ρ_B - black, APGA - yellow, remaining algorithms - green. Subplot 2: Overlay of positioning algorithms colored the same as table 3.2. Subplot 3: σ_ϕ [radians] for all visible satellites.

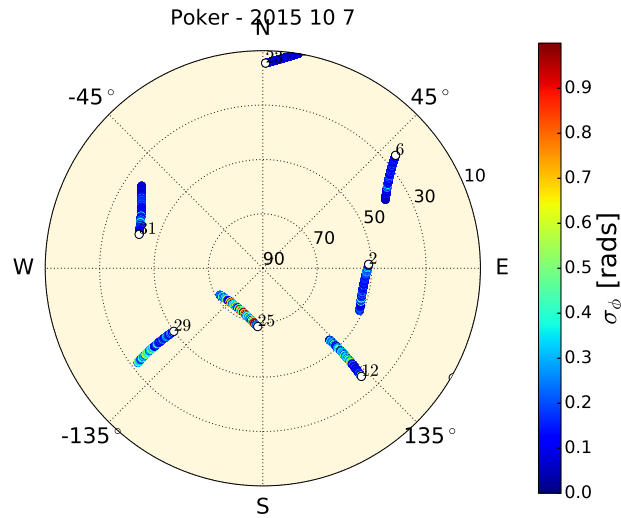


Figure A.3: Poker Flat, Alaska 10/7/2015 skyplot. Satellite tracks are colored by the σ_ϕ value in radians.

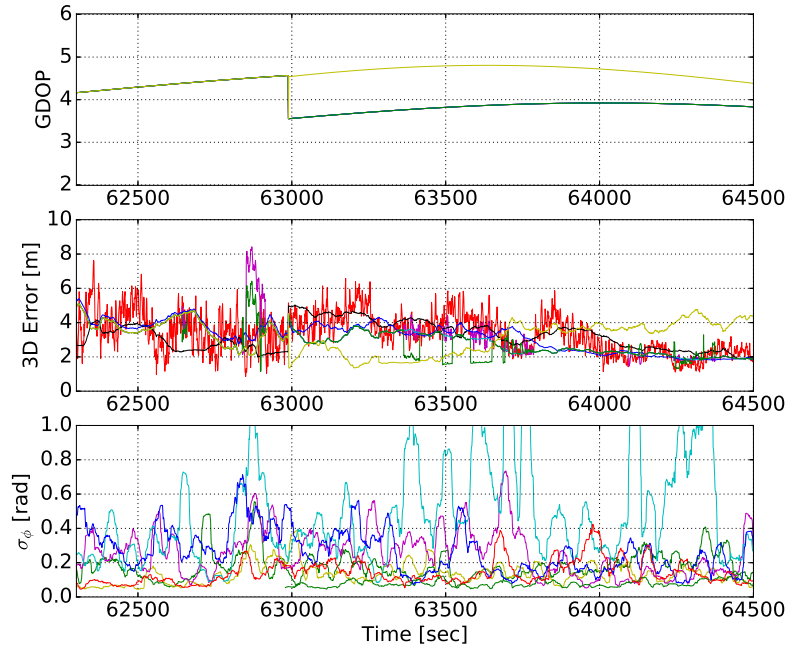


Figure A.4: Poker Flat, Alaska 10/7/2015 positioning algorithms. Subplot 1: GDOP for all positioning algorithms. ρ_B - black, APGA - yellow, remaining algorithms - green. Subplot 2: Overlay of positioning algorithms colored the same as table 3.2. Subplot 3: σ_ϕ [radians] for all visible satellites.

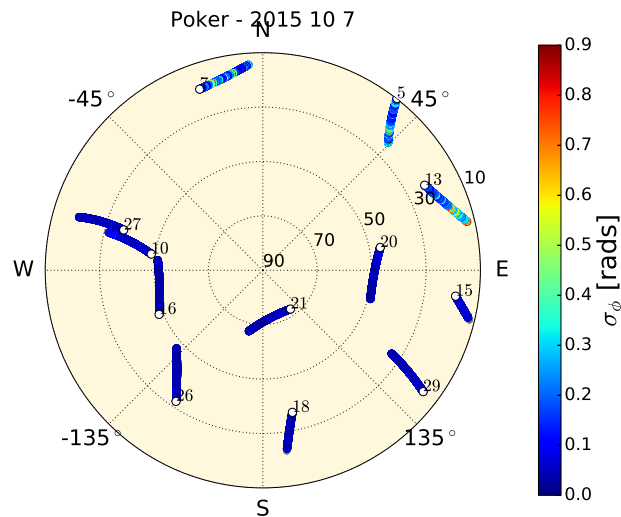


Figure A.5: Poker Flat, Alaska 10/7/2015 skyplot. Satellite tracks are colored by the σ_ϕ value in radians.

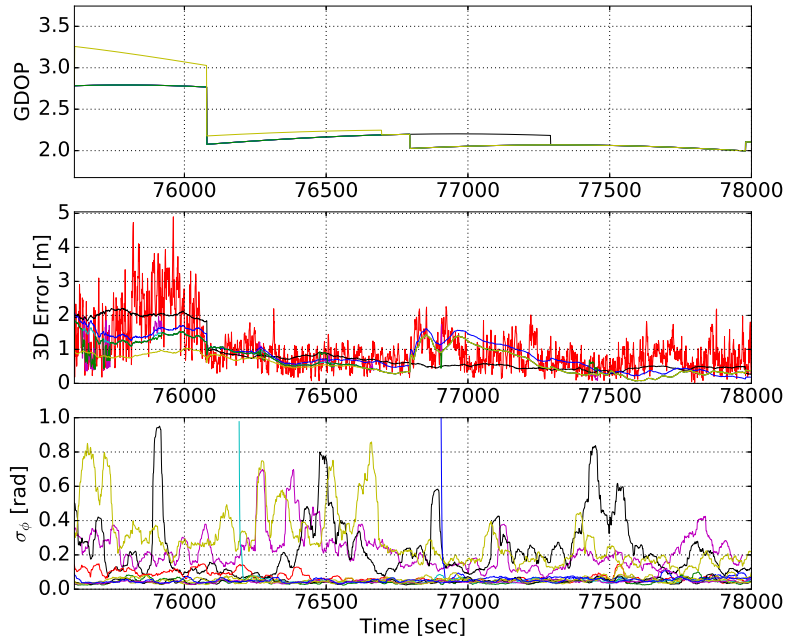


Figure A.6: Poker Flat, Alaska 10/7/2015 positioning algorithms. Subplot 1: GDOP for all positioning algorithms. ρ_B - black, APGA - yellow, remaining algorithms - green. Subplot 2: Overlay of positioning algorithms colored the same as table 3.2. Subplot 3: σ_ϕ [radians] for all visible satellites.

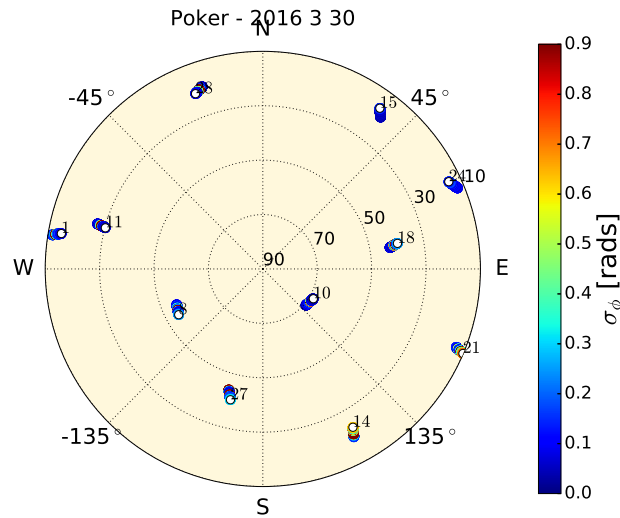


Figure A.7: Poker Flat, Alaska 3/30/2016 skyplot. Satellite tracks are colored by the σ_ϕ value in radians.

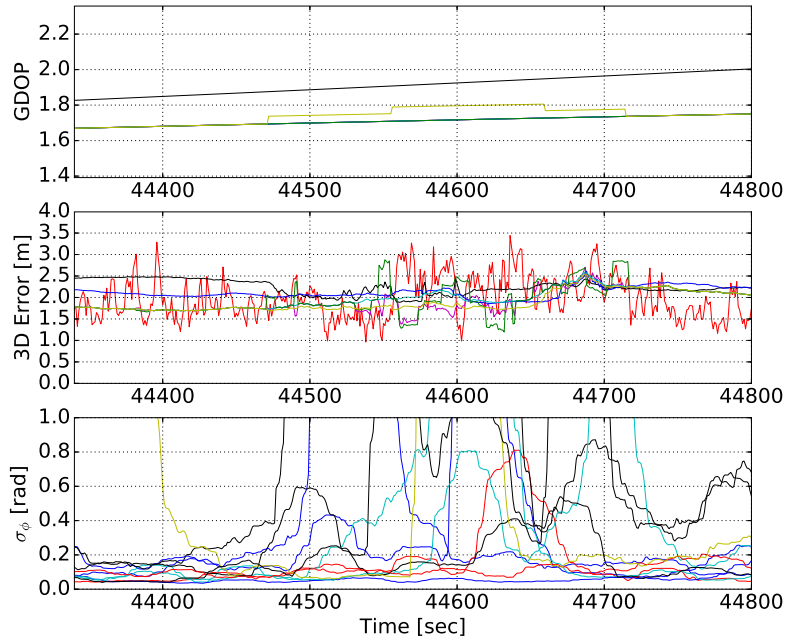


Figure A.8: Poker Flat, Alaska 3/30/2016 positioning algorithms. Subplot 1: GDOP for all positioning algorithms. ρ_B - black, APGA - yellow, remaining algorithms - green. Subplot 2: Overlay of positioning algorithms colored the same as table 3.2. Subplot 3: σ_ϕ [radians] for all visible satellites.

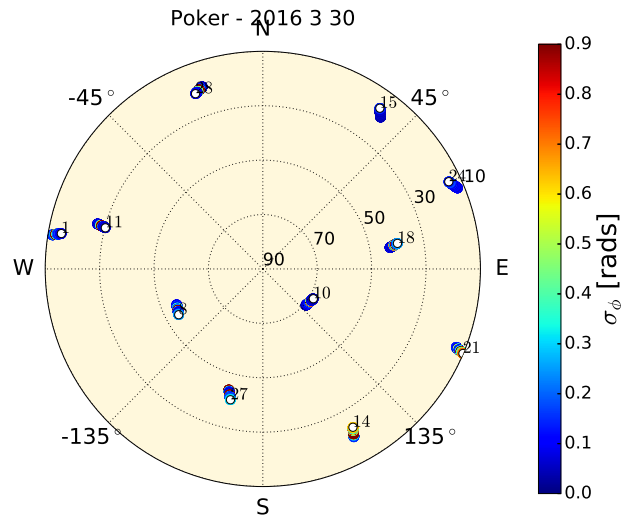


Figure A.9: Poker Flat, Alaska 3/30/2016 skyplot. Satellite tracks are colored by the σ_ϕ value in radians.

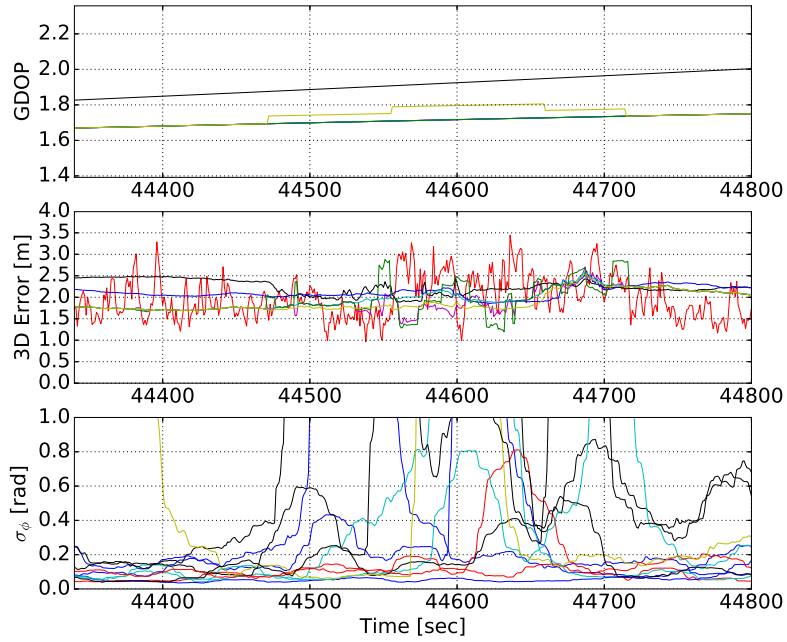


Figure A.10: Poker Flat, Alaska 3/30/2016 positioning algorithms. Subplot 1: GDOP for all positioning algorithms. ρ_B - black, APGA - yellow, remaining algorithms - green. Subplot 2: Overlay of positioning algorithms colored the same as table 3.2. Subplot 3: σ_ϕ [radians] for all visible satellites.

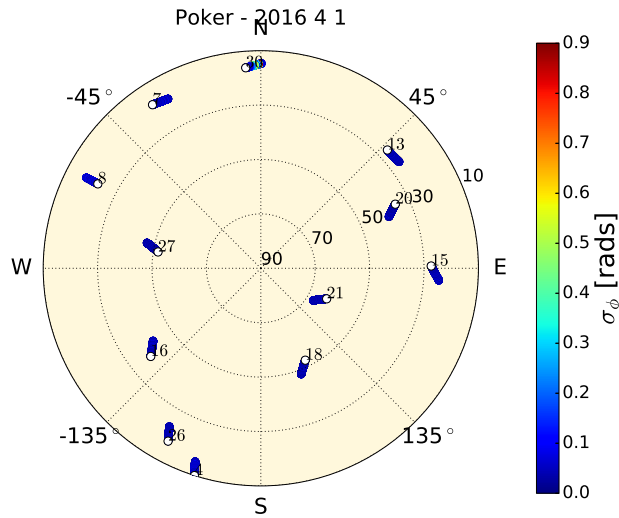


Figure A.11: Poker Flat, Alaska 4/1/2016 skyplot. Satellite tracks are colored by the σ_ϕ value in radians.

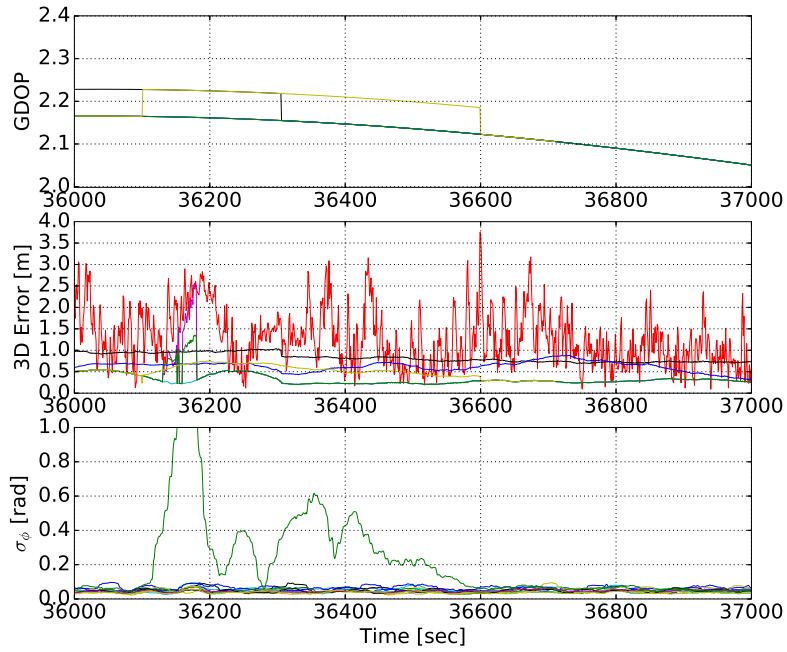


Figure A.12: Poker Flat, Alaska 4/1/2016 positioning algorithms. Subplot 1: GDOP for all positioning algorithms. ρ_B - black, APGA - yellow, remaining algorithms - green. Subplot 2: Overlay of positioning algorithms colored the same as table 3.2. Subplot 3: σ_ϕ [radians] for all visible satellites.

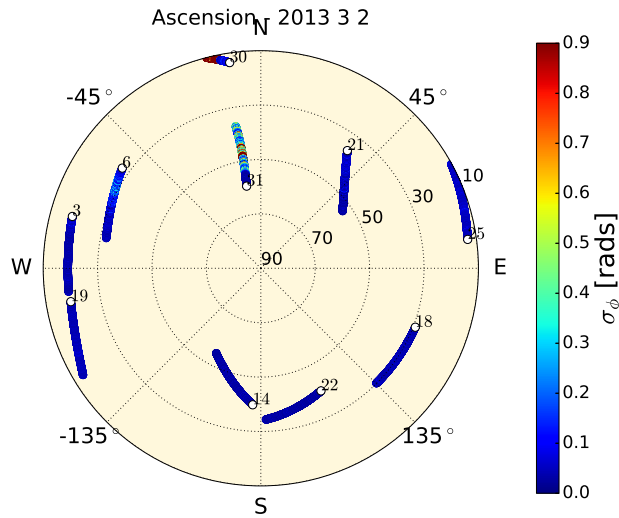


Figure A.13: Ascension Island 3/2/2013 skyplot. Satellite tracks are colored by the σ_ϕ value in radians.

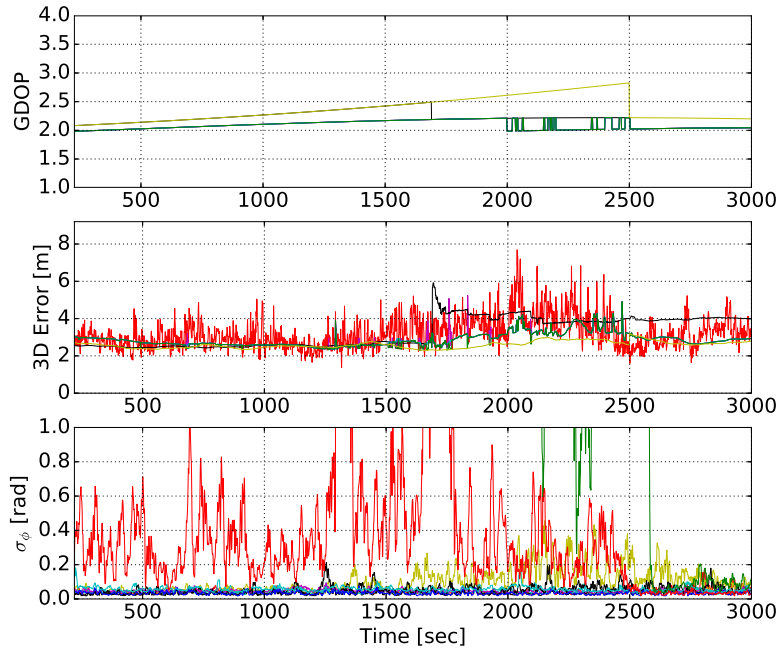


Figure A.14: Ascension Island 3/2/2013 positioning algorithms. Subplot 1: GDOP for all positioning algorithms. ρ_B - black, APGA - yellow, remaining algorithms - green. Subplot 2: Overlay of positioning algorithms colored the same as table 3.2. Subplot 3: σ_ϕ [radians] for all visible satellites.

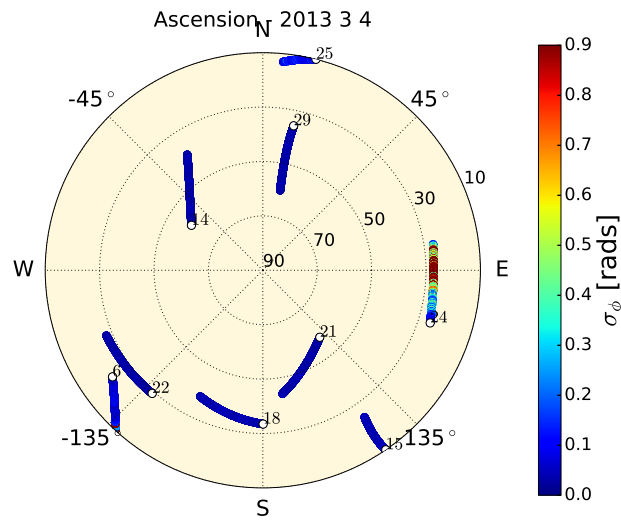


Figure A.15: Ascension Island 3/4/2013 skyplot. Satellite tracks are colored by the σ_ϕ value in radians.

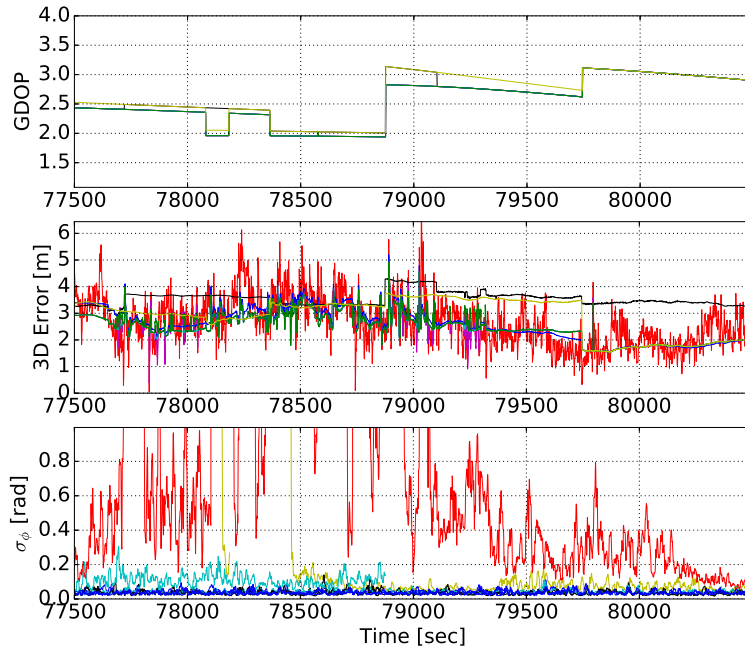


Figure A.16: Ascension Island 3/4/2013 positioning algorithms. Subplot 1: GDOP for all positioning algorithms. ρ_B - black, APGA - yellow, remaining algorithms - green. Subplot 2: Overlay of positioning algorithms colored the same as table 3.2. Subplot 3: σ_ϕ [radians] for all visible satellites.

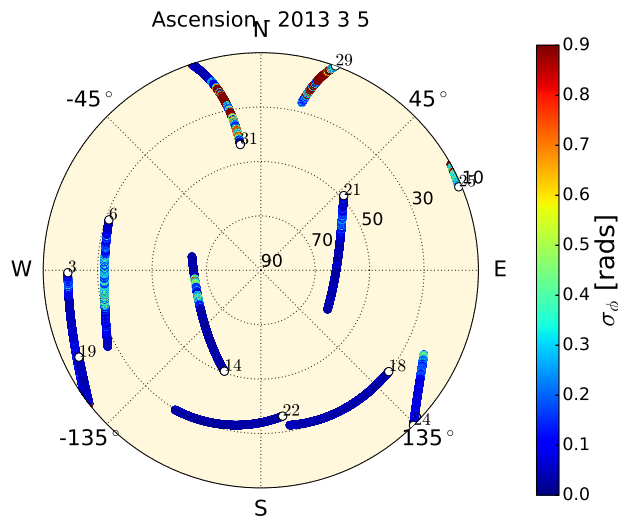


Figure A.17: Ascension Island 3/5/2013 skyplot. Satellite tracks are colored by the σ_ϕ value in radians.

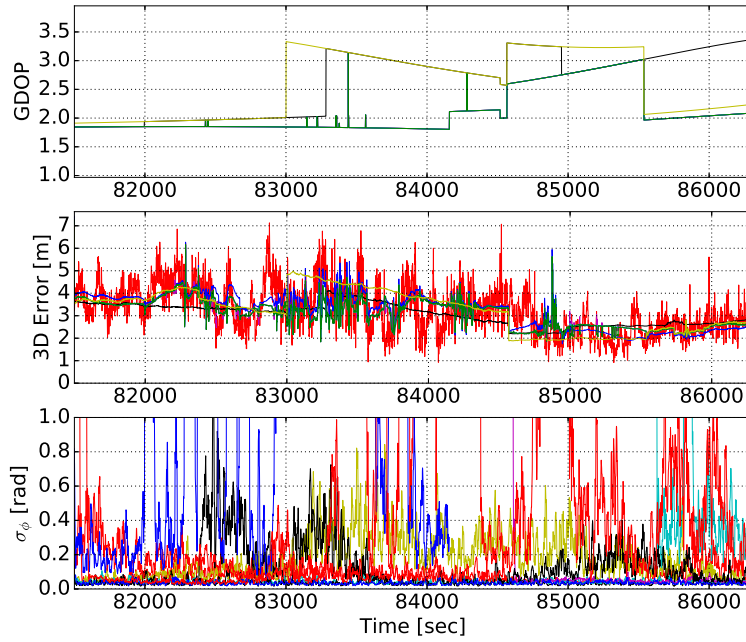


Figure A.18: Ascension Island 3/5/2013 positioning algorithms. Subplot 1: GDOP for all positioning algorithms. ρ_B - black, APGA - yellow, remaining algorithms - green. Subplot 2: Overlay of positioning algorithms colored the same as table 3.2. Subplot 3: σ_ϕ [radians] for all visible satellites.

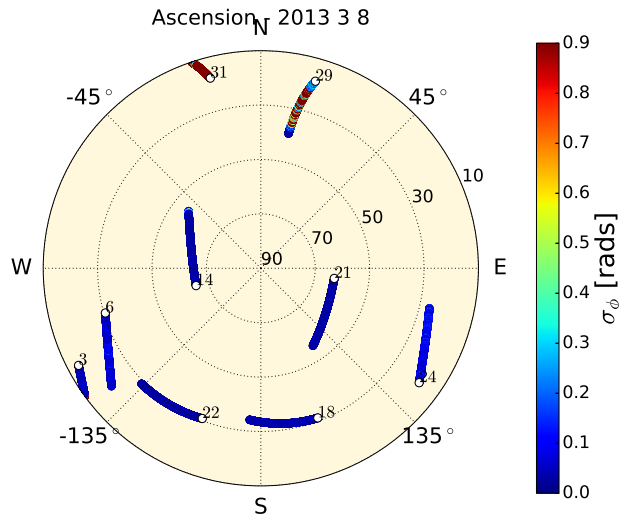


Figure A.19: Ascension Island 3/8/2013 skyplot. Satellite tracks are colored by the σ_ϕ value in radians.

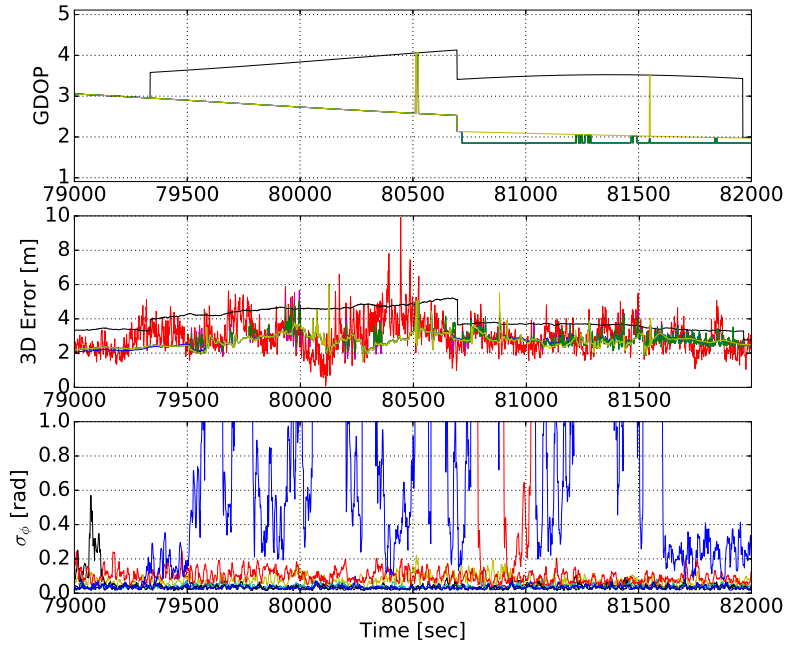


Figure A.20: Ascension Island 3/8/2013 positioning algorithms. Subplot 1: GDOP for all positioning algorithms. ρ_B - black, APGA - yellow, remaining algorithms - green. Subplot 2: Overlay of positioning algorithms colored the same as table 3.2. Subplot 3: σ_ϕ [radians] for all visible satellites.

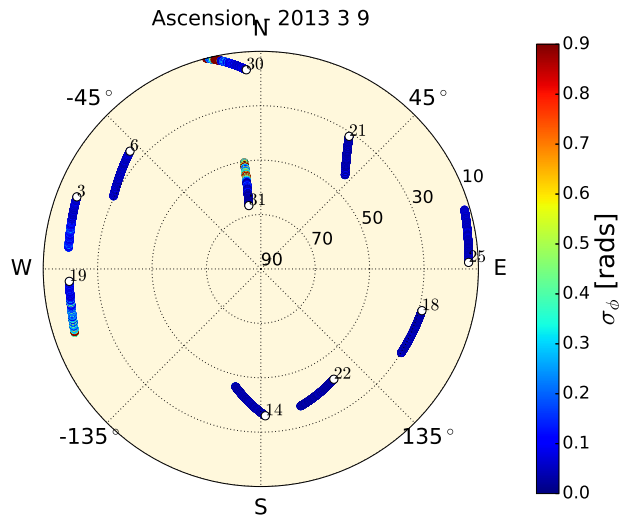


Figure A.21: Ascension Island 3/9/2013 skyplot. Satellite tracks are colored by the σ_ϕ value in radians.

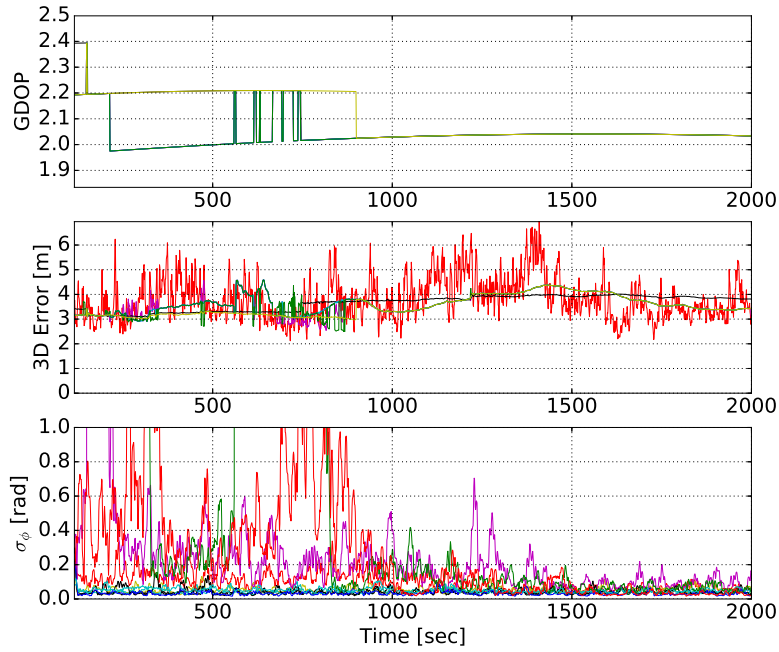


Figure A.22: Ascension Island 3/9/2013 positioning algorithms. Subplot 1: GDOP for all positioning algorithms. ρ_B - black, APGA - yellow, remaining algorithms - green. Subplot 2: Overlay of positioning algorithms colored the same as table 3.2. Subplot 3: σ_ϕ [radians] for all visible satellites.

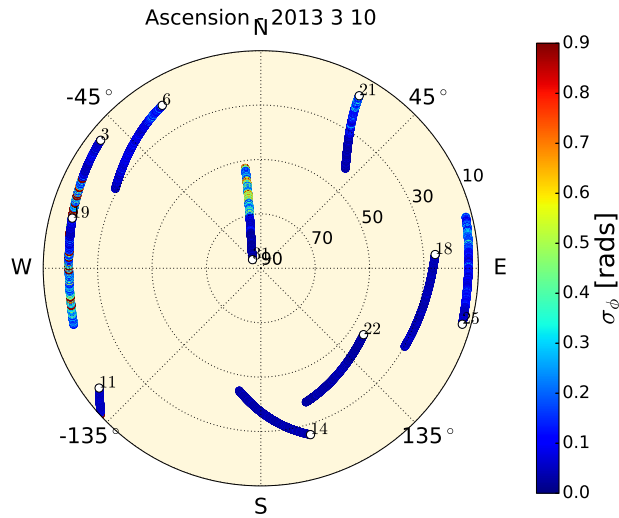


Figure A.23: Ascension Island 3/10/2013 skyplot. Satellite tracks are colored by the σ_ϕ value in radians.

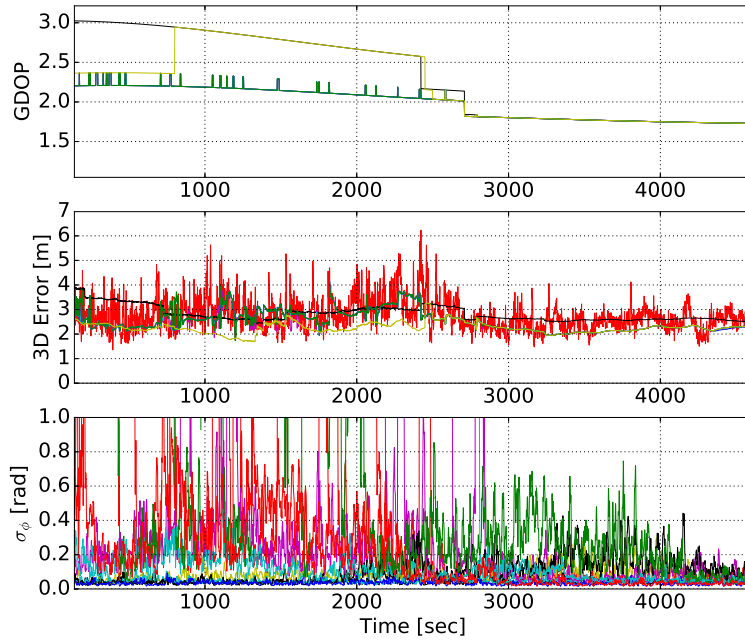


Figure A.24: Ascension Island 3/10/2013 positioning algorithms. Subplot 1: GDOP for all positioning algorithms. ρ_B - black, APGA - yellow, remaining algorithms - green. Subplot 2: Overlay of positioning algorithms colored the same as table 3.2. Subplot 3: σ_ϕ [radians] for all visible satellites.

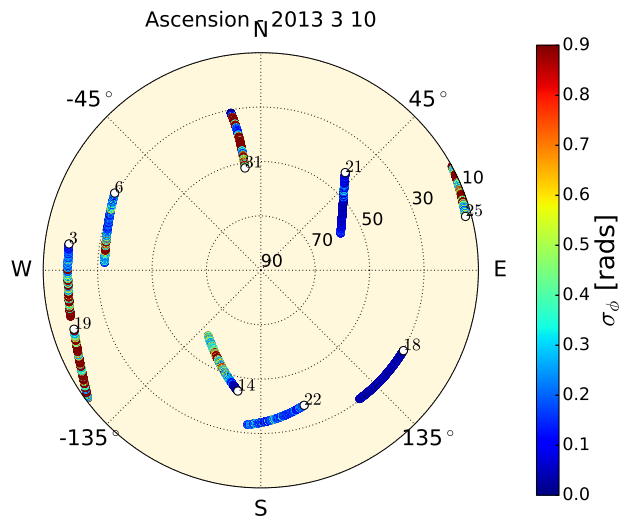


Figure A.25: Ascension Island 3/10/2013 skyplot. Satellite tracks are colored by the σ_ϕ value in radians.

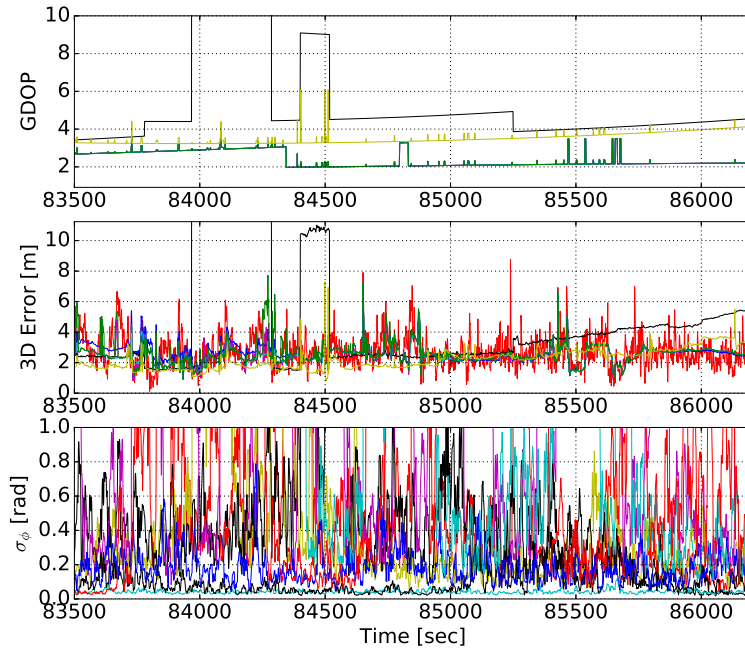


Figure A.26: Ascension Island 3/10/2013 positioning algorithms. Subplot 1: GDOP for all positioning algorithms. ρ_B - black, APGA - yellow, remaining algorithms - green. Subplot 2: Overlay of positioning algorithms colored the same as table 3.2. Subplot 3: σ_ϕ [radians] for all visible satellites.

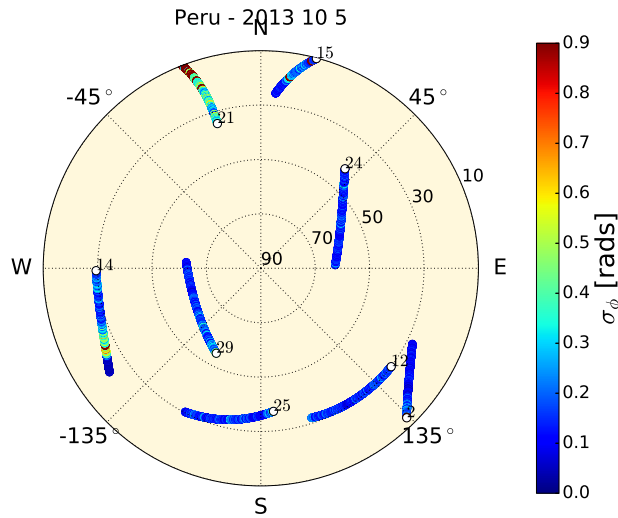


Figure A.27: Jicamarca, Peru 10/5/2013 skyplot. Satellite tracks are colored by the σ_ϕ value in radians.

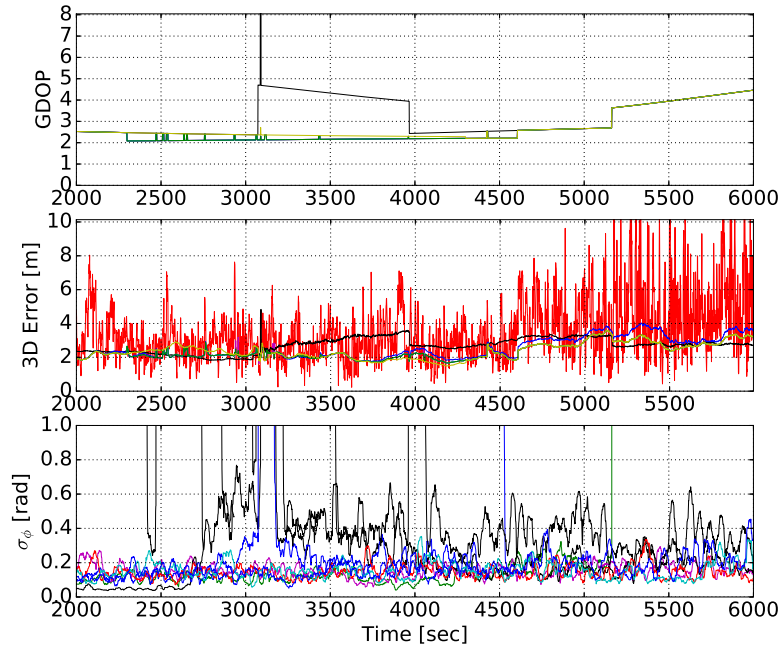


Figure A.28: Jicamarca, Peru 10/5/2013 positioning algorithms. Subplot 1: GDOP for all positioning algorithms. ρ_B - black, APGA - yellow, remaining algorithms - green. Subplot 2: Overlay of positioning algorithms colored the same as table 3.2. Subplot 3: σ_ϕ [radians] for all visible satellites.

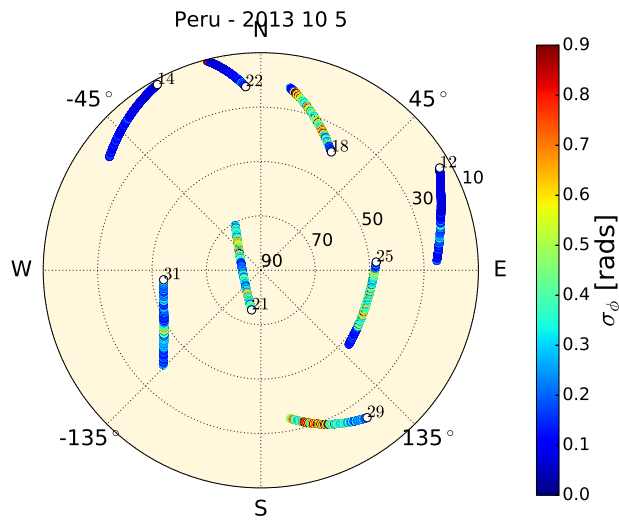


Figure A.29: Jicamarca, Peru 10/5/2013 skyplot. Satellite tracks are colored by the σ_ϕ value in radians.

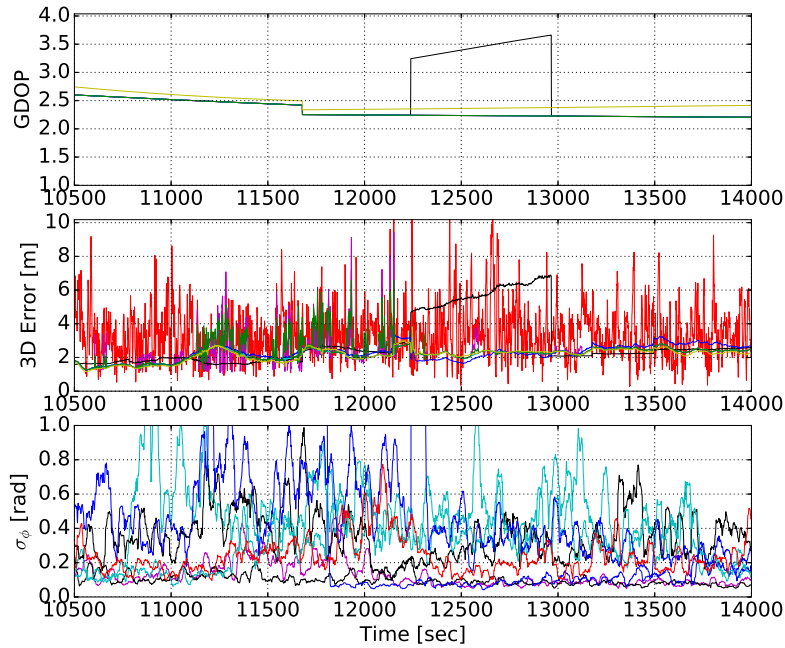


Figure A.30: Jicamarca, Peru 10/5/2013 positioning algorithms. Subplot 1: GDOP for all positioning algorithms. ρ_B - black, APGA - yellow, remaining algorithms - green. Subplot 2: Overlay of positioning algorithms colored the same as table 3.2. Subplot 3: σ_ϕ [radians] for all visible satellites.

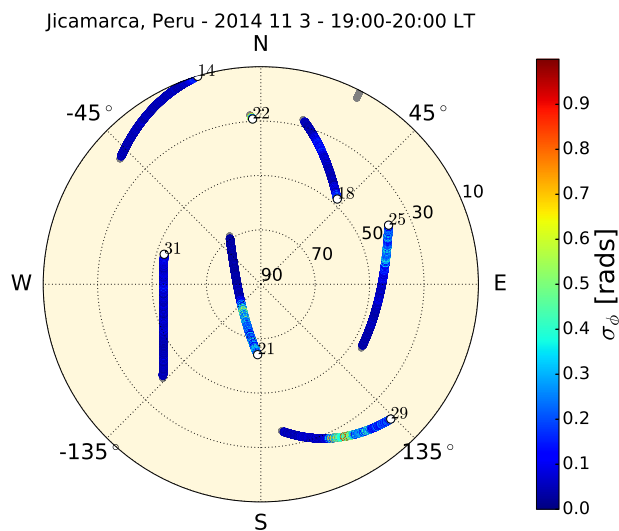


Figure A.31: Jicamarca, Peru 11/3/2014 skyplot. Satellite tracks are colored by the σ_ϕ value in radians.

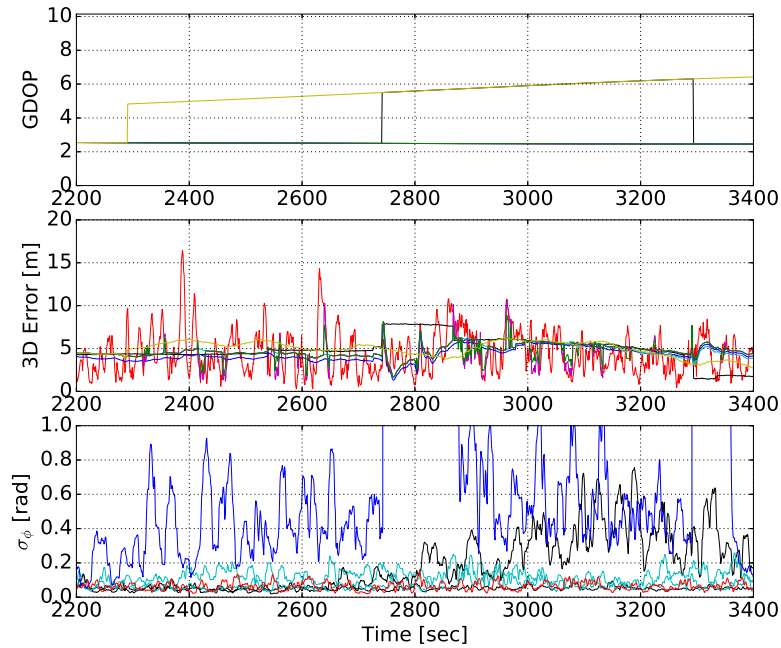


Figure A.32: Jicamarca, Peru 11/3/2014 positioning algorithms. Subplot 1: GDOP for all positioning algorithms. ρ_B - black, APGA - yellow, remaining algorithms - green. Subplot 2: Overlay of positioning algorithms colored the same as table 3.2. Subplot 3: σ_ϕ [radians] for all visible satellites.

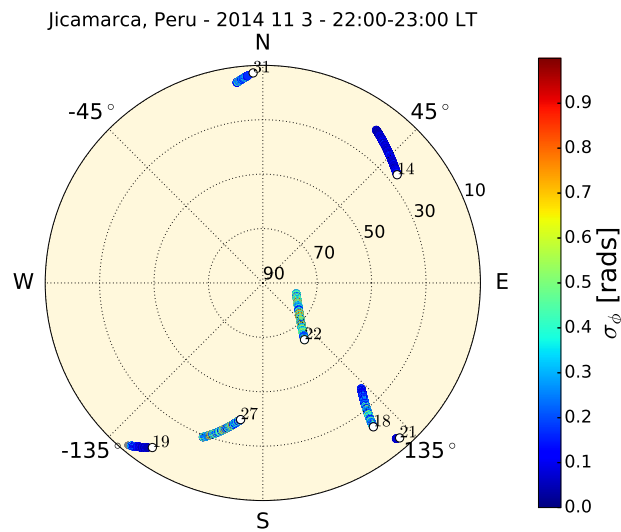


Figure A.33: Jicamarca, Peru 11/3/2014 skyplot. Satellite tracks are colored by the σ_ϕ value in radians.

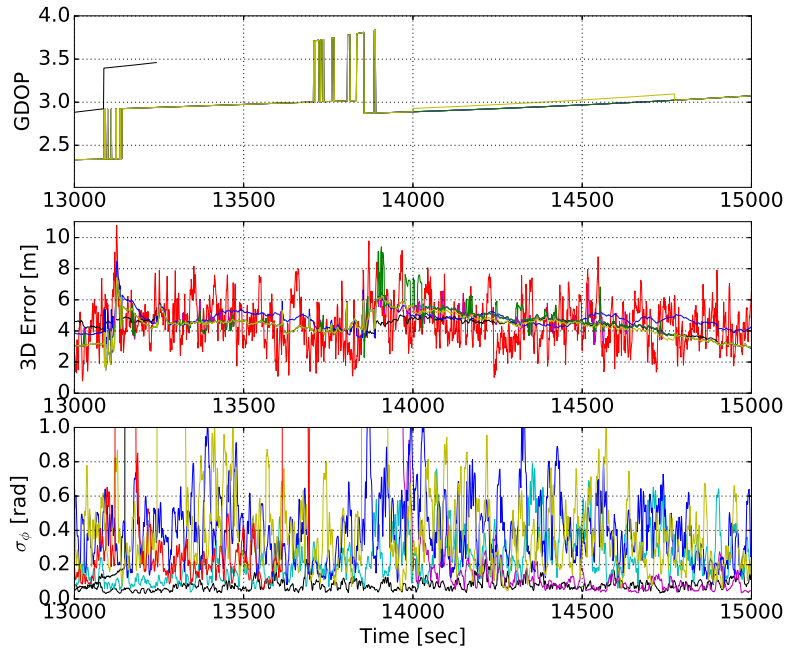


Figure A.34: Jicamarca, Peru 11/3/2014 positioning algorithms. Subplot 1: GDOP for all positioning algorithms. ρ_B - black, APGA - yellow, remaining algorithms - green. Subplot 2: Overlay of positioning algorithms colored the same as table 3.2. Subplot 3: σ_ϕ [radians] for all visible satellites.

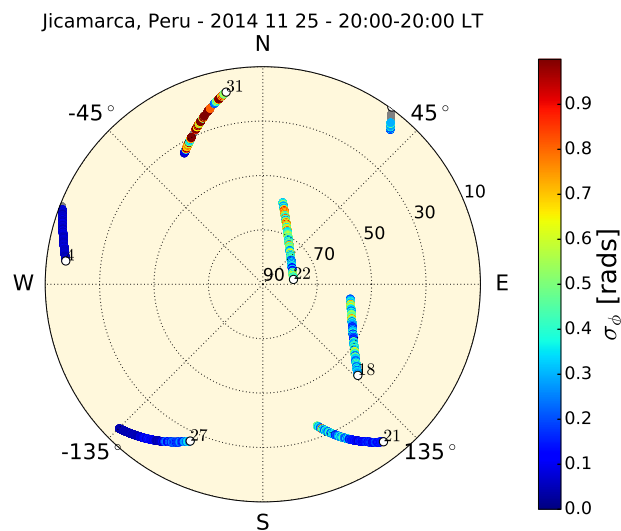


Figure A.35: Jicamarca, Peru 11/25/2014 skyplot. Satellite tracks are colored by the σ_ϕ value in radians.